INTERACTION OF SMALL MOLECULES WITH NUCLEIC ACID TARGETS: FROM RNA SECONDARY STRUCTURE TO THE RIBOSOME

A Dissertation
Presented to
The Academic Faculty

by

Joshua Craig Canzoneri

In Partial Fulfillment
of the Requirements for the Degree
Doctor of Philosophy in the
School of Chemistry and Biochemistry

Georgia Institute of Technology
December 2012

INTERACTION OF SMALL MOLECULES WITH THEIR NUCLEIC ACID TARGETS: FROM RNA SECONDARY STRUCTURE TO THE RIBOSOME

Approved by:

Dr. Adegboyega Oyelere, Advisor
School of Chemistry and Biochemistry
Georgia Institute of Technology

Dr. Stephen Harvey
School of Biology
Georgia Institute of Technology

Dr. Nicholas Hud
School of Chemistry and Biochemistry
Georgia Institute of Technology

Dr. Roger Wartell
School of Biology
Georgia Institute of Technology

Dr. Loren Williams
School of Chemistry and Biochemistry
Georgia Institute of Technology

Date Approved: July 23, 2012

ACKNOWLEDGEMENTS

The list of people that I owe thanks to for my current position in life is quite long, but I will highlight the most influential here. First and foremost, I would like to thank my advisor, Dr. Yomi Oyelere for the amazing opportunity to work in his lab. His steadfast sense of direction, understanding nature, and vast knowledge of all things chemistry have been a huge inspiration to me, and have undoubtedly helped me to mature as both a scientist and as a person. It is also his great passion for what he does that inspires me. The excitement seen in Dr. Oyelere's expression when presented with new data has provided me with a ceaseless sense of accomplishment throughout my graduate career. Most importantly, it has been Dr. Oyelere's confidence in me that has led me to my successes. He believed in my abilities even when I was unsure of myself, and I could never express enough how much that has meant to me.

I would also like to thank my committee members; Dr. Harvey, Dr. Hud, Dr. Williams, and Dr. Wartell. My interactions with them in the classroom as a young grad student, and in RiboEvo later in my graduate career, have been an absolute joy. The enthusiasm with which these gentlemen approach science has left a lasting mark on me. I must also thank them for the confidence they have had in me over the years, for it has allowed me to truly become confident in myself as a chemist.

Appreciation must also be given to my family and close friends. Even though they may not have fully understood exactly what I was doing in the lab, they always showed me support and praise.

Thanks are also due to my lab family, both past and present, in the Oyelere Lab. We have shared the greatest joys and the deepest sorrows together. The tragic loss of Dereck Benicewickz will forever be a reminder of just how precious life is. Despite this heartache, seldom a day passed in wing 3A where laughter was not heard from the Oyelere Lab benches, and for that I am most grateful. Each and every member holds a special place in my heart and I wish them nothing but the best.

I must also thank my wonderful future wife, Ms. Tiffany Livingston, for coming back into my world at exactly the right time and cheering me on during my final years of grad school. Her endless love, understanding and encouragement have been a catalyst in the progression of my life.

I would like to dedicate this thesis to my grandmother, Beverly Jean Sprinz. Grandma Bevy was diagnosed with stage 4 non-small cell lung cancer in December of 2010. As of the completion of this manuscript in July of 2012, she is losing the battle against this horrible disease. Despite her pain, she has managed to always keep a smile on her face and a sense of humor about her. Her strength through this struggle will always serve as inspiration to me in whatever life may throw my way.

TABLE OF CONTENTS

	Page
ACKNOWLEDGEMENTS	iii
LIST OF TABLES	viii
LIST OF FIGURES	ix
LIST OF SCHEMES	xi
LIST OF SYMBOLS AND ABBREVIATIONS	xii
SUMMARY	xiv
CHAPTER	
1 Introduction	1
1.1 RNA Structural Motifs Involved in Binding	1
1.2 Targeting the Ribosome	12
1.3 References	21
2 Interaction of Anthracyclines with Iron Responsive Elements mRNAs	30
2.1 Introduction	30
2.2 Anthracycline Antibiotics	31
2.3 Iron Metabolism and Regulation via Iron Responsive Elements	33
2.4 Biophysical Characterization of Anthracycline/IRE RNA Interaction	35
2.5 Discussion	49
2.6 References	56
3 Preferential Binding of Anthracyclines to DNA Mismatch Base Pairs	63
3.1 Known DNA / Anthracycline Interactions	63
3.2 Biophysical Characterization of Anthracycline / Hairpin DNA Interaction	66

3.3 Discussion 78

3.4 References 82

4 Exploring the Ribosome with Novel Macrolide-Peptide Conjugates 92

4.1 Architecture of the Ribosomal Exit Tunnel 92

4.2 Peptolide Design and Synthesis 93

4.3 *In vitro* Cell Extract Inhibition Assays 97

4.4 Chemical Footprinting 99

4.5 Discussion 105

4.6 References 111

5 Characterization of Novel Topoisomerase II / Histone Deacetylase Inhibitor Conjugates: Nucleic Acid Binding Properties 114

5.1 Introduction 114

5.2 Rational Design of TopoII / HDACi Conjugates 115

5.3 *In vitro* HDAC Inhibition 121

5.4 *In vitro* TopoII Decatenation 124

5.5 *In vitro* Cell Growth Inhibition 126

5.6 Intracellular TopoII Inhibition 129

5.7 Cellular Localization 132

5.8 Interaction of Conjugates With DNA and RNA 134

5.9 Discussion 139

5.10 References 142

6 Molecular Architecture of Zinc Binding Small Molecules that Inhibit Splicesome Assembly 151

6.1 Introduction 151

6.2 Screening of Structurally Diverse HDACi for Splicing Inhibition 155

6.3 Conclusions 167

6.4 Materials and Methods 168

6.5 References 170

7 Conclusions and Future Directions 174

APPENDIX A: Supplemental Information for CHAPTER 2 175

APPENDIX B: Supplemental Information for CHAPTER 5 190

VITA 191

LIST OF TABLES

Page

Table 2.1: Melting Temperature Data for IRE RNAs in the Absence and Presence of Anthracyclines 39

Table 2.2: Apparent Dissociation Constants for DOX and IRE RNAs 43

Table 3.1: Melting Temperature Data for DNA Mismatch Hairpins and Anthracyclines 70

Table 4.1: Peptolide IC_{50} Values For Cell Free Translation Inhibition Assays 98

Table 5.1: *In Vitro* HDAC Inhibition of TopoII / HDACi Conjugates 123

Table 5.2: Cell Viability Assay of TopoII / HDACi Conjugates 128

Table 5.3: Melting Temperature Data and Stern-Volmer Constants for TopoII / HDACi Conjugates and DNA 137

Table 5.4: Melting Temperature Data for TopoII / HDACi Conjugates and RNA 137

Table 6.1: Structure Activity Relationship and Splicing Inhibition of Novel Zinc Binding Compounds 158

LIST OF FIGURES

Page

Figure 1.1: Crystal Structures of B-DNA and A-RNA 3

Figure 1.2: Crystal Structure of DOX Bound to DNA 4

Figure 1.3: Crystal Structure of Cisplatin Bound to DNA 5

Figure 1.4: Representative Secondary Structure Elements found in RNA 7

Figure 1.5: Crystal Structure of tRNA 8

Figure 1.6: Hammerhead Ribozyme Mechanism and Conserved Structural Features 10

Figure 1.7: Diagram of the 70S Ribosomal Subunit 13

Figure 1.8: Crystal Structure of Linezolid Bound to 50S Ribosome 16

Figure 1.9: Representative Structures of the Macrolide Antibiotic Family 17

Figure 1.10: Crystal Structure of Erythromycin and Telithromycin Bound to the 50S Ribosomal Subunit 18

Figure 1.11: Position of Residue A2058 in Relation to Bound Macrolide 19

Figure 2.1: Structures of IRE RNAs and Anthracyclines 34

Figure 2.2: UV Melting Profile of IRE RNA and DOX 38

Figure 2.3: Absorbance and Fluorescence Profiles and Stern-Volmer Plot for IRE RNA and DOX 41

Figure 2.4: Job Plot Analysis of IRE RNA and DOX 44

Figure 2.5: RNase T1 Footprinting of IRE RNA in Absence and Increasing Concentration of DOX 47

Figure 3.1: Hairpin DNA Construct and Anthracyline Structure 64

Figure 3.2: Circular Dichroism of Wild Type and Mutant Hairpin DNA in Absence and Presence of DOX 72

Figure 3.3: Stern-Volmer Analysis of Hairpin DNA Constructs Bound to DOX 75

Figure 3.4: Negative ESI-Mass Spectrometry of Hairpin DNA Bound to DOX 76

Figure 3.5: Relative Binding Percentages of DOX Bound to DNA as Determined by ESI-Mass Spectrometry 77

Figure 4.1: Macrolide Binding Pocket 93

Figure 4.2: Crystal Structure of Telithromycin Bound to Three Unique 50S Ribosomal Subunits 94

Figure 4.3: Modification of Telithromycin to Yield Peptolides 95

Figure 4.4: Synthetic Scheme for Peptolides 96

Figure 4.5: DMS Chemical Footprinting Analysis of 23S rRNA with Primer 2180 103

Figure 4.6: CMCT Chemical Footprinting Analysis of 23S rRNA with Primer 2180 104

Figure 4.7: Crystal Structure Indicating Location of Footprinted Residue U1963 With Respect to Bound Macrolide 108

Figure 5.1: Structure of Representative Anthracycline Antibiotics 117

Figure 5.2: Design of Dual Acting TopoII / HDACi Conjugates 118

Figure 5.4: Topoisomerase II Decatenation of KDNA Assay of TopoII / HDACi Conjugates 125

Figure 5.5: Intracellular TopoII Inhibition of TopoII / HDACi Conjugates Slot Blot 131

Figure 5.6: Fluorescence Microscopy Demonstrating Cellular Localization of TopoII / HDACi Conjugates 133

Figure 5.7: RNA and DNA Constructs Used to Determine Nucleic Acid Binding Characteristics of TopoII / HDACi Conjugates 134

Figure 5.8: Stern-Volmer Plot of TopoII / HDACi Conjugates Bound to DNA 138

Figure 6.1: Prototypic HDAC Inhibitor 155

Figure 6.2: MINX pre-mRNA Splicing Inhibition Assay 157

Figure 6.3: Restoring Splicing by Adding Zn to MINX Assay 165

LIST OF SCHEMES

Page

Scheme 5.1: Synthesis of SAHA-based TopoII / HDACi Conjugates 119

Scheme 5.2: Synthesis of SAHA-based Triazole Linked TopoII / HDACi Conjugates 120

LIST OF SYMBOLS AND ABBREVIATIONS

ATP	Adenosine Triphosphate
BPE	Bisphosphate EDTA Buffer
CD	Circular Dichroism
CMCT	1-cyclohexyl-(2-morpholinoethyl)carbodiimide metho-p-toluene sulfonate
DAU	Daunorubicin
ddNTP	Dideoxy Nucleotide Triphosphate
DMS	Dimethyl Sulfate
DMSO	Dimethyl Sulfoxide
DNA	Deoxyribonucleic Acid
dNTP	Deoxy Nucleotide Triphosphate
DOX	Doxorubicin
DTT	Dithiothreitol
EDTA	Ethylenediaminetetraacetic Acid
erm	Erythromycin Ribosome Methylase
ESI-MS	Electrospray Ionization Mass Spectrometry
HDAC	Histone Deacetylase
HDACi	Histone Deacetylase Inhibitor
HHR	Hammerhead Ribozyme
IRE	Iron Responsive Element
IRP	Iron Regulatory Protein
KDNA	Kinetoplast DNA
LIN	Linezolid
MMR	Mismatch Repair

mRNA	Messenger RNA
pre-mRNA	Precursor mRNA
PTC	Peptidyl Transferase Center
RNA	Ribonucleic Acid
RNAi	RNA Interference
RNP	Ribonucleoprotein
rRNA	Ribosomal RNA
SAR	Structure Activity Relationship
snRNP	Small Nuclear Ribonucleoprotein
TBE	Tris Borate EDTA Buffer
TEL	Telithromycin
TopoII	Topoisomerase II
tRNA	Transfer RNA
UTR	Untranslated Region
UV-vis	Ultraviolet Visible

SUMMARY

Nucleic acids have proven to be viable targets for small molecule drugs. While many examples of such drugs are detailed in the literature, only a select few have found practical use in a clinical setting. These currently employed nucleic acid targeting therapies suffer from either debilitating off-target side effects or succumb to a resistance mechanism of the target. The need for new small molecules that target nucleic acids is evident. However, designing a novel drug to bind to DNA or RNA requires a detailed understanding of exactly what binding environments each nucleic acid presents. In an effort to broaden this knowledge, the work presented in this thesis details the binding location and affinity of known and novel nucleic acid binding small molecules with targets ranging from simple RNA secondary structure all the way to the complex structure of ribosomal RNA. Specifically, it is shown that the anthracycline class of antineoplastics prefer to bind at or near mismatch base pairs in both physiologically relevant iron responsive element RNA hairpin constructs as well as DNA hairpin constructs presenting mismatched base pairs. Also characterized in this thesis is a novel class of topoisomerase II / histone deacetylase inhibitor conjugates that display a unique affinity for DNA over RNA. Finally, the novel class of macrolide-peptide conjugates, known as peptolides, are shown to retain potent translation inhibition of the prokaryotic ribosome. The binding pocket of the peptolides, including a crevice previously unreachable by macrolides that extends away from the peptidyl transferase center toward the subunit interface, is confirmed in detail via chemical footprinting of the 70S ribosome. Overall, the identification of a novel binding site for the anthracycline class of

drugs and the characterization of the two novel drug designs presented in this thesis will undoubtedly aid in the effort to design and discover new molecules that aim for nucleic acid targets. For example, the anthracycline derivative topoisomerase II / histone deacetylase inhibitor conjugates, with their differential mode of nucleic acid binding, may prove to have a unique side effect profile in a therapeutic application. The peptolide compounds also have the potential to be applied as novel antibiotics as they bind to an area of the prokaryotic ribosome unrelated to known macrolide resistance mutations. Furthermore, as a result of the observation of this thesis work that some peptolides also posses eukaryotic translation inhibition capabilities, they could prove to be useful in preventing the growth of rapidly proliferating eukaryotic cells such as plasmodium, leishmania, or tumor cells. Additionally, different head groups could be utilized in creating new peptolides; for example, an oxazolidinone antibiotic could be employed to sample a different binding area of the ribosome.

CHAPTER 1: INTRODUCTION

1.1 RNA Structural Motifs Involved in Binding

In recent decades, nucleic acids have been shown to be not merely the scribes of the genetic and proteomic code, but they have also been revealed to play crucial roles in regulating genes and gene products via interaction with a variety of ligands including other nucleic acids, proteins, metabolites, cofactors, enzymes, and small molecules (1-11). Prior to this realization, proteins were the main targets of a medicinal chemistry campaign to identify novel small molecules with therapeutic potential. With the successful sequencing of the human genome, hopes were high that all proteins in the human body could be identified and subsequently many new ones could become the target for the treatment of diseases. This, however, has not panned out as only 15% of the human proteome has been deemed drugable and only 207 proteins are targeted by current FDA approved small molecule drugs (12, 13). Many of these clinically successful drugs share the trait of mimicking a protein partner in a protein-protein interaction as their primary mode of action (14, 15). Due to the large surface area and relative complexity of these interactions, it has proven to be a very difficult endeavor to target proteins with small molecules for therapeutic application. This has emphasized the importance of being able to target the source of the protein product related to a disease state, the DNA and RNA encoding it, as a means of treatment. There have been relatively few successful cases of directly targeting DNA in a clinical setting. The most notable success stories would be the alkylating antineoplastic agents such as nitrogen mustards, nitrosoureas, and alkyl sulfonates as well as the cisplatin and anthracycline families of chemotherapeutics (16-19). With an even more underwhelming representation is the effort to develop treatments exploiting RNA as the target, excluding of course ribosomal RNA-targeting antibiotics. While RNAi holds great promise as a means to

target specific nucleic acid sequences, the difficulty in delivering the small RNA constructs to the target has hindered its application in a clinical setting (20-21). Efforts are concurrently underway by multiple labs to develop not only a clear understanding of how nucleic acids react and bind to small molecules drugs, but also to identify and characterize novel nucleic acid binders in both a high-throughput and a rationally-driven design basis (22-24).

In order to facilitate this search for novel nucleic acid targeting small molecules, a thorough understanding of what a nucleic acid binding site has to offer to a small molecule is needed. This can be gleaned by examining the secondary and tertiary structures formed by doth DNA and RNA and by considering several examples of drugs that have successfully pinpointed nucleic acids in a clinical setting. DNA and RNA share a similar structure in that they both form a duplex of phosphate backbone linked nucleosides stitched together in a helical arrangement by base pairs between adjacent, anti-parallel strands. However, due to the unique sugar pucker restrictions of RNA owing to its additional 2` hydroxyl group, duplex RNA in a physiological environment presents a much different helical structure in three dimensions than DNA (Figure 1.1). The typical B-form DNA found inside the cell presents a wide yet shallow major groove and a narrow but deep minor groove.

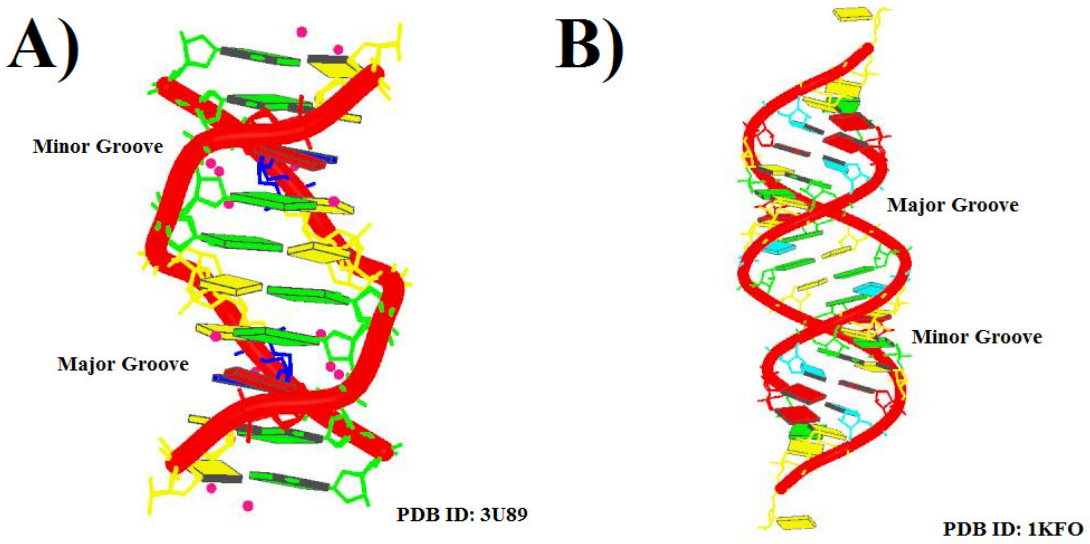

Figure 1.1 A) Crystal structure of the typical B-DNA helix. B) Crystal structure of typical A-RNA helix. (25, 26)

The width of the major groove allows for easy access to the hydrogen bond participant and pi-stacking rich core of the DNA duplex by small molecules. The deep and narrow nature of the minor groove presents a hydrophobic and densely electronegative rift for small electropositive molecules. The binding of daunorubicyn (DAU), a member of the anthracycline class of anti-tumor drugs that also includes doxorubicin (DOX), to B-DNA clearly illustrates the two main non-covalent binding modes of small molecules to a nucleic acid target: minor groove binding and intercalation (Figure 1.2).

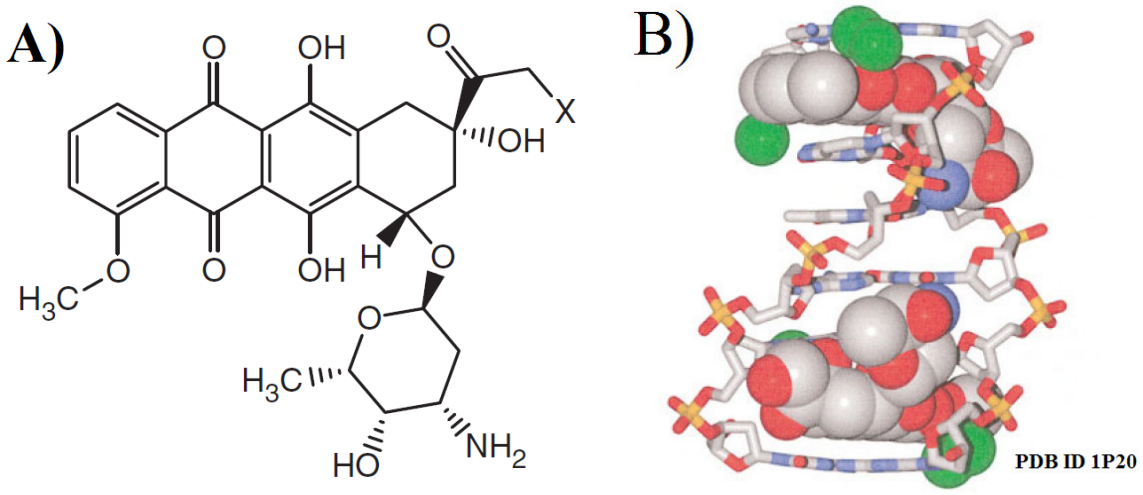

Figure 1.2) A) General skeleton of the anthracycline class of drugs; DAU X=H, DOX X=OH. B) Crystal structure of two molecules of DAU (sphere) bound to B-DNA helix (stick) (27).

The flat, conjugated ring system of the aglycone moiety of DAU slips snuggly in between adjacent base pairs of the DNA helix (Figure 1.2B). It is this favorable intercalation that has been attributed to the anthracycline family's strong binding preference for DNA (28-36). Further stabilizing the interaction, the amino sugar moiety is presented to the minor groove where it binds firmly via electrostatic interactions (27).

An example of a covalent small molecule interaction with DNA can be found with the chemotherapeutic cisplatin (Figure 1.3). Cisplatin is a platinum containing molecule that upon administration looses one of its chlorine atoms to water displacement. This water molecule, also an excellent leaving group, allows the platinum atom to readily bind to bases in the DNA helix, preferably G residues. The second chlorine atom is subsequently displaced, causing an intrastrand cross link between adjacent G residues. This crosslinking causes a distortion of the helix (Figure 1.3B) that is recognized by the DNA repair pathway but cannot be undone, thus signaling cell death. From these examples it is clear that while DNA is certainly druggable, its

confined nature in the cell, wound tightly around histone complexes in the nucleus, has made it difficult to directly target with but a few successful clinical applications. Even the success stories such as anthracyclines and cisplatin are plagued by systemic toxicity and off-target side effects, thus leaving much room for improvement.

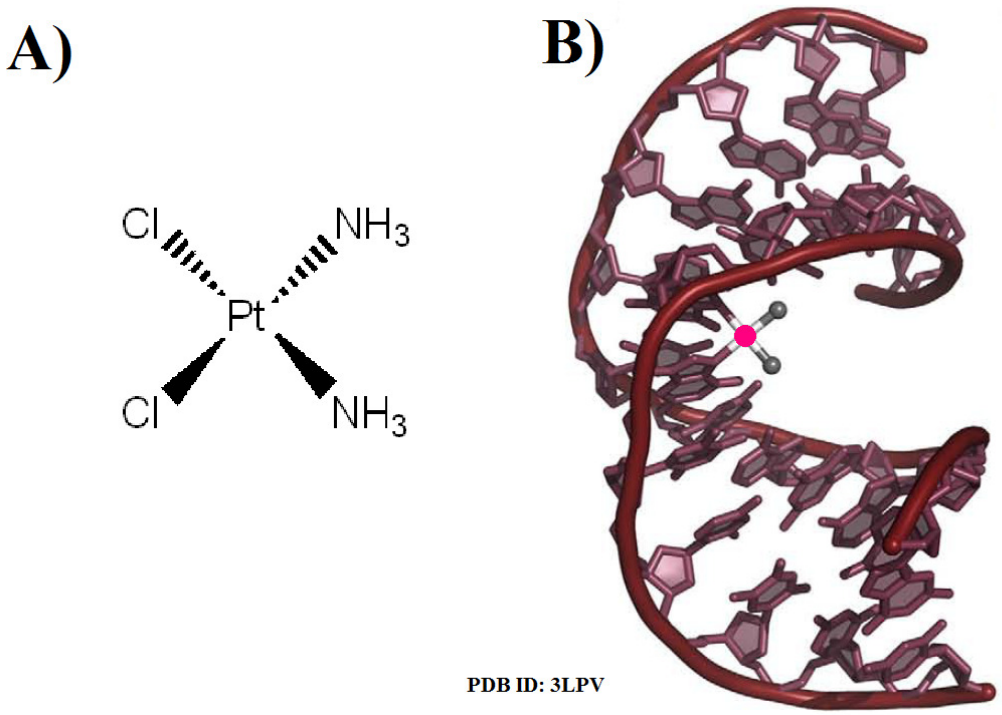

Figure 1.3 A) Structure of Cisplatin B) Crystal structure of cisplatin (Pt is pink sphere near center) covalently bound to a B-DNA helix. Figure adapted from (37).

Conversely, RNA is ubiquitous in both the nucleus and cytoplasm and readily accessible to small molecule invaders of the cell. However, a survey of RNA's secondary structuring highlights a dissimilar topology to that of DNA described above. With its fixed C-3` endo ribose pucker, RNA presents an A-form helix inside the cell (Figure 1.1B). Unique to the A-form helix are its distinct groove characteristics. The major groove of A-RNA is wider than the minor

groove, but recent results have indicated that it is too narrow to accommodate small molecule binding (38). This is unfortunate since the major groove is rich with small molecule luring functional groups along the Hoogsteen edges of the base pairs (39). The minor groove of the A-form RNA helix is both shallow and narrow, thus appearing to be a less alluring interaction site for a small molecule ligand than the inviting grooves of the B-DNA helix.

The seemingly constrained and minor groove-inaccessible conformation of the A-RNA duplex helix is not indicative of its ability to form complex tertiary structures. In fact, RNA has the gymnastic ability to form some of the most complex binding motifs found inside the cell (39). It owes this flexibility to several key differences from its DNA counterpart. DNA for the most part exists as a duplex of individual strands. This dictates that the DNA always be paired to its compliment in what tends to be a very strict, canonical Watson-Crick base pairing fashion. In contrast, RNA exists almost entirely as a single stranded entity, save of course for its time spent paired with its molecular role model in a DNA:RNA hybrid. As a result of its inherent single strandedness, RNA is left to fold back upon itself in a complimentary fashion. Without a strict compliment for the RNA strand, very unique and complex structures arise from the lone RNA strand searching for its lowest entropic energy state with only itself, water, and a few metal ions to rely on. Some of the most commonly observed secondary structures found to be conserved in molecular recognition in an RNA-ligand binding event are presented in Figure 1.4.

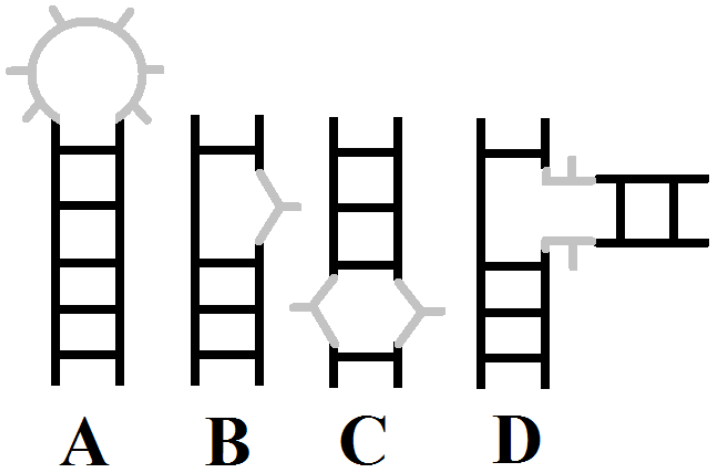

Figure 1.4 Some of the conserved and unique secondary structures found in RNA-ligand interactions. A) hairpin loop B) single base bulge C) mismatch bulge D) multi stem junction

Despite its limiting features as a strict A-form helix, the building blocks presented in Figure 1.4 are just a few of the features that RNA employs to engineer incredibly complex secondary and tertiary structure. The hairpin loop allows the RNA strand to make sharp turns back onto itself, the bulges allow for symmetrical and asymmetrical disregard of any unruly bases not wanting to pair, and the multi-way junction allows multiple, distinct regions of functionality to bud and branch out of the same single strand of RNA (39, 40). Another factor contributing to the structural plasticity of RNA is the high incidence and tolerance of mismatched base pairs. Unlike DNA, RNA does not have a housekeeping repair pathway to clean up mismatched pairs. While a base mismatch in DNA has the possibility to corrupt the genome and must be corrected swiftly, the mismatch pair in RNA is employed as a point of flexibility in the tertiary structure. In fact, mismatch pairs are often also a conserved feature in RNA recognition motifs (41). The base-pair mismatch distorts the shape of the A-RNA helix. This distortion kinks and partially unwinds the otherwise inaccessible helix, thus widening the

major groove and opening up an electronegative pocket offering an inviting home to any number of small molecule binders.

An elegant example of all of these highly emancipating structural features coming together to form a macromolecule important to all known life can be found in the structure of transfer RNA (tRNA). When the crystal structure of yeast $tRNA^{PHE}$ was solved for the first time in 1974 it revealed an incredible number of structural features made from only a 76-nt long RNA strand (42, 43). As crystallographic resolution improved over the coming decades, even more structural characteristics were gleaned from the similar E. coli $tRNA^{PHE}$ (Figure 1.5).

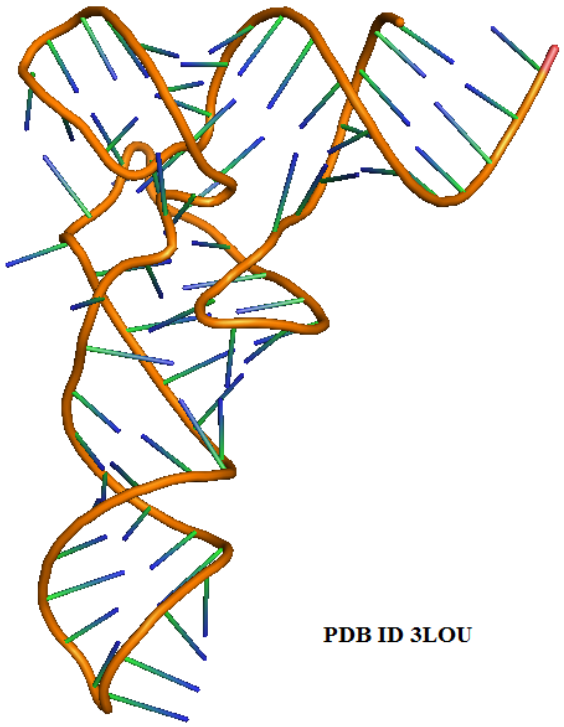

Figure 1.5 Cyrstal structure of $tRNA^{PHE}$ flaunting its many structural motifs unique to RNA (44).

In this single, relatively short tRNA there exist a number of secondary and tertiary interactions serving to hold the oligo in exactly the correct orientation to recognize and selectively deliver charged amino acids to the ribosome for incorporation into the nascent polypeptide chain. Some

of these interactions include non-canonical base pairs, hairpins, 10 modified bases, and a complex three way stem junction held together by a number of base-triple pairs (44). Additionally there are a number of water molecules and divalent Mg^{2+} ions helping to stabilize tertiary interactions (44). It is truly remarkable to recognize just how many special building blocks were taken from the RNA engineering tool kit to create and conserve an RNA motif capable of recognizing its binding partner with such high fidelity.

An equal marvel of RNA structural complexity and ligand recognition can be found in the enzymatically active class of RNAs known as ribozymes. Prior to the discovery of the first ribozymes, enzymatic ability had been relegated solely to protein enzymes. It was the discovery of this class of self cleaving RNA structures that opened the doors for the RNA world theory; it was now possible for RNA to posses characteristics of both the chicken and the egg (the encoder of heredity and the enzymatic catalyst) in the long-lived debate over which came first in the origin of life, RNA or DNA. It was the complex tertiary structures observed in crystal structures of tRNA that led to the hypothesis that this was indeed feasible as early as the late 1960's. Proof did not come until the late 1970's via work by Thomas Cech involving a self-splicing RNA fragment and work by Sydney Altman on the discovery of the auto-catylytic RNase P (45-47). Cech and Altman shared the 1989 Nobel Prize in Chemistry for their contribution to the discovery that RNA was not just a molecule of heredity, but that it was more importantly a biocatalyst (48). Ribozymes have been shown to be capable of several types of enzymatic reactions without the need for cofactors such as adenosine triphosphate (ATP). The most common of these enzymatic capabilities is the cleavage of its own phosphodiester backbone via a transeserification reaction, as found in, for example, the hammerhead ribozyme (HHR) family (Figure 1.6A). The structural characteristics of HHR ribozymes are unique and have been found

to be conserved in one form or another in all three boughs of the tree of life (49). A close look at the secondary and tertiary structure of HHRs again highlights the complexity attainable by the ribonucleic acid polymer (FIG 1.6B&C).

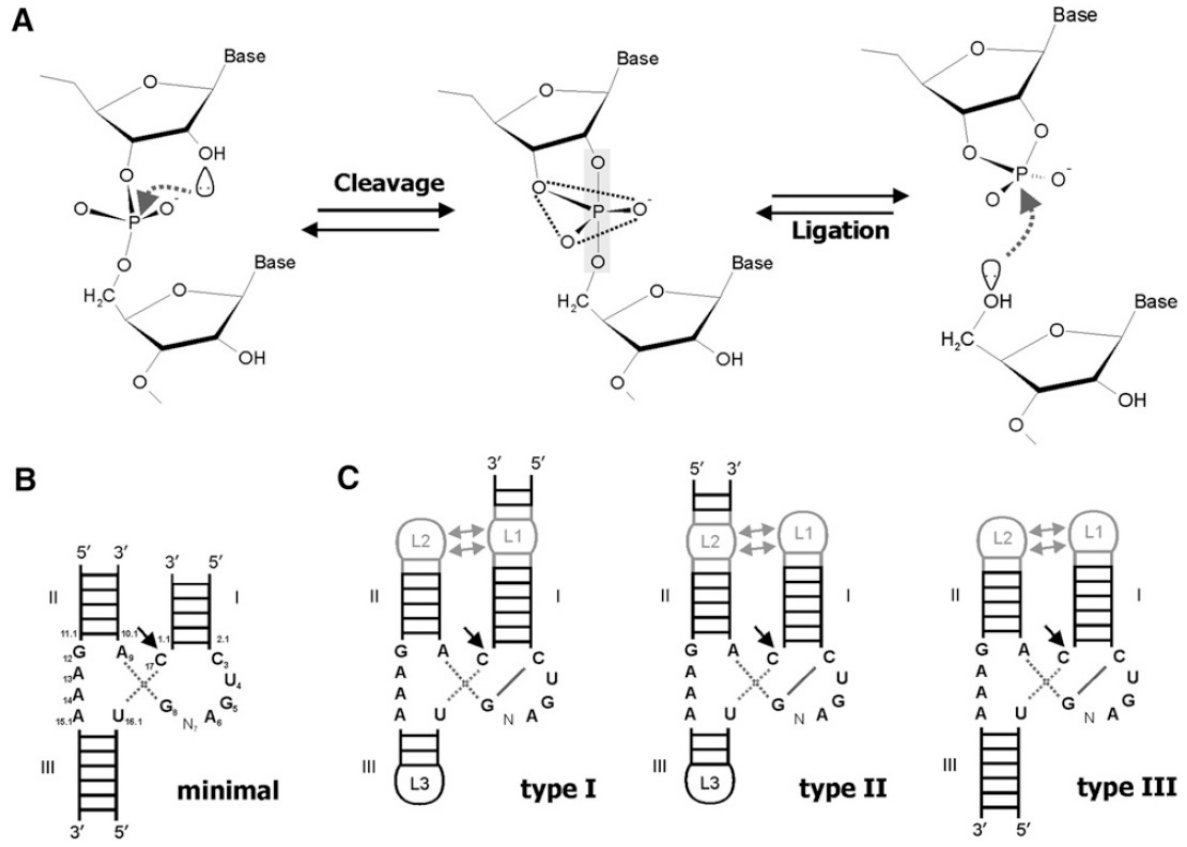

Figure 1.6 A) The self catalyzed S_N2 mechanism by which the ribozyme cleaves its own backbone. B) The minimal structure of the HHR catalytic core. The site of cleavage is indicated by the arrow. C) The three types of complete HHR configurations known to be active under physiological conditions. Figure adapted from (49).

Of the known types of existing HHR catalytic cores, the same general secondary and tertiary design elements remain constant: three helical segments held in precise alignment with respect to one another via tertiary interaction between conserved residues. While the minimal catalytic core has been shown to be active in vitro (Figure 1.6B), it has been shown that in vivo activity requires that the additional loop regions found in types I-III of the HHR are essential to

function (50-51). This is a testament to the absolute precision with which these ribonucleic acid based enzymes have evolved. Perhaps the most awe inspiring feat of RNA secondary structure can be found in what amounts to the most sophisticated ribozyme found in life, and the subject of the next section of this manuscript: the ribosome.

1.2 Targeting the Ribosome

The most successfully targeted nucleic acid to date has undoubtedly been ribosomal RNA (rRNA). In fact, nearly all current FDA approved RNA targeting therapeutics are antibiotics specifically targeting the RNA component of the bacterial ribosome (52-54). The ribosome is one of the most sophisticated and complex macromolecular machines ever discovered and thus may seem to be a daunting target for any rationally designed therapeutic. However, with a thorough understanding of its components, assembly, and function coupled with an appreciation of previously examined rRNA-targeting drugs, the ribosome becomes much less intimidating prey for a stalking small molecule. The ribosome is the cell's protein assembly line and is required for life across all three branches of the phylogenetic tree. This peptide production facility reads the triplet code embedded in the messenger RNA (mRNA), which has been transcribed from genomic DNA, and utilizing a multitude of cofactors diligently adds each additional amino acid residue to a growing nascent peptide chain utilizing tRNA as its molecular supplier of charged amino acids. While the catalytic core of the ribosome has very high conservation amongst all life forms, the composition and overall structure of the entire ribosome varies between archaea, eukaryota and bacteria. As the bacterial ribosome is the target of the antibiotics that will be discussed later, only its structure will be detailed here.

The prokaryotic ribosome in its entirety is known as the 70S unit, owing its name to the particle's sedimentation coefficient in Svedberg units (S). This 70S ribosome is comprised of two smaller components known as the 50S and 30S subunits. The 50S subunit consists of about 30 ribosomal proteins as well as the 5S and 23S rRNA strands while the 30S subunit contains the 16S rRNA and around 20 ribosomal proteins. An overall model of the ribosome can be found in Figure 1.7.

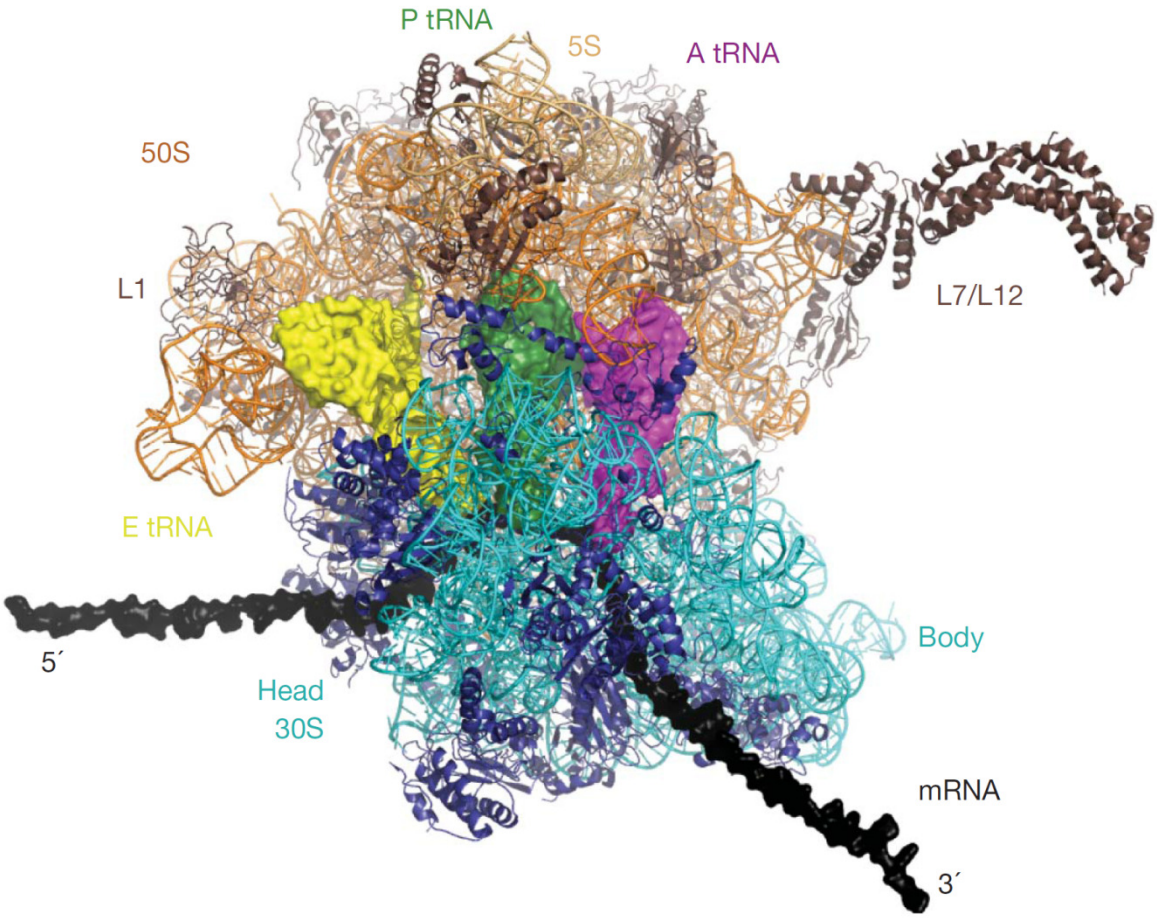

Figure 1.7 Model detailing the relative positions of all major components of the 70S ribosome. Figure adapted from (55).

The interface between 50S and 30S subunits is made almost entirely from rRNA and serves as the catalytic core of the ribosome. The 30S subunit is responsible for binding to the mRNA and subsequently proof reading each added amino acid. It is the purpose of the 50S subunit to serve as the site of peptide bond formation. This catalytic core, contained mostly in the 50S but extending into the 30S as well, is comprised of three distinct binding sites for incoming tRNAs: the A-site, P-site, and E-site. These three positions and the surrounding area are known together as the peptidyl transferase center, or PTC. The A site of the PTC serves as the premier binding position for incoming aminoacyl tRNAs laden with their amino acid cargo. The next position for

this inbound tRNA is the P site, where the peptidyl transfer and bond formation will actually occur. The tRNA's bound amino acid residue is ligated to the growing nascent polypeptide. Once relieved of its passenger, the tRNA then enters the E site where it exits the PTC and ribosome. To accommodate the structural rearrangements necessary for tRNAs to move from one site to the next, a large scale, concerted shift in overall ribosomal structure causes a ratcheting movement of the 50S and 30S subunits with respect to one another. As tRNAs shuttle in and out of the ribosome creating an ever longer peptide, the growing polypeptide makes its own egress from the ribosome through a long narrow passage in the 50S subunit known as the exit tunnel. A detailed understanding of the interworking of the ribosome is a relatively new revelation. It was not until 2000 that several high resolution crystal structures were solved simultaneously (56-59). Venkatraman Ramakrishnan, Thomas Steitz, and Ada Yonath shared the 2009 Nobel Prize in Chemistry for contributions allowing this intimate glimpse into the ribosome (60).

Once the structural specifics of the target are known it is then instructional to look at drugs that have successfully targeted rRNA. With the many moving parts that are perfectly synchronized like tight fitting cogs in the impressive macromolecular machine of the ribosome, it is clear that a small molecule binding anywhere in the machinery could prove to be disastrous to the fidelity of the translational process. In fact, there exist several examples of clinically utilized antibiotic families that inhibit translation by doing exactly that, binding to the ribosome and stalling the gears. Two examples of more recent, broad spectrum antibiotics targeting rRNA of penicillin resistant bacteria can be found in the oxazolidinone and anthracycline families of drugs. Linezolid (LIN), the premier member of the oxazolidinone class of antibiotics, gained FDA approval for treatment of severe infections resulting from antibiotic resistant, gram-positive bacteria (61). The overall structure of LIN includes three rings, the most important being the 2-

oxazolidone ring decorated with an acetamedomethyl tail moiety having an S-configuration (Figure 1.8A). Early on it was discovered that Lin owes its strong bacteriostatic nature to the ability to inhibit the initiation step of protein synthesis (62). By binding to the 50S subunit of the ribosome prior to ribosomal assembly, LIN affectively prevents the binding of the large and small subunits together along with $tRNA^{fMet}$, thus preventing initiation. Looking to the crystal structure of LIN bound to the 50S subunit it becomes apparent why the small molecule has found such a suitable binding pocket amongst the rRNA (63). As can be seen in Figure 1.8B, the ring systems of LIN nestle in amongst the bases of the 23S rRNA strand yielding 5 van der Waals interactions as well as a direct hydrogen bond to residue G2540. The stacking of C2487, LIN, and U2541 is an excellent example of pi-pi stacking contributing to the binding affinity of a small molecule for RNA. In Figure 1.8B the binding position of a P-site binding analogue, CCA-*N*-acetylphenylalanine (CCA-Phe), can also be seen. Using CCE-Phe as a landmark it becomes clear that LIN is binding in the direct vicinity of the A-site. This interference in the heart of the PTC is what leads to LIN's ability to inhibit prokaryotic protein synthesis. Further studies have also indicated that LIN has the ability to bind in the P-site and directly interact with the first few residues of the nascent chain, furthering its devastating capabilities inside the 50S subunit (64).

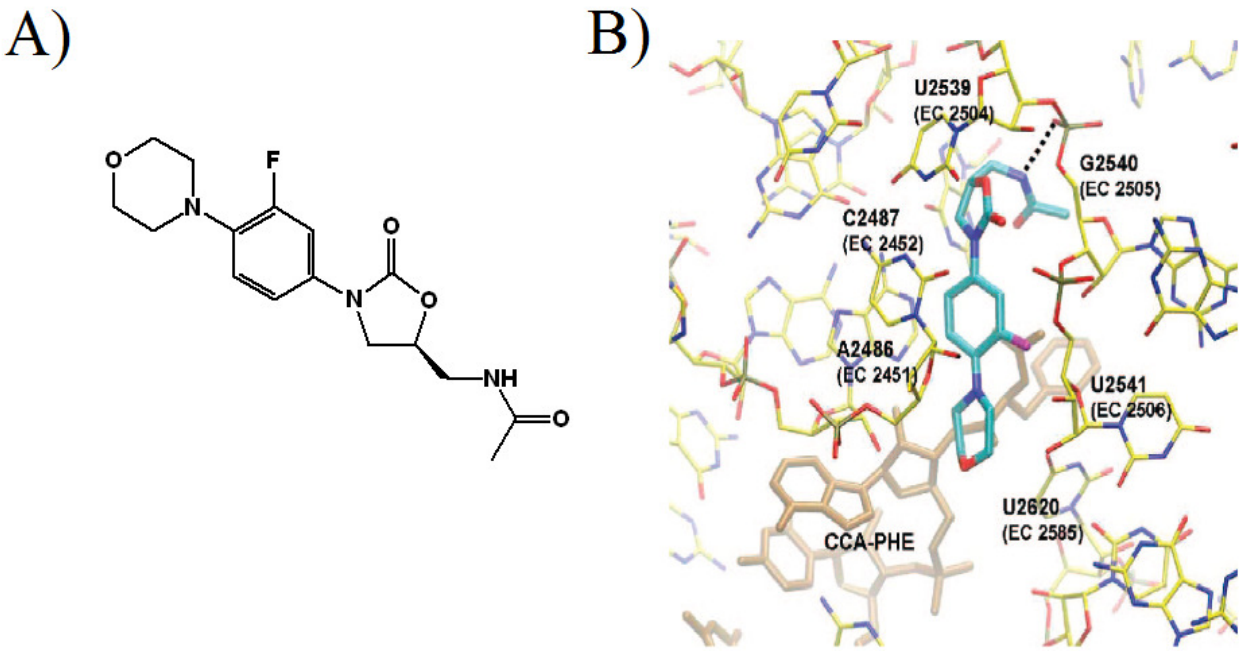

Figure 1.8 A) Structure of Linezolid (LIN). B) Crystal structure of LIN bound to the 50S subunit of *Haloarcula marismortui*. Labeled residues indicate positions of van der Waals interaction with the LIN molecule. The dashed line denotes a hydrogen bond to G2540. Figure adapted from (63).

While the oxazolidinone family has only one FDA approved drug in LIN, the much more clinically applicable macrolide class of antibiotics boasts a long list of approved compounds including azithromycin, clarithromycin, erythromycin and telithromycin. These and other macrocyclic antibiotics have been widely used to treat gram-positive bacterial infections across the globe for almost 60 years (65). Unique to this class of compounds is their tissue selective accumulation in the lungs, making them ideal for treating infections of the respiratory tract. Macrolide antibiotics share a similar macrocyclic skeleton, found in 13-17 member varieties, and have various sugars and other functional groups attached as appendages (Figure 1.9). Common to all members of the macrolide family is their binding location in the prokaryotic ribosome known as the macrolide binding pocket. This binding pocket lies at the interface of the 50S and

30S subunits directly adjacent to the PTC A- and P-sites (Figure 1.10). This site of interaction lies directly between the PTC and the intended path of the nascent peptide chain through the exit tunnel.

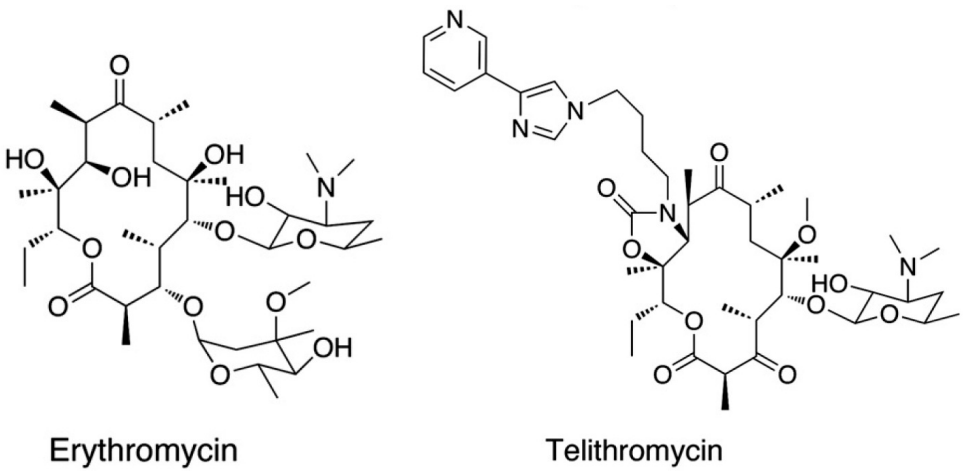

Figure 1.9 Representative structures of the macrolide class of antibiotics.

It is this high affinity binding to an rRNA target so close to the PTC, effectively blocking the exit tunnel, that has made the macrolide class of drugs so crucial to human health in recent decades. A testament to the specificity of this small-molecule / RNA interaction can be found in the most prevelant form of macrolide resistance mechanisms empoloyed by bacteria: rRNA methylation.

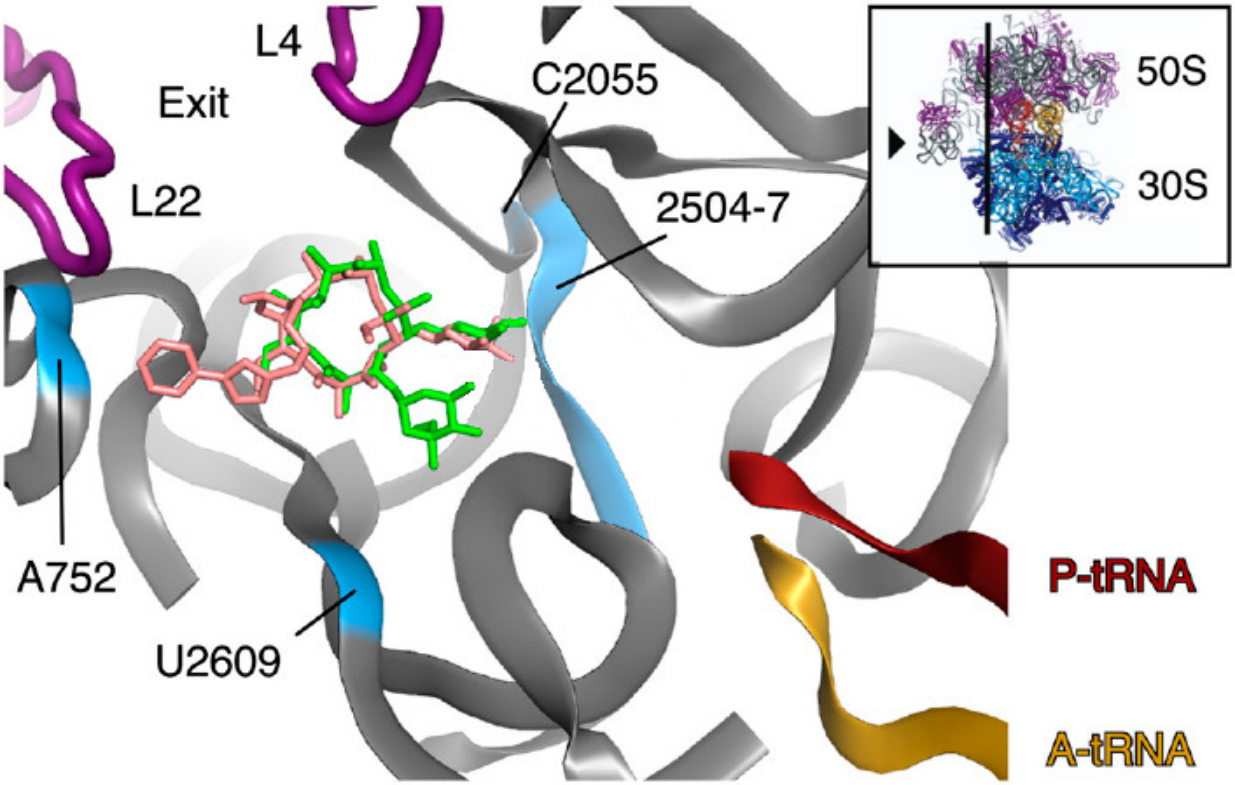

Figure 1.10 Crystal structures of erythromycin (green) and telithromycin (pink) bound to the *E. coli* 50S subunit. Figure adapted from (73).

Macrolide resistance in certain bacterial strains was observed soon after the clinical introduction of erythromycin in the 1950's (65). It was later understood that the mechanism behind this resistance was the bacteria's ability to methylate its own ribosome via a set of genes known collectively as the erythromycin ribosome methylase (*erm*) genes (66). Utilizing the enzymes encoded in the *erm* gene, bacteria can selectively methylate the 23S rRNA. One such modification that proves to be highly detrimental to macrolide binding is a dimethylation of residue A2058 (66). The adenosine at position 2058, according to *E. coli* numbering, is directly adjacent to the macrolide binding pocket and even participates in van der Waals interaction with the macrolide (Figure 1.11). It is this intimate proximity to the bound macrolide that makes the addition of two methyl groups to A2058 a devastating mutation yielding erythromycin resistant

strains of bacteria. The extra $CH_{3's}$ sterically preclude the macrolide from being able to bind to its designated pocket in the ribosome. Similar seemingly miniscule mutations to the 23S rRNA have also been shown to lead to oxazolidinone resistance in a similar fashion (67-72).

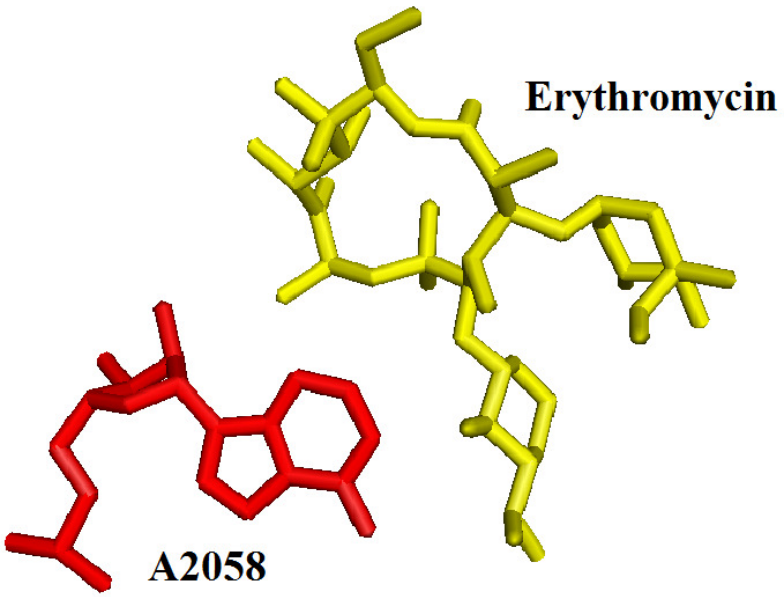

Figure 1.11 Crystal structure of erythromycin bound to the 50S subunit. Interaction with A2058 is crucial to erythromycin's ability to bind to the ribosome (73).

Of the strains of bacteria found in the hospital environment around the world, up to 75% of them (depending on geographical local) are both penicillin- and erythromycin-resistant (74). This staggering percentage, coupled with the fact that only three new classes of antibiotics have been approved by the FDA in the last 30+ years, intensifies the urgency with which novel rRNA targeting small molecules must be designed or discovered. Additionally, design of nucleic acid targeting small molecules as a whole could benefit greatly from a more thorough understanding of exactly what creates, and what disrupts, a suitable binding environment in DNA and RNA. It is the aim of this thesis to broaden the knowledge of small molecules that target nucleic acids.

These compounds include known and novel, rationally designed, small molecule drugs. Detailed in this thesis is the characterization of a never before described binding preference of anthracyclines for mismatch GU pairs in biologically critical RNA structures, a similar investigation of the preference of anthracyclines for mismatches in DNA, and the rational design and characterization of a novel class of anthracycline / histone deacetylase conjugate class of small molecule drugs. Also detailed in this thesis is the design, synthesis, and target validation of a novel class of macrolide / peptide conjugates designed to interrogate the binding environment of the ribosomal exit tunnel. It is with the utmost intention that the work presented in the following pages will serve to enrich the knowledge of nucleic acid binding small molecules with targets ranging from simple RNA secondary structure all the way to the complexities of ribosomal RNA.

1.3 References

1) 1) Tok,J., Cho,J. and Rando,R. (1999) Aminoglycoside antibiotics are able to specifically bind the 50- untranslated region of thymidylate synthase messenger RNA. *Biochemistry*, **38**, 199–206.
2) Thomas,J., Liu,X. and Hergenrother,P. (2005) Size-specific ligands for RNA hairpin loops. *J. Am. Chem. Soc*., **127**, 12434–12435.
3) Tibodeau,J., Fox,P., Ropp,P., Theil,E. and Thorp.,H. (2006) The up-regulation of ferritin expression using a small-molecule ligand to the native mRNA. *Proc. Natl Acad. Sci*., **103**, 253–257.
4) Xavier,K., Eder,P. and Giordano,T. (2000) RNA as a drug target: methods for biophysical characterization and screening. *Trends Biotechnol*., **18**, 349–356.
5) Bagalkot,V., Farokhzad,O., Langer,R. and Jon,S. (2006) An aptamer–doxorubicin physical conjugate as a novel targeted drug-delivery platform. *Angew. Chem. Int. Ed*., **45**, 8149–8152.
6) Mei,H., Cui,M., Heldsinger,A., Lemrow,S., Loo,J., Sannes-Lowery,K., Sharmeen,L. and Czarnik,A. (1998) Inhibitors of protein-RNA complexation that target the RNA: specific recognition ofhuman immunodeficiency virus type 1 TAR RNA by small organic molecules. *Biochemistry*, **37**, 14204–14212.
7) Leibold,E. and Munro,H. (1988) Cytoplasmic protein binds in vitro to a highly conserved sequence in the 50 untranslated region of ferritin heavy- and light-subunit mRNAs. *Proc. Natl Acad. Sci.USA*, **85**, 2171–2175.
8) Wagner EG, Altuvia S, Romby P. (2002) Antisense RNAs in bacteria and their genetic elements. *Adv. Genet.* **46**, 361-398.

9) Sevignani C, Calin GA, Siracusa LD, Croce CM. (2006) Mammalian microRNAs: a small world for fine-tuning gene expression. *Mamm Genome*. **17**, 189-202.

10) DeJong ES, Luy B, Marino JP. RNA and RNA-protein complexes as targets for therapeutic intervention.

11) Winkler WC, Breaker RR. (2003) Genetic control by metabolite-binding riboswitches. *Chembiochem*. **4**, 1024-32.

12) Hopkins AL, Groom CR. (2002) The druggable genome. *Nat Rev Drug Discov*. **9**, 727-30.

13) Overington JP, Al-Lazikani B, Hopkins AL. (2006) How many drug targets are there? *Nat Rev Drug Discov*. **12**, 993-6.

14) Fletcher S, Hamilton AD. (2005) Protein surface recognition and proteomimetics: mimics of protein surface structure and function. *Curr Opin Chem Biol*. **6**, 632-8.

15) Fry DC. (2008) Drug-like inhibitors of protein-protein interactions: a structural examination of effective protein mimicry. *Curr Protein Pept Sci*. **3**, 240-7.

16) Gilman, A. (1963) The Initial Clinical Trial of Nitrogen Mustard. *Am. J Surg.* **105**, 574-8.

17) Lin SH, Kleinberg LR. (2008) Carmustine wafers: localized delivery of chemotherapeutic agents in CNS malignancies. *Expert Rev Anticancer Ther*. **3**, 343-59.

18) Rebecca A. Alderden , Matthew D. Hall and Trevor W. Hambley. (2006) The Discovery and Development of Cisplatin. *J. Chem. Educ.*, **83**, 728.

19) Minotti G, Menna P, Salvatorelli E, Cairo G, Gianni L. (2004) Anthracyclines: molecular advances and pharmacologic developments in antitumor activity and cardiotoxicity. *Pharmacol Rev*. **56**, 185-229.

20) Rácz Z, Hamar P. (2006) Can siRNA technology provide the tools for gene therapy of the future? *Curr Med Chem*. **13**, 2299-307.

21) Lieberman J, Song E, Lee SK, Shankar P. (2003) Interfering with disease: opportunities and roadblocks to harnessing RNA interference. *Trends Mol Med*. **9**, 397-403.

22) Stelzer AC, Frank AT, Kratz JD, Swanson MD, Gonzalez-Hernandez MJ, Lee J, Andricioaei I, Markovitz DM, Al-Hashimi HM. (2011) Discovery of selective bioactive small molecules by targeting an RNA dynamic ensemble. *Nat Chem Biol*. **7**, 553-9.

23) Childs-Disney JL, Hoskins J, Rzuczek SG, Thornton CA, Disney MD. (2012) Rationally designed small molecules targeting the RNA that causes myotonic dystrophy type 1 are potently bioactive. *ACS Chem Biol*. **7**, 856-62.

24) Guerrant W, Patil V, Canzoneri JC, Oyelere AK. (2012) Dual targeting of histone deacetylase and topoisomerase II with novel bifunctional inhibitors. *J Med Chem*. **55**, 1465-77.

25) Maehigashi T, Hsiao C, Woods KK, Moulaei T, Hud NV, Williams LD. (2012) B-DNA structure is intrinsically polymorphic: even at the level of base pair positions. *Nucleic Acids Res*. **40**, 3714-22.

26) Lima S, Hildenbrand J, Korostelev A, Hattman S, Li H. (2002) Crystal structure of an RNA helix recognized by a zinc-finger protein: an 18-bp duplex at 1.6 A resolution. *RNA*. **8**, 924-32.

27) Howerton SB, Nagpal A, Williams LD. (2003) Surprising roles of electrostatic interactions in DNA-ligand complexes. *Biopolymers*. **9**, 87-99.

28) Zeman,S., Phillips,D. and Crothers,D. (1998) Characterization of covalent adriamycin-DNA adducts. *Proc. Natl Acad. Sci*., **95**, 11561–11565.

29) Chaires,J., Satyanarayana,S., Suh,D., Fokt,I., Przewloka,T. and Priebe,W. (1996) Parsing the free energy of anthracycline antibiotic binding to DNA. *Biochemistry*, **35**, 2047–2053.

30) Rabbani,A., Finn,R., Thambirajah,A. and Ausio,J. (2004) Binding of antitumor antibiotic daunomycin to histones in chromatin and in solution. *Biochemistry*, **43**, 16497–16504.

31) Chaires,J., Dattagupta,N. and Crothers,D. (1982) Studies on interaction of anthracycline antibiotics and deoxyribonucleic acid: equilibrium binding studies on the interaction of daunomycin with deoxyribonucleic acid. *Biochemistry*, **21**, 3933–3940.

32) Chaires,J. (1990) Biophysical chemistry of the daunomycin-DNA interaction. *Biophys. Chem*., **35**, 191–202

33) Fritzsche,H. and Berg,H. (1987) Analysis of equilibrium, kinetic and structural data of anthracycline-DNA interaction. *Gazz. Chim. Ital*., **117**, 331–352.

34) Priebe,W. (1995) Mechanism of action-governed design of anthracycline antibiotics: a ‘‘turn-off/turn-on’’ approach. *Curr. Pharmaceut. Design*, **1**, 51–68.

35) Graves,D.E. and Krugh,T.R. (1983) Adriamycin and daunorubicin bind in a cooperative manner to deoxyribonucleic acid. *Biochemistry*, **22**, 3941–3947.

36) Pullman,B. (1991) Sequence specificity in the binding of anti-tumour anthracyclines to DNA: a success of theory. *Anticancer Drug Des*., **6**, 95–105.

37) Todd RC, Lippard SJ. (2010) Structure of duplex DNA containing the cisplatin 1,2-{Pt(NH3)2}2+-d(GpG) cross-link at 1.77 A resolution. *J Inorg Biochem*. **104**, 902-8.

38) Weeks KM, Crothers DM. (1993) Major groove accessibility of RNA. *Science*. **261**, 1574-7.

39) Hermann T, Patel DJ. (1999) Stitching together RNA tertiary architectures. Stitching together RNA tertiary architectures. *J Mol Biol*. **294**, 829-49.

40) Varani G, McClain WH. The G x U wobble base pair. (2000) A fundamental building block of RNA structure crucial to RNA function in diverse biological systems. *EMBO Rep* **1**, 18-23.

41) Hermann T, Patel DJ. (2008) RNA bulges as architectural and recognition motifs. Structure. **8**, R47-54.

42) Kim SH, Suddath FL, Quigley GJ, McPherson A, Sussman JL, Wang AH, Seeman NC, Rich A. (1974) Three-dimensional tertiary structure of yeast phenylalanine transfer RNA. *Science*. **185**, 435-40.

43) Kim SH, Sussman JL, Suddath FL, Quigley GJ, McPherson A, Wang AH, Seeman NC, RICH A. (1974) The general structure of transfer RNA molecules. *Proc Natl Acad Sci U S A*. **71**, 4970-4.

44) Byrne RT, Konevega AL, Rodnina MV, Antson AA. (2010) The crystal structure of unmodified tRNAPhe from Escherichia coli. *Nucleic Acids Res*. **38**, 4154-62.

45) Cech TR, Rio DC. (1979) Localization of transcribed regions on extrachromosomal ribosomal RNA genes of Tetrahymena thermophila by R-loop mapping. *Proc Natl Acad Sci U S A*. **76**, 5051-5.

46) Zaug AJ, Cech TR. (1980) In vitro splicing of the ribosomal RNA precursor in nuclei of Tetrahymena. *Cell*. **19**, 331-8.

47) Altman S. (2000) The road to RNase P. *Nat Struct Biol*. **7**, 827-8.

48) "The Nobel Prize in Chemistry 1989". Nobelprize.org. 15 Jul 2012 http://www.nobelprize.org/nobel_prizes/chemistry/laureates/1989/

49) de la Peña M, García-Robles I. (2010) Ubiquitous presence of the hammerhead ribozyme motif along the tree of life. *RNA*. **16**, 1943-50.

50) Przybilski R, Graf S, Lescoute A, Nellen W, Westhof E, Steger G, Hammann C. (2005) Functional hammerhead ribozymes naturally encoded in the genome of Arabidopsis thaliana. *Plant Cell.* **17**, 1877–1885.

51) Nelson JA, Uhlenbeck OC. (2008) Minimal and extended hammerheads utilize a similar dynamic reaction mechanism for catalysis. *RNA*. **14**, 43-54.

52) Hermann T. (2005) Drugs targeting the ribosome. *Curr Opin Struct Biol*. **15**, 355-66.

53) Poehlsgaard J, Douthwaite S. (2005) The bacterial ribosome as a target for antibiotics. *Nat Rev Microbiol*. **3**, 870-81.

54) Hermann T. (2003) Chemical and functional diversity of small molecule ligands for RNA. *Biopolymers*. **70**, 4-18.

55) Schmeing TM, Ramakrishnan V. (2009) What recent ribosome structures have revealed about the mechanism of translation. *Nature* **461**, 1234-42.

56) Wimberly BT, Brodersen DE, Clemons WM Jr, Morgan-Warren RJ, Carter AP, Vonrhein C, Hartsch T, Ramakrishnan V. (2000) Structure of the 30S ribosomal subunit. *Nature*. **407**, 327-39.

57) Ban N, Nissen P, Hansen J, Moore PB, Steitz TA. (2000) The complete atomic structure of the large ribosomal subunit at 2.4 A resolution. *Science*. **289**, 905-20.

58) Nissen P, Hansen J, Ban N, Moore PB, Steitz TA. (2000) The structural basis of ribosome activity in peptide bond synthesis. *Science*. 289, 920-30.

59) Schluenzen F, Tocilj A, Zarivach R, Harms J, Gluehmann M, Janell D, Bashan A, Bartels H, Agmon I, Franceschi F, Yonath A. (2000) Structure of functionally activated small ribosomal subunit at 3.3 angstroms resolution. *Cell*. **102**, 615-23.

60) "The Nobel Prize in Chemistry 2009". Nobelprize.org. 15 Jul 2012 http://www.nobelprize.org/nobel_prizes/chemistry/laureates/2009/

61) First Antibiotic in a New Class of Drugs Fights Resistant Infections. (2000) *FDA Consum.* **34**, 4.

62) Swaney SM, Aoki H, Ganoza MC, Shinabarger DL. (1998) The oxazolidinone linezolid inhibits initiation of protein synthesis in bacteria. *Antimicrob Agents Chemother* **42**, 3251-5.

63) Ippolito JA, Kanyo ZF, Wang D, Franceschi FJ, Moore PB, Steitz TA, Duffy EM. (2008) Crystal structure of the oxazolidinone antibiotic linezolid bound to the 50S ribosomal subunit. *J Med Chem*. **51**, 3353-6.

64) Seidelt B, Innis CA, Wilson DN, Gartmann M, Armache JP, Villa E, Trabuco LG, Becker T, Mielke T, Schulten K, Steitz TA, Beckmann R. (2009) Structural insight into nascent polypeptide chain-mediated translational stalling. *Science* **326**, 1412-5.

65) LOWBURY EJ, HURST L. (1959) The sensitivity of staphylococci and other wound bacteria to erythromycin, oleandomycin, and spiramycin. *J Clin Pathol*. **12**, 163-9.

66) Kovalic D, Giannattasio RB, Weisblum B. (1995) Methylation of minimalist 23S rRNA sequences in vitro by ErmSF (TlrA) N-methyltransferase. Biochemistry. **34**, 15838-44.

67) Prystowsky J, Siddiqui F, Chosay J, Shinabarger DL, Millichap J, Peterson LR, Noskin GA.(20010) Resistance to linezolid: characterization of mutations in rRNA and

comparison of their occurrences in vancomycin-resistant enterococci. *Antimicrob. Agents Chemother.* **45**, 2154–2156.

68) Xiong L, Kloss P, Douthwaite S, Andersen NM, Swaney S, Shinabarger DL, Mankin AS. (2000) Oxazolidinone resistance mutations in 23S rRNA of Escherichia coli reveal the central region of domain V as the primary site of drug action. *J Bacteriol*. **182**, 5325-31.

69) Meka VG, Pillai SK, Sakoulas G, Wennersten C, Venkataraman L, DeGirolami PC, Eliopoulos GM, Moellering RC Jr, Gold HS.(2004) Linezolid resistance in sequential Staphylococcus aureus isolates associated with a T2500A mutation in the 23S rRNA gene and loss of a single copy of rRNA. *J Infect Di*s. **190**, 311-7.

70) Livermore DM, Warner M, Mushtaq S, North S, Woodford N. (2007) In vitro activity of the oxazolidinone RWJ-416457 against linezolid-resistant and -susceptible staphylococci and enterococci. *Antimicrob Agents Chemother*. **51**, 1112-4.

71) Wong A, Reddy SP, Smyth DS, Aguero-Rosenfeld ME, Sakoulas G, Robinson DA. (2010) Polyphyletic emergence of linezolid-resistant staphylococci in the United States. *Antimicrob Agents Chemother*. **54**, 742-8.

72) Tsiodras S, Gold HS, Sakoulas G, Eliopoulos GM, Wennersten C, Venkataraman L, Moellering RC, Ferraro MJ. (2001) Linezolid resistance in a clinical isolate of Staphylococcus aureus. *Lancet*. **358**, 207-8.

73) Jack A. Dunkle, Liqun Xiong, Alexander S. Mankin, and Jamie H. D. Cate. (2010) Structures of the Escherichia coli ribosome with antibiotics bound near the peptidyl transferase center explain spectra of drug action. *Proc Natl Acad Sci U S A*. **107**, 17152–17157.

74) Mark E. Jones, Daniel F. Sahm, Nele Martin, Sibylle Scheuring, Peter Heisig, Clyde Thornsberry, Karl Köhrer, and Franz-Josef Schmitz. (2000) Prevalence of gyrA, gyrB, parC, and parE Mutations in Clinical Isolates of Streptococcus pneumoniae with Decreased Susceptibilities to Different Fluoroquinolones and Originating from Worldwide Surveillance Studies during the 1997-1998 Respiratory Season. *Antimicrob Agents Chemother*. **44**, 462–466.

CHAPTER 2: INTERACTION OF ANTHRACYCLINES WITH IRON RESPONSIVE ELEMENT mRNAs

This work was published by Joshua Canzoneri and Adegboyega Oyelere in Nucleic Acids Research 2008 (38), 6825-6834. The manuscript is presented here unchanged except for section 2.1.

2.1 Introduction

Double-stranded sections of mRNA are often inviting sites of interaction for a wide variety of proteins and small molecules. Interactions at these sites can serve to regulate, or disrupt, the homeostasis of the encoded protein products. Such ligand target sites exist as hairpin–loop structures in the mRNAs of several of the proteins involved in iron homeostasis, including ferritin heavy and light chains, and are known as iron responsive elements (IREs). These IREs serve as the main control mechanism for iron metabolism in the cell via their interaction with the iron regulatory proteins (IRPs). Disruption of the IRE/IRP interaction could greatly affect iron metabolism. Here, we report that anthracyclines, a class of clinically useful chemotherapeutic drugs that includes doxorubicin and daunorubicin, specifically interact with the IREs of ferritin heavy and light chains. We characterized this interaction through UV melting, fluorescence quenching and drug–RNA footprinting. Results from footprinting experiments with wild-type and mutant IREs indicate that anthracyclines preferentially bind within the UG wobble pairs flanking an asymmetrically bulged C-residue, a conserved base that is essential for IRE–IRP interaction. Additionally, drug–RNA affinities (apparent K_ds) in the high nanomolar range were calculated from fluorescence quenching experiments, while UV melting studies revealed shifts in melting temperature (ΔTm) as large as 10°C. This anthracycline–IRE interaction may contribute to the aberration of intracellular iron homeostasis that results from anthracycline exposure.

2.2 Anthracycline Antibiotics

Daunorubicin (DAU), the first member of the anthracycline antibiotic family, was isolated from the *Streptomyces peucetius* soil bacterium in 1963. Soon after, the incredibly potent antineoplastic ability of DAU and its analogs, including its 14-hydroxylated variant doxorubicin (DOX), was noted in cancerous cell cultures (1). The antineoplastic nature of the compounds was at the time attributed to their ability to inhibit nucleic acid metabolism. It was observed that anthracyclines not only bound to nucleic acids but they also greatly inhibited the synthesis of both DNA and RNA (2, 3). The anthracycline class of drugs quickly entered clinical trials in the mid to late 1960's, they were subsequently granted FDA approval, and they remain the cornerstone of clinical treatment of leukemia, lymphoma, solid tumors and Hodgkin's disease (4). However, the clinical use of anthracyclines is limited by the occurrence of both chronic and acute cardiotoxicity that can often lead to cardiomyopathy, myocardial infarction and congestive heart failure (4-6). The mitigation of these often fatal side affects is of high interest and many attempts have been made to characterize the mechanism of anthracycline cardiotoxicity. However, there is much disagreement on this point in the literature. Theories include the suppression of transcription factors, production of reactive oxygen species, free radical-induced oxidative stress, decreased levels of intercardiac protective proteins and impaired intracellular iron handling and homeostasis (7-15). Elegant attempts have been made to tie all of the popular pathways listed above into a single complex model for anthracycline cardiotoxicity (16). However, the exact method by which anthracyclines lead to cardiomyopathy must still be

elucidated in order to rationally design new therapeutic options for the successful treatment of cancer with anthracyclines.

2.3 Iron Metabolism and Regulation via Iron Responsive Elements

The iron responsive elements (IREs) of proteins involved in iron metabolism serve as the premier regulatory site of translation due to their unique tertiary structure. IREs are ≈30-nt long hairpin–loop structures in the untranslated regions (UTRs) of several iron metabolism proteins including both ferritin subunits (Figure 2.1), ferroportin and the erythroid isoform of aminolevulinate synthase, eALAS (17,18) The structure and sequence of IREs is highly conserved throughout all of the animal kingdom including early metazoan (19). The homeostasis of IRE-containing mRNAs is regulated by the iron-dependent availability of the IRP proteins (17). Ligand interaction in the UTRs of mRNA can serve to stabilize or destabilize the mRNA, and thus increase or decrease translation. In general, binding of a protein or small molecule in the 5`-UTR inhibits translation by deterring the association of translation factors and preventing the assembly of the ribosome. Conversely, the binding of a ligand in the 3`-UTR upregulates translation by protecting against nuclease degradation (17). In the case of IRE–IRP interaction, at low intracellular iron concentrations, IRP1 is converted into its active binding state through the dissociation of its 4Fe-4S cluster. This active state then binds to the 5` IRE of ferritin heavy and light chain mRNAs, serving to downregulate translation and reduce the iron-storage capacity of ferritin (17). Disruption of this IRE/IRP interaction could greatly affect intracellular iron handling.

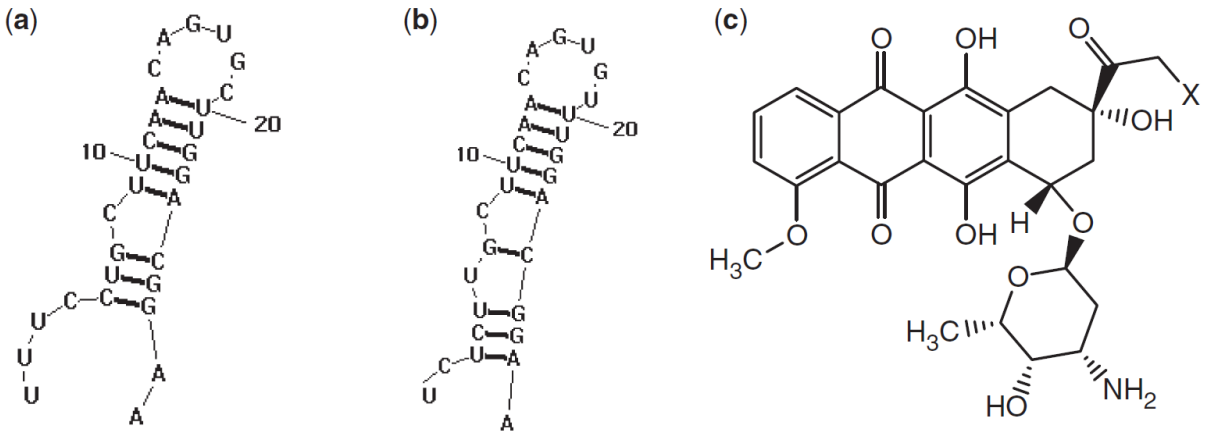

Figure 2.1 (a) Human ferritin H-chain IRE 5_ UTR, (b) human ferritin L-chain IRE 5_ UTR, (c) anthracyclines investigated in this report, X=OH, doxorubicin; X=H, daunomycin.

The antitumor affects of anthracyclines are attributed to the ability of the molecules to inhibit topoisomerase by intercalating DNA, and the specifics of this interaction are very well-characterized (20-28). However, the ability of these drugs to intercalate double-stranded RNA has largely been neglected in the literature. It has previously been observed that anthracyclines cause an imbalance in the regulation of IRP and its binding to IREs, but it has yet to be investigated whether this perturbation is a direct result of anthracyclines interacting with the IREs (11, 12). Toward unraveling the mechanism of anthracycline induced disruption of IRE binding to IRP we investigated the possibility of a direct interaction between anthracyclines and IREs harbored at the 5`-UTR of ferritin heavy and light chain mRNAs. A direct interaction of a small molecule, such as an anthracycline, with the IRE could change the tertiary structure of the RNA drastically and alter the effectiveness of the IRE/IRP interaction.

2.4) Biophysical Characterization of Anthracycline/ IRE RNA Interaction

mRNA sequence selection and preparation

The mRNA sequences of the human proteins of interest were retrieved from the Entrez Nucleotide Database (www.pubmed.org). The UTRs of these mRNA sequences were identified, and the folding of these sequences was modeled in the RNAstructure Version 4.3 program (rna.urmc.rochester.edu/rnastructure.html). The resulting secondary structures were surveyed to identify hairpin loop structures. The isolated sequence of the loop and stem region of these structures, on average 30 nt in length, was then folded via the RNAstructure program once again to ensure that the secondary structure was maintained in the absence of the rest of the sequence (Figure 2.1). The mRNA sequences of these structures were purchased from Dharmacon Research Inc., Lafayette, CO, deprotected according to the manufacturer's protocol, and their purity was verified via denaturing urea polyacrylamide gel electrophoresis. RNA concentrations were determined by UV-vis spectroscopy in 1 cm path length quartz cuvettes using the molar extinction coefficients provided by Dharmacon.

UV-vis melting and absorption experiments

UV melting experiments were performed in the absence of drug and in the presence of DOX or DAU at final drug concentrations of 5 μM and 20 μM. RNA and drug complexes were formed by the addition of an aliquot of stock drug solution in DMSO to a volume of RNA in BPE buffer (6mM Na2HPO4, 2mM Na2H2PO4, 1mM EDTA, pH 7.1). The mixture was allowed to equilibrate for at least 20 min at 4°C to ensure complete association. The drug stock was prepared so that upon reaching the desired concentration of drug, the amount of DMSO in the sample was no >1% of the total volume. For absorption studies, a constant concentration of drug (7 μM) was titrated with increasing amounts of RNA (0.5–20 μM) and the absorbance was

measured over the range of 400–600nm on a Cary 50 Bio UV-vis spectrophotometer. Melting studies were performed over a temperature range of 25–90°C, using a melting rate of 1°C/min and data were collected every half degree. In order to favor hairpin formation and avoid self-association, constructs were heated at 99°C for 1 min, then slowly cooled (1°C/min) to 10°C prior to being melted from 25°C to 90°C (29). For melting experiments, absorbance was measured at 260 nm, the temperature was controlled with a Quantum Northwest TC 125 temperature control unit, drug concentration varied between 5 and 20 μM, and the concentration of RNA was held constant at 2.5 μM. The T_m was taken as the midpoint of the melting transition as determined by the maxima of first derivative plots. An example of the first derivative plots for ferritin H-chain IRE RNA in the absence and presence of both DOX and DAU can be found in the Supplementary Material (Supplementary Figure S1). All T_ms were reproducible to within ±1°C. Repeated recording of heating and cooling profiles indicates that no hysteresis occurs in the absence or presence of ligand.

Fluorescence quenching experiments

Quenching of the drug's natural fluorescence upon binding to RNA was monitored via titrations of a constant concentration of drug (7 μM) with RNA of increasing concentration (0.1–20 μM). Quenching experiments were performed in a 96-well black microplate following the protocol described by Hergenrother et al. (30). Fluorescence emission at 556nm was recorded on a Molecular Devices SpectraMAX Gemini microplate reader after excitation at 480nm and 485nm for DOX and DAU respectively. All experiments were repeated at least four times. The data collected in the fluorescence quenching titrations was fit to a second-order decay curve utilizing TableCurve 2D v5.01, equation 8107 (30):

$$y = \frac{a * b}{b + x}$$

Where b is the apparent dissociation constant, x is the RNA concentration and a is the asymptotic limit. Fluorescence quenching plots and curve fits are available in the Supplementary Material. A stock solution of 4M NaCl in BPE buffer was diluted with BPE to achieve the various salt concentrations listed in the paper (31).

RNase T1 footprinting

The protocol for drug–RNA footprinting was adapted from previously reported methods (32). RNA constructs were 5`-end-labeled with γ-^{32}P ATP (PerkinElmer, Waltham, MA) utilizing T4 polynucleotide kinase (Invitrogen, Carlsbad, CA) according to the manufacturer's protocol. Labeled RNA (1.25 µM), unlabeled RNA (11.5 µM) and drug (1–20 µM) were combined in a final volume of 9 µl of footprinting buffer (11mM Tris–HCl, pH 7.0) and were allowed to equilibrate for 30 min at 25°C. The equivalent of 1U of RNase T1 enzyme (USB) was added and allowed to proceed for 10 min at 25°C. The reaction was quenched by the addition of 5 µl of urea loading buffer (8M urea, 20mM EDTA and 2mM Tris, pH 7.5). Samples were then heated at 95°C for 5 min, and 11 µl of each sample was run on a 12% denaturing acrylamide gel for 90 min at 290 V. The gel was then dried, exposed to an IP plate (Fuji Film) and was visualized on a Fuji Film FLA-3000 IP plate scanner. Quantification of band intensity was performed with the Fuji Film program Multi Gauge version 3.0 utilizing profile quantification in the direction of migration and a polygonal baseline for background compensation.

RESULTS

UV melting and absorbance experiments

The magnitude of ligand-induced change in nucleic acid T_m [$\Delta T_m = T_m$ (RNA + ligand) - T_m(RNA)] is an indication of the affinity of the ligand for the nucleic acid target. Hence, we performed UV melting experiments to obtain the first indication of a direct association between the drugs and the IRE RNAs. The UV melting curves of both ferritin H-chain and L-chain IREs (Figure 2.2) display bi-phasic melting profiles in the absence and presence of drug.

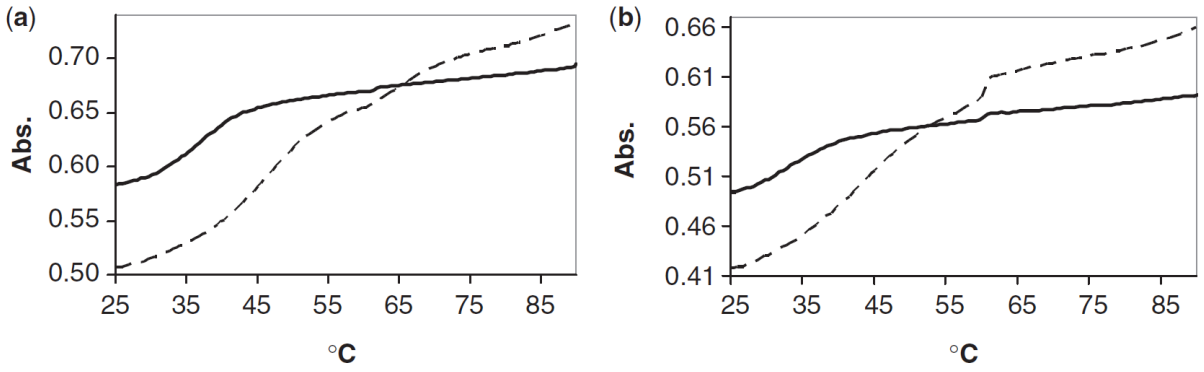

Figure 2.2 Overlay of the melting profiles of (a) ferritin H-chain mRNA and (b) ferritin L-chain mRNA in the absence (solid) and presence (dashed) of 20 μM DOX.

The higher temperature transition (T_m=61°C) is a minor transition and was found to remain constant under all conditions. The lower temperature transition revealed a concentration-dependent increase in T_m in the presence of DOX and DAU. The observed ΔT_m for all construct and drug combinations are presented in Table 2.1. It was found that the addition of drug to the IRE RNAs caused an increase in T_m not only in a concentration-dependent manner but also in a drug-dependent manner, with DOX consistently causing a more substantial shift than DAU (Table 2.1, Supplementary Figure S1). It was also observed that the slight changes in sequence

and structure of the constructs led to a graded degree of T_m shift in response to the presence of drug. In the presence of 20 µM DOX, both the ferritin heavy and light IREs produced a ΔT_m of around 10°C (Table 2.1). Comparatively, the HIV-1 TAR RNA construct (33, 34), which is also a hairpin-loop structure that has been shown to interact with small molecules, produced a maximum shift of 5°C under the same conditions (data not shown).

Table 2.1 The average ΔT_ms observed for all drug and IRE combinations

Ligand	H-chain	L-chain	G23I-IRE	U10C-IRE	U6C-IRE	C8A-IRE	U6C-U10C-IRE
5 µM DOX	2.5	2.7	4.7	3.7	2.6	3.9	1.0
20 µM DOX	9.9	10.1	10.3	6.8	6.5	7.9	5.5
5 µM DAU	0.5	3.5	3.8	1.7	1.5	2.9	0.5
20 µM DAU	5.7	6.5	7.3	4.7	4.0	5.9	1.5

Guided by the results from the RNase footprinting experiments on wild-type IREs (see details below), mutations were made to the native H-chain IRE that altered or removed certain structural features associated with drug binding and recognition (35, 36). We constructed four point mutants designated U6C-IRE, C8A-IRE, U10C-IRE and G23I-IRE (I=inosine) with mutations at nucleotide positions 6, 8, 10 and 23, respectively; and one double mutant designated U6C-U10C-IRE, bearing double mutations that replaced the two UG pairs with CG pairs. These mutations were predicted by RNAstructure to preserve the IRE secondary structure. The difference in ΔT_m between these mutants and the wild-type indicated the importance of both UG wobble base pairs found in the ferritin IRE. The observed ΔT_m for the double mutant, U6C-U10C-IRE, which replaces both UG wobble base pairs, was 5.5°C and 1.5°C in the presence of 20 µM DOX and DAU, respectively. For the G23I-IRE mutant, the magnitudes of the observed ΔT_m are slightly higher than that of the wildtype for both DOX and DAU at all concentration studied (see Supplementary Material for melting curves). Interestingly, U6C-IRE and U10C-

IRE, mutants in which one of the UG pairs is replaced with a CG, have identical ligand-dependent ΔT_m. However, their observed ΔT_m is about 3°C less than that observed with the wild-type RNA in the presence of 20 μM DOX.

Figure 2.3a shows the changes that occur in the absorption spectrum of DOX in the visible region during the titration of a fixed concentration of DOX with increasing concentrations of the wild-type H-chain IRE. The resulting absorbance profile of DOX yielded two distinct absorbance maxima at ≈ 472nm and 499nm and a marked bathochromic shift was observed for both peaks resulting in a $\Delta\lambda$ of 5nm and 10 nm, respectively. Additionally, a hypochromism of 33.7% for the first maxima and 24.4% for the second was observed.

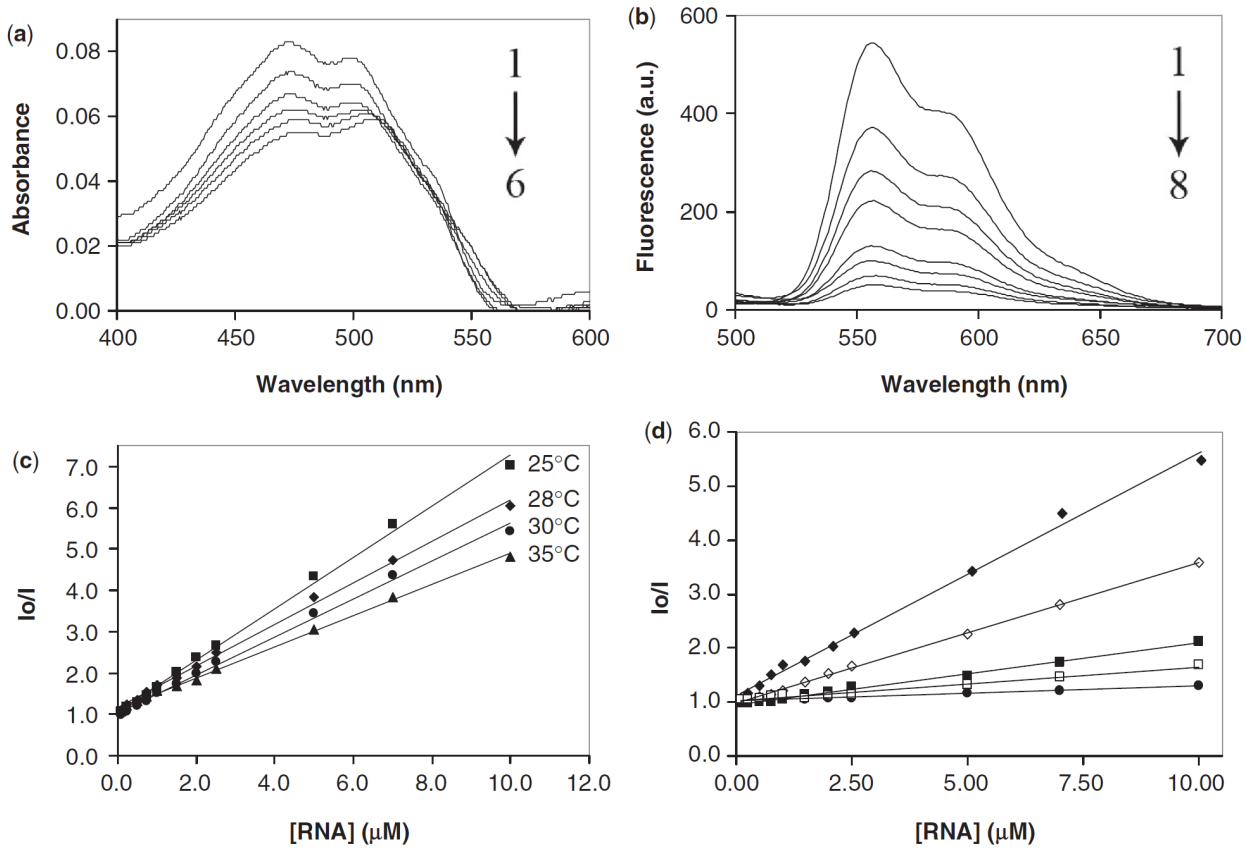

Figure 2.3 (a) Absorbance profiles of 7 μM DOX in the presence of (from 1 to 6) 0, 0.5, 1.0, 2.5, 7 and 20 μM ferritin H-chain IRE RNA. (b) Fluorescence profiles of the titration of 7 μM DOX with (from 1 to 8) 0, 1, 1.5, 2.5, 5, 7, 10 and 15 μM ferritin H-chain IRE RNA. (c) Stern–Volmer plot of 7 μM DOX with ferritin H-chain IRE RNA at the indicated temperatures. (d) Stern–Volmer plot of 7 μM DOX with ferritin H-chain IRE RNA in BPE of the following Na^+ concentrations: 16mM (filled diamond), 46mM (open diamond), 116mM (filled square), 216mM (open square) and 516mM (filled circle). Each Stern–Volmer plot was obtained from an average of at least four independent experiments.

Fluorescence quenching

The natural fluorescence of DOX and DAU upon excitation was monitored as they were titrated with increasing amounts of RNA. The fluorescence spectra show a quenching of DOX fluorescence signal upon titration with IRE RNA (Figure 2.3b). The decay curves of the fluorescent signal were fitted, and apparent K_ds were calculated. It is important to note that this apparent K_d is a total dissociation constant, and does not differentiate between the contribution of direct drug binding (e.g. intercalation) and the contribution of electrostatic interaction due to the charged nature of the anthracycline molecule. The apparent K_ds and associated standard errors of RNA constructs are presented in Table 2.2. Fluorescence quenching data at 25, 28, 30 and 35°C was used to perform a Stern–Volmer analysis (31, 37, 38) of ferritin H-chain IRE RNA quenching DOX according to the equation:

$$I_0/I = 1 + K_{SV}\,[Q]$$

Where I_0 and I are the fluorescence intensities in the absence and presence of RNA, respectively, [Q] is the concentration of quencher (RNA) and K_{SV} is the dynamic quenching constant related to the bimolecular collision process. For the quenching experiment at 25°C, this analysis revealed a linear relationship between I_0/I and [Q] (Figure 2.3c). The linearity of the Stern–Volmer plot indicates that the mode of quenching is either collisional or static. Collisional and static quenching can be distinguished by their different dependencies on temperature. An increase in temperature leads to an increase in the diffusion constant of the quencher and will result in an increase in collisional quenching. In contrast, an increase in temperature will lead to a decrease in the binding constant of quencher for fluorophore and will result in a decrease in

quenching for a static quencher (38). To identify the quenching mechanism, we repeated the quenching experiments at 25, 28, 30 and 35°C. Stern–Volmer analysis of the resulting data revealed linear relationships between I_0/I and [Q] and also showed that the K_{SV} is inversely correlated with temperature (Figure 2.3c). Based on this result, it could be concluded that the probable quenching mechanism of the DOX-H-chain IRE–RNA complex is initiated by static quenching (37, 38).

Table 2.2 Apparent K_ds and standard errors of association of DOX with wild-type and mutant IREs.

	H-chain	L-chain	G23I-IRE	U10C-IRE	U6C-U10C-IRE
Apparent K_d (nM)	904	837	903	991	1100
Fit Std Error (nM)	±30.9	±32.7	±22.0	±13.2	±38.5

To determine the drug/RNA stoichiometry, we use the fluorescence quenching data to construct Job plots (Figure 2.4) (39, 40). The x-axis of the Job plot, labeled as the mole fraction, is the ratio of the concentration of RNA to the total concentration of RNA and drug, or: Mole Fraction = [RNA] / ([RNA] + [drug]). In this case, the sum of [RNA] and [drug] was held constant at 7 μM. The intersection of the two linear portions of the Job plot yield the mole ratio corresponding to the approximate binding stoichiometry between drug and RNA. This analysis revealed a mole fraction corresponding to ≈ 3.0 molecules of drug associating with each molecule of the H-chain IRE RNA. To further confirm the participation of the UG pairs in anthracycline binding, we also constructed Job plots using the fluorescence quenching data of the mutants IREs. We obtained a binding stoichiometry of ≈ 2.0 molecules of drug associating with each molecule of either U10C or the double mutant U6C, U10C (See Supplementary Figure S3).

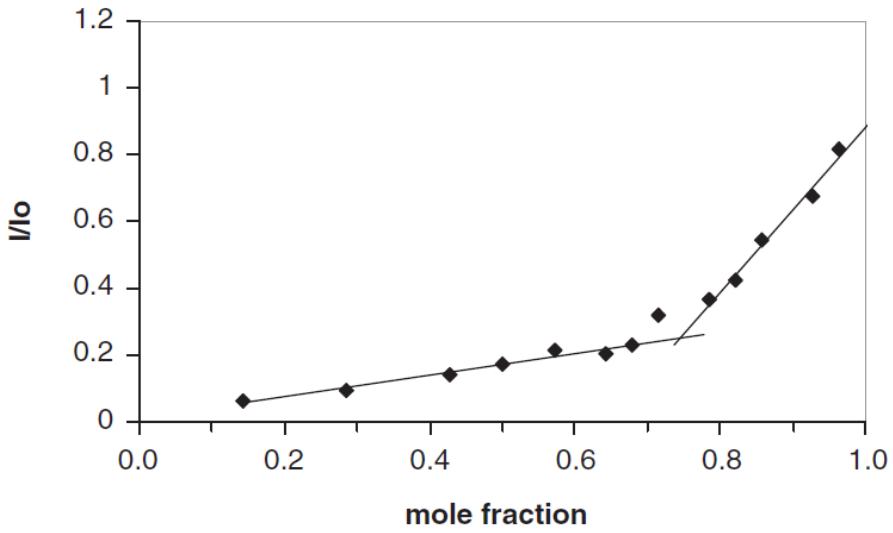

Figure 2.4. Job plot of the fluorescence decay of DOX being titrated with ferritin H-chain IRE RNA. The sum of [RNA] and [drug] was held constant at 7 μM in each experiment {Mole Fraction = {([RNA] + [drug]) / [RNA]}. Each point was obtained from an average of at least four independent experiments. The error associated with this experiment is estimated to be 10%.

Binding energy

In an effort to partition the binding free energies of anthracyclines with the IRE RNAs into their nonelectrostatic and polyelectrolyte contributions, fluorescence quenching was monitored over a range of Na^+ concentrations, and a Stern–Volmer plot for each was plotted (Figure 2.3d) (21). The quenching constant (K_{SV}) was determined for each curve and was then used to calculate the standard Gibbs free energy ($\Delta G°$) using the equation:

$$\Delta G° = - RT \ln K_{SV}$$

Where R is the gas constant (1.987 cal/K/mol) and T is the temperature in Kelvin. The quenching constants estimated at 25, 28, 30 and 35°C are 6.2 x 10^5 M^{-1}, 5.0 x 10^5 M^{-1}, 4.6 x 10^5 M^{-1} and 3.8 x 10^5 M^{-1}, respectively. A subsequent plot of log K_{SV} versus log [Na^+] yielded the salt dependence of the binding constant defined by the slope (SK) of such plots. The SK value (-0.83

for DOX and ferritin H-chain IRE) was used in the following equation to determine the polyelectrolyte contribution (ΔG_{PE}) at a given salt concentration (21, 41):

$$\Delta G_{PE} = (SK)\ RT \ln [Na^+]$$

To determine the nonelectrostatic contribution to binding energy, the nonelectrostatic contribution to the free energy change (ΔG_t) was calculated according to the equation (25):

$$\Delta G_t = \Delta G^\circ - \Delta G_{PE}$$

The values obtained for the binding of DOX to H-chain IRE RNA (BPE buffer, 16mM Na^+, 25°C) are as follows: ΔG°= - 7.7 kcal mol^{-1}, ΔG_{PE} = - 2.0 kcal mol-1 and ΔGt = - 5.7 kcal mol^{-1}. The error associated with these values is estimated to be ± 0.1 kcal mol^{-1} (21). A comparable value of ΔG_{PE} has been reported for the binding of DOX to DNA under similar conditions (21).

Drug–RNA footprinting

RNase footprinting was performed in order to probe the binding site(s) of DOX and DAU on the RNA constructs. Of the several RNases investigated, RNase T1 was found to provide the cleanest and most useful cleavage pattern. RNase T1 cleaves single-stranded RNA at the 3`-end of guanylic residues and, as expected, it caused strong cleavage of the RNA at G7, G16 and G18, all residues predicted by RNAstructure to be within the single-stranded region of the IRE secondary structure (Figure 2.5a). The most striking observation from this autoradiograph is that T1 cleavage at G22/G23 and G26/27, the nucleotide positions corresponding to the two UG sites, displayed a drug concentration-dependent increase in band intensity (Figure 2.5a). While G16 also showed some variation in band intensity, comparison of the quantitated G16 and G23 band intensities, after the footprinting of the H-chain IRE with DOX, revealed that G23 displayed a

consistent and marked concentration-dependent increase in cleavage intensity compared to G16 (Figure 2.5b).

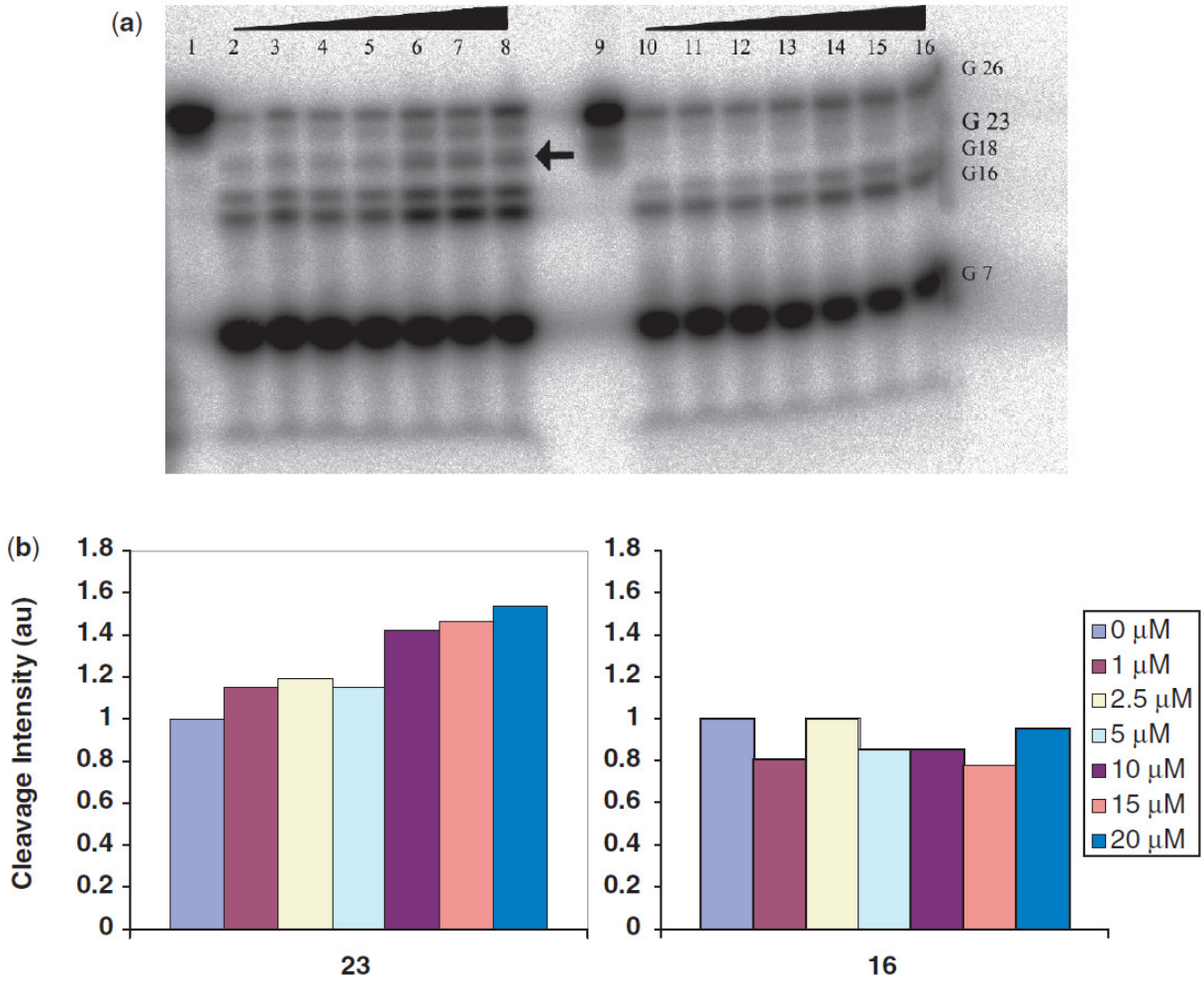

Figure 2.5 (a) Autoradiograph of RNase T1 footprinting of γ-^{32}P 5`-end-labeled ferritin H-chain IRE RNA (lanes 1–8) and H-chain U10C mutant(lanes 9–16). Lane: (1) H-chain RNA only; (2–8) RNA, RNase T1 and 0, 1, 2.5, 5, 10, 15, 20 µM DOX, (9) H-chain U10C mutant RNA only; (10–16) RNA, RNaseT1 and 0, 1, 2.5, 5, 10, 15, 20 µM DOX. The G 23 band, indicated by the arrow, is absent for the mutant. (b) Quantitations of theG16 and G23 bands intensities of ferritin H-chain IRE RNA after RNase T1 footprinting in the presence of DOX. DOX concentration for each band is indicated in the legend.

We then used RNase T1 footprinting to follow the effects of the aforementioned mutations on cleavage at G23, the guanylic residue of one of the UG pairs (U10G23) that showed T1 cleavage enhancement in the presence of DOX. We chose to monitor G23 because it is the better resolved of the two G residues on the autoradiograph (Figure 2.5a). In a manner similar to the wildtype H-chain IRE, the footprinting of the G23I mutant with DOX displayed a drug concentration dependent increase in band intensity at G23 (data not shown). Conversely, the footprint of the U10C-IRE, the mutant which replaced the top UG pair, lacks the band corresponding to G23 when compared to that of the wildtype H-chain IRE (Figure 2.5a). Validation of the cleavage band designations can be found in the supplementary material (Supplementary Figure S4).

2.5) Discussion

Anthracycline–DNA interactions are among the best characterized in the literature (20-28). Despite their chemical similarity to DNA and direct role in gene expression, little is known about the extent to which RNA interactions with anthracyclines contribute to anthracyclines' biological activities. In this article, we demonstrate that DOX and DAU directly interact with the IRE hairpins (Figure 2.1a and b) located in the 5`-UTR of ferritin H- and L-chains mRNAs. DOX and DAU caused a concentration-dependent shift in the melting profiles of the H- and L-chains IREs (Figure 2.2 and Supplementary Figure S1). In most cases, we observed higher ΔT_ms for DOX compared to DAU for all IRE RNAs studied under the same conditions (Table 2.1). Since the magnitude of ΔT_m is an indication of the affinity of a probe molecule for a nucleic acid target (42), the noted differences in the values of ΔT_ms suggest that DOX binds tighter to these RNAs compared to DAU. The lower ΔT_ms observed for DAU (Table 2.1, bottom half) is consistent with the literature report indicating that DAU binds to DNA between 1.5- to 4-fold less strongly than DOX (27). Furthermore, the only structural difference between the two drugs is the presence of a primary OH-group at C14 of DOX (Figure 2.1c); it is therefore possible that the OH-group at C14 is playing a role in the binding of anthracyclines to the RNAs, perhaps in a similar manner to its involvement in DNA binding and recognition (43).

The drug induced changes in the melting profiles of the mutant IREs gave further evidence for the base sequence preference of the interactions between the anthracyclines and the IRE RNAs. While the asymmetric bulge in the H-chain IRE is somewhat tolerant of a base change, the replacement of either or both of the UG wobble pairs flanking the asymmetric bulge with a CG significantly impaired DOX and DAU binding (Table 2.1). These results point to the requirement of the UG base pairs in facilitating the binding of DOX and DAU to the IRE RNAs.

However, the UG base pair recognition by anthracyclines may be RNA sequence dependent. Preliminary evidence to that effect was seen in the melting profile of a C22U mutant TAR RNA. Relative to the wild-type TAR RNA, we observed almost no change in ΔT_m of the C22U mutant in the presence of 20 μM DOX. This result may suggest that the microenvironment of the UG pairs within the RNA sequence may play important role in anthracycline recognition (see Supplementary Figure S2, for the melting profiles of wild-type and C22U mutant TAR RNA).

The ability of IRE RNAs to alter the spectral characteristics of anthracyclines gives further indication of an interaction of drug and RNA (Figure 2.3 a and b). We observed a quenching of the natural fluorescence of DOX and DAU with increasing RNA concentration (Figure 2.3b). The quenching of DOX fluorescence by DNA has been ascribed to its intercalation into DNA (23, 44). Thus, we attribute the extensive fluorescence quenching (>90% at a 2:1 ratio of DOX to H-chain IRE RNA) to the intercalation of one or more anthracycline molecules per RNA molecule (Figure 2.3b). A similar interpretation has recently been proposed to explain DOX fluorescence quenching by a SELEX generated DOX RNA aptamer (45). Additionally, the titration of a fixed concentration of DOX with increasing concentrations of the wild-type H-chain IRE results in a hyprochromic effect accompanied by a shift of the absorption maximum (λ_{max}) to a longer wavelength (bathochromic shift). The observed maximal absorbance decrease is ≈ 33.7% (Figure 2.3a). These results are indicative of changes in the drug's environment and a perturbation of the DOX chromophore system upon binding to the IRE RNA, consistent with intercalative binding of DOX within the IRE RNA. Furthermore, the apparent K_d (Table 2.2) extracted from the fluorescence quenching data give an indirect clue about the affinity of DOX for the IREs. Although we did not have sufficient information to differentiate between the

contribution of direct drug binding and that of electrostatic interaction for all IRE constructs, the magnitudes of the apparent K_d's suggest strong association of the drug with the IREs.

We performed RNase footprinting experiments to gain more insight into the binding site(s) of DOX and DAU on the ferritin H-chain IRE and a series of mutant RNAs (46, 47). Results from the drug–RNA footprinting experiments show that the T1 cleavage at two sites, G22/G23 and G26/27, is enhanced upon addition of DOX (Figure 2.5a). Chaires et al. (47) have attributed an analogous enhancement in nuclease cleavage of DNA, in the presence of DAU, to the perturbation of DNA structure in the immediate vicinity of a DAU intercalation site. If this explanation holds for RNA, our results suggest the existence of at least two main drug binding sites at or near the two UG wobble base pairs of the ferritin H-chain IRE (Figure 2.5). Interaction of anthracycline molecules at both of these proposed binding sites would not violate the nearest neighbor exclusion rule when applied to anthracycline–nucleic acid binding (23).

Wobble pairs, especially GU or UG, are ubiquitous building blocks of higher order RNA structures. Compared to regular Watson–Crick base pairs, wobble pairs differ in both the array of functional groups displayed in the helical grooves and the orientation of the bases with respect to the phosphodiester backbone. The consequence of this is that a wobble pair causes weakening of the helix and local distortions which significantly increase the electronegative environment at or near the mismatch pair (48, 49). The two UG pairs in the ferritin H-chain IRE could each provide an electronegative environment for nestling the electropositive DOX. In fact, the wobble pair has been shown to be a commonly conserved ligand binding site (48). To further probe this observation, we extensively studied the effects of mutation of the two UG pairs and bulge C on the binding affinity of DOX for the IRE RNA. Results from these experiments show that all mutations that preserved the U10-G23 wobble displayed essentially the same cleavage pattern as

in the wild-type RNA. This suggests that these mutants are able to induce the structural changes necessary for DOX binding within the vicinity of U10-G23. More importantly, however, the G23I mutant sheds light on the specifics of the UG pair recognition by DOX. The G23I mutation results in the deletion of the guanosine N2 exocyclic amine, a very distinct functional group displayed in the minor groove of a wobble that often serves as a specific receptor recognition signal. The fact that the G23I-IRE mutant also displayed increase in T_m and enhancement of T1 cleavage at G23 in the presence of DOX suggest the G23 amine may not be essential for DOX recognition by the ferritin H-chain IRE (see Supplementary Material for the UV melting profiles for construct G23I, Supplementary Figure S5). An alternative mechanism of ligand recognition of a wobble pair is through its unique conformational features. This may well be exploited by DOX in its interaction with the H-chain IRE. This inference is supported by two key observations. First, the magnitudes of the observed ΔT_ms for the G23I-IRE mutant are slightly higher than that of the wild-type in the presence of either DOX or DAU at all concentration studied (Table 2.1). These data suggest that the substitution of G23 for I may have resulted in slightly increased RNA ligand-binding affinity. Previous literature observation indicates that an IU base pair is slightly less stable than a GU pair (49). The subtle duplex instability as a result of the G23I mutation may enhance the structural changes essential for ligand binding, thereby resulting in increased interaction of ligand with the RNA. Second, the G23 band in the U10C, a mutant IRE in which the G23-U10 is substituted by a GC base pair, is protected from T1 cleavage (Figure 2.5). Based on the increased GC content, one will expect this mutation to increase the binding affinity of DOX for the 5-base paired segment of the IRE. The protection of G23 from T1 digestion may be due to diminished or lack of DOX binding, thereby preventing the necessary conformational changes that expose G23 to T1. Alternatively, it may also be that

DOX binding persists but is not accompanied by a conformational change that is sensitive to T1 cleavage.

The Stern–Volmer analysis of the drug fluorescence quenching data supports a static mechanism for the quenching of the DOX fluorescence by the H-chain IRE RNA (Figure 2.3c and d). The static quenching could occur through the formation of a complex, stabilized mainly by hydrophobic interactions, between DOX (fluorophore) and RNA (quencher) (37, 38). This complex could result from the intercalation of DOX into the IRE bases as suggested by the aforementioned evidence. In addition, the Stern–Volmer analysis allows an estimation of the equilibrium constant for the formation of the DOX-H-chain IRE RNA complex. Applying the polyelectrolyte theory (21, 41), these equilibrium constants enable the dissection of the RNA binding free energies of anthracyclines into their nonelectrostatic and polyelectrolyte contributions. The calculated value of ΔG_{PE} is very similar to that reported for the binding of DOX to DNA under similar conditions (21). This result suggests a similar polyelectrolyte contribution to the overall *ΔG* of binding of DOX to DNA and RNA. A Job plot of the fluorescence quenching of DOX with wildtype IRE RNA gives a drug to RNA binding ratio of ≈ 3.0:1 (Figure 2.4). A similar plot of the U10C IRE, a mutant in which one of the proposed binding sites has been replaced with a GC pair, resulted in a drug to RNA stoichiometry of ≈ 2.0:1 (Supplementary Figure S3). This result is consistent with our original inference on the participation of U10-G23 wobble pair in DOX binding to the IRE. However, the drug to RNA stoichiometry remained ≈ 2.0:1 when both UG pairs are replaced (Supplementary Figure S3). The lack of further change in the drug to RNA ratio upon the replacement of the proposed second DOX binding site may be due to the fact that the second mutation did not completely abolish DOX binding. Although footprinting only identified the two UG sites as possible binding

sites, the nonelectrostatic binding energy, ΔG_t, was found to account for only 74% of the total observed change in ΔG upon DOX binding to IRE RNA. Taken together, these data suggest that in addition to the intercalation of two anthracycline molecules at the UG sites, there is at least one additional site of interaction, most likely electrostatic in nature, on the IRE RNA.

The crystal structure of IRP1 bound to frog ferritin IRE has recently been solved (50). The structure reveals almost twice the number of specific interactions found in most protein–RNA associations. Despite the level of interaction, single mutations to just a few of the residues involved have been shown to greatly diminish the IRE/IRP interaction (35, 51, 52). This high degree of structural and sequence selectivity reveals the seemingly robust interaction to be in fact very sensitive to minute disturbances. The binding of anthracycline molecules to the IRE structure could cause changes to the tertiary structure of the IRE RNA that could diminish the affinity of IRP for the IRE. This may cause an aberration in the intracellular regulation of the translation of mRNAs harboring these IREs. Supporting this hypothesis is a recent observation from the Thorp group on up-regulation of the cellular expression of ferritin upon exposure to yohimbine, a small molecule that binds to the ferritin IRE (53). Additionally, Butcher et al have recently described the binding of anthracyclines to an HIV-1 frameshift site RNA hairpin similar not only in structure to the IREs discussed here, but also in the K_d and ΔT_m values reported for the interaction (54).

The biochemical evidence presented in this study suggests that anthracyclines form strong and specific interactions with IRE RNAs. Furthermore, it sheds light on some of the structural requirements for this interaction. Although anthracyclines such as DOX and DAU have been reported to show a requirement for GC sequences in DNA binding (47,55), we have presented evidence that the binding of anthracyclines to ferritin IRE RNA demonstrates a strong

preference for UG pairs. The prevalence of wobble base pairs in higher order RNA structures (48) suggests that this non-canonical pair, when structurally available, could serve as a ubiquitous recognition site for the binding of anthracyclines to other RNAs as well. Further studies are necessary to better understand the possible biological significance of the anthracycline-IRE interaction. Part of our ongoing effort is to probe the effects of DOX and DAU on IRE-IRP complex formation both in vitro and in vivo.

Supporting Information: Supporting information is available for this chapter in Appendix A.

2.6) References

1) Weiss RB. (1992) The anthracyclines: will we ever find a better doxorubicin? *Semin Oncol*. **19**, 670-86.

2) Di Marco A, Silvestrini R, Di Marco S, Dasdia T. (1965) Inhibiting effect of the new cytotoxic antibiotic daunomycin on nucleic acids and mitotic activity of HeLa cells. *J Cell Biol*. **27**, 545-50.

3) Gabbay EJ, Grier D, Fingerle RE, Reimer R, Levy R, Pearce SW, Wilson WD. (1976) Interaction specificity of the anthracyclines with deoxyribonucleic acid. Biochemistry. **15**, 2062-70.

4) Singal,P. and Iliskovic,N. (1998) Doxorubicin-induced cardiomyopathy *N. Engl. J. Med*., **339**, 900–905.

5) Thorburn,A. and Frankel,A. (2006) Apoptosis and anthracycline cardiotoxicity. *Mol. Cancer Ther*., **5**, 197–199.

6) Jones,R., Swanton,C. and Ewer,M. (2006) Anthracycline cardiotoxocity. *Expert Opin. Drug Saf.*, **5**, 791–809.

7) Kim,Y., Ma,A., Kitta,K., Fitch,S., Ikeda,T., Ihara,Y., Simon,A., Evans,T. and Suzuki,Y. (2003) Anthracycline-induced suppression of GATA-4 transcription factor: implication in the regulation of cardiac myocyte apoptosis. *Mol. Pharmacol*., **63**, 368–377.

8) Fogli,S., Nieri,P. and Breschi,M. (2004) The role of nitric oxide in anthracycline toxicity and prospects for pharmacologic prevention of cardiac damage. *FASEB J*., **18**, 664–675.

9) Jeyaseelan,R., Poizat,C., Baker,R., Abdishoo,S., Isterabadi,L., Lyons,G. and Kedes,L. (1997) A novel cardiac-restricted target for doxorubicin. CARP, a nuclear modulator of

gene expression in cardiac progenitor cells and cardiomyocytes. *J. Biol. Chem.*, **272**, 22800–22808.

10) Kwok,J. and Richardson,D. (2002) Unexpected anthracyclinemediated alterations in iron-regulatory protein-RNA-binding activity: the iron and copper complexes of anthracyclines decrease RNA-binding activity. *Mol. Pharmacol.*, **62**, 888–900.

11) Kwok,J. and Richardson,D. (2003) Anthracyclines induce accumulation of iron in ferritin in myocardial and neoplastic cells: inhibition of the ferritin iron mobilization pathway. *Mol. Pharmacol.*, **63**, 849–861.

12) Hentze,M. and Kuhn,L. (1996) Molecular control of vertebrate iron metabolism: mRNA-based regulatory circuits operated by iron, nitric oxide, and oxidative stress. *Proc. Natl Acad. Sci. USA*, **93**, 8175–8182.

13) Gewirtz,D. (1999) A critical evaluation of the mechanisms of action proposed for the antitumor effects of the anthracycline antibiotics adriamycin and daunorubicin. Biochem. *Pharmacol.*, **57**, 727–741.

14) Saad,S., Najjar,T. and Al-Rikabi,A. (2001) The preventive role of deferoxamine against acute doxorubicin-induced cardiac, renal and hepatic toxicity in rats. *Pharmacol. Res.*, **43**, 211–218.

15) Rabbani,A., Iskandar,M. and Ausio,J. (1999) Daunomycin-induced unfolding and aggregation of chromatin. *J. Biol. Chem.*, **274**, 18401–18406.

16) Minotti,G., Cairo,G. and Monti,E. (1999) Role of iron in anthracycline cardiotoxicity: new tunes for an old song? *FASEB J.*, **13**, 199–212.

17) Hentze,M., Muckenthaler,M. and Andrews,N. (2004) Balancing acts: molecular control of mammalian iron metabolism. *Cell*, **117**, 285–297.

18) Oliveira,C., Goossen,B., Zanchin,N., McCarthy,J., Hentze,M. and Stripecke,R. (1993) Translational repression by the human ironregulatory factor (IRF) in Saccharomyces cerevisiae. *Nucleic Acids Res*., **21**, 5316–5322.

19) Piccinelli,P. and Samuelsson,T. (2007) Evolution of the ironresponsive element. *RNA*, **13**, 952–966.

20) Zeman,S., Phillips,D. and Crothers,D. (1998) Characterization of covalent adriamycin-DNA adducts. *Proc. Natl Acad. Sci*., **95**, 11561–11565.

21) Chaires,J., Satyanarayana,S., Suh,D., Fokt,I., Przewloka,T. and Priebe,W. (1996) Parsing the free energy of anthracycline antibiotic binding to DNA. *Biochemistry*, **35**, 2047–2053.

22) Rabbani,A., Finn,R., Thambirajah,A. and Ausio,J. (2004) Binding of antitumor antibiotic daunomycin to histones in chromatin and in solution. *Biochemistry*, **43**, 16497–16504.

23) Chaires,J., Dattagupta,N. and Crothers,D. (1982) Studies on interaction of anthracycline antibiotics and deoxyribonucleic acid: equilibrium binding studies on the interaction of daunomycin with deoxyribonucleic acid. *Biochemistry*, **21**, 3933–3940.

24) Chaires,J. (1990) Biophysical chemistry of the daunomycin-DNA interaction. *Biophys. Chem*., **35**, 191–202

25) Fritzsche,H. and Berg,H. (1987) Analysis of equilibrium, kinetic and structural data of anthracycline-DNA interaction. *Gazz. Chim. Ital*., **117**, 331–352.

26) Priebe,W. (1995) Mechanism of action-governed design of anthracycline antibiotics: a ‘‘turn-off/turn-on’’ approach. *Curr. Pharmaceut. Design*, **1**, 51–68.

27) Graves,D.E. and Krugh,T.R. (1983) Adriamycin and daunorubicin bind in a cooperative manner to deoxyribonucleic acid. *Biochemistry*, **22**, 3941–3947.

28) Pullman,B. (1991) Sequence specificity in the binding of anti-tumour anthracyclines to DNA: a success of theory. *Anticancer Drug Des*., **6**, 95–105.

29) Proctor,D., Kierzek,E., Kierzek,R. and Bevilacqua,P. (2003) Restricting the conformational heterogeneity of RNA by specific incorporation of 8-bromoguanosine. *J. Am. Chem. Soc*., **125**, 2390–2391.

30) Thomas,J., Liu,X. and Hergenrother,P. (2005) Size-specific ligands for RNA hairpin loops. *J. Am. Chem. Soc*., **127**, 12434–12435.

31) Tang,K., Pan,N., Zhang,Y. and Zou,G. (2005) Studies of adriamycin binding to histone H1 by resonant mirror biosensor and fluorescence spectroscopy. *Anal. Lett*., **38**, 2151–2164.

32) McPike,M., Goodisman,J. and Dabrowiak,J. (2001) Drug-RNA footprinting. *Methods Enzymol*., **340**, 431–449.

33) Mei,H., Cui,M., Heldsinger,A., Lemrow,S., Loo,J., Sannes-Lowery,K., Sharmeen,L. and Czarnik,A. (1998) Inhibitors of protein-RNA complexation that target the RNA: specific recognition ofhuman immunodeficiency virus type 1 TAR RNA by small organic molecules. *Biochemistry*, **37**, 14204–14212.

34) Dassonneville,L., Hamy,F., Colson,P., Houssier,C. and Bailly,C. (1997) Binding of Hoechst 33258 to the TAR RNA of HIV-1. Recognition of a pyrimidine bulge-dependent structure. *Nucleic Acids Res*., **25**, 4487–4492.

35) Jaffrey,S., Haile,D., Klausner,R. and Harford,J. (1993) The interaction between the iron-responsive element binding protein and its cognate RNA is highly dependent upon both RNA sequence and structure. *Nucleic Acids Res*., **21**, 4627–4631.

36) Ke,Y., Wu,J., Leibold,E., Walden,W. and Thiel,E. (1998) Loops and bulge/loops in iron-responsive element isoforms influence iron regulatory protein binding. Fine-tuning of mRNA regulation? *J. Biol. Chem.*, **273**, 23637–23640.

37) Wang,C., Wu,Q., Li,C., Wang,Z., Ma,J., Zang,X. and Qin,N. (2007) Interaction of tetrandrine with human serum albumin:a fluorescence quenching study. *Anal. Sci.*, **23**, 429–433.

38) Lakowics,J.R. (1983) *Principles of Fluorescence Spectroscopy*, 2nd edn., Kluwer Academic, Plenum Publishers, New York, 257–265.

39) Job,P. (1928) Formation and stability of inorganic complexes in solution. *Ann. Chim.*, **9**, 113–203.

40) Horowitz,E. and Hud,N.V. (2006) Ethidium and proflavine binding to a 20,50-linked RNA duplex. *J. Am. Chem. Soc.*, **128**, 15380–15381.

41) Record,M.T., Ha,J. and Fisher,M. (1991) Analysis of equilibrium and kinetic measurements to determine thermodynamic origins of stability and specificity and mechanism of formation of site-specific complexes between proteins and helical DNA. *Methods Enzymol.*, **208**, 291–343.

42) Wilson,W.D., Tanious,F.A., Fernandez-Saiz,M. and Rigl,C.T. (1997) Evaluation of drug–nucleic acid interactions by thermal melting curves. In *Drug-DNA Interaction Protocols*. Humana Press Inc., Totowa, NJ, pp. 219–240.

43) Wang,A.H., Ughetto,G., Quigly,G. and Rich,A. (1987) Interactions between an anthracycline antibiotic and DNA: molecular structure of daunomycin complexed to d(CpGpTpApCpG) at 1.2-ANG. resolution. *Biochemistry*, **26**, 1152–1163.

44) Haj,H., Salerno,M., Priebe,W., Kozlowski,H. and Garnier- Suillerot,A. (2003) New findings in the study on the intercalation of bisdaunorubicin and its monomeric analogues with naked and nucleus DNA. *Chem. Biol. Interact*., **145**, 349–358.

45) Bagalkot,V., Farokhzad,O., Langer,R. and Jon,S. (2006) An aptamer–doxorubicin physical conjugate as a novel targeted drug-delivery platform. *Angew. Chem. Int. Ed*., **45**, 8149–8152.

46) Li,K., Davis,T.M., Bailly,C., Kumar,A., Boykin,D.W. and Wilson,W.D. (2001) A heterocyclic inhibitor of the Rev-RRE complex binds to RRE as a dimer. *Biochemistry*, **40**, 1150–1158.

47) Chaires,J., Herrera,J. and Waring,M. (1990) Preferential binding of daunomycin to 50ATCG and 50ATGC sequences revealed by footprinting titration experiments. *Biochemistry*, **29**, 6145–6153.

48) Varani,G. and McClain,W. (2000) The GU wobble base pair. *EMBO Rep*., **1**, 18–23.

49) Strobel,S., Cech,T., Usman,N. and Beigelman,L. (1994) The 2,6-diaminopurine riboside.5-methylisocytidine wobble base pair: an isoenergetic substitution for the study of G.U pairs in RNA. *Biochemistry*, **33**, 13824–13835.

50) Walden,W., Selezneva,A., Dupuy,J., Volbeda,A., Fontecilla- Camps,J., Theil,E. and Volz,K. (2006) Structure of dual function iron regulatory protein 1 complexed with ferritin IRE-RNA. *Science*, **314**, 1903–1908.

51) Erlitzki,R., Long,J. and Theil,E. (2002) Multiple, conserved ironresponsive elements in the 30-untranslated region of transferring receptor mRNA enhance binding of iron regulatory protein 2. *J. Biol. Chem*., **277**, 42579–42587.

52) Ke,Y. and Theil,E. (2002) An mRNA loop/bulge in the ferritin iron-responsive element forms in vivo and was detected by radical probing with Cu-1,10-phenantholine and iron regulatory protein footprinting. *J. Biol.Chem.*, **277**, 2373–2376.

53) Tibodeau,J., Fox,P., Ropp,P., Theil,E. and Thorp.,H. (2006) The up-regulation of ferritin expression using a small-molecule ligand to the native mRNA. *Proc. Natl Acad. Sci.*, **103**, 253–257.

54) Marcheschi RJ, Mouzakis KD, Butcher SE. (2009) Selection and characterization of small molecules that bind the HIV-1 frameshift site RNA. *ACS Chem Biol*. **4**, 844-54.

55) Qu,X., Wan,C., Becker,H.C., Zhong,D. and Zewail,A.H. (2001) The anticancer drug-DNA complex: femtosecond primary dynamics for anthracycline antibiotics function. *Proc. Natl Acad. Sci. USA*, **98**, 14212–14217.

CHAPTER 3: PREFERENTIAL BINDING OF ANTHRACYCLINES TO DNA MISMATCH BASE PAIRS

3.1 Known DNA/Anthracycline Interactions

Anthracyclines are powerful antineoplastic agents that are widely used for the treatment of leukemia, lymphoma, solid-tumors and Hodgkin's disease (1). The general structure of anthracyclines consists of two dissimilar moieties: a planar hydrophobic tetracyclic (aglycone) ring and a hydrophilic, basic sugar (glycone) moiety attached to the tetracyclic ring through a glycosidic linkage (Figure 3.1a). The aglycone moiety intercalates between adjacent base pairs of DNA while the amino sugar ring lies in the minor groove of the B-DNA double helix. Anthracycline-DNA interactions are among the best characterized in the literature (2-27). Several X-ray diffraction and NMR structural analyses have provided valuable information regarding the binding interactions of anthracyclines with DNA (2-10). Additionally, extensive thermodynamic, kinetic, footprinting and computational studies have furnished detailed evidence on the molecular basis of the interaction of these compounds with certain DNA sequences (11-21) Despite the extensive clinical utilization and successes achieved in characterizing anthracycline-DNA interactions, the exact mechanism of the anticancer activities of anthracyclines is still a subject of debate in the literature. Among the proposed mechanisms are topoisomerase II (topo II) inhibition via intercalating DNA, leading to inhibition of RNA and DNA synthesis, generation of pro-apoptotic free radicals and reactive oxygen species, inhibition of DNA strand separation (helicase activity) and direct membrane effects (28). Of these, the inhibition of intracellular topo II activity is still considered the primary mechanism of anticancer activity of anthracyclines because most other modes of action were demonstrated at concentrations well above the peak plasma concentration in patients undergoing anthracycline therapy (28, 29).

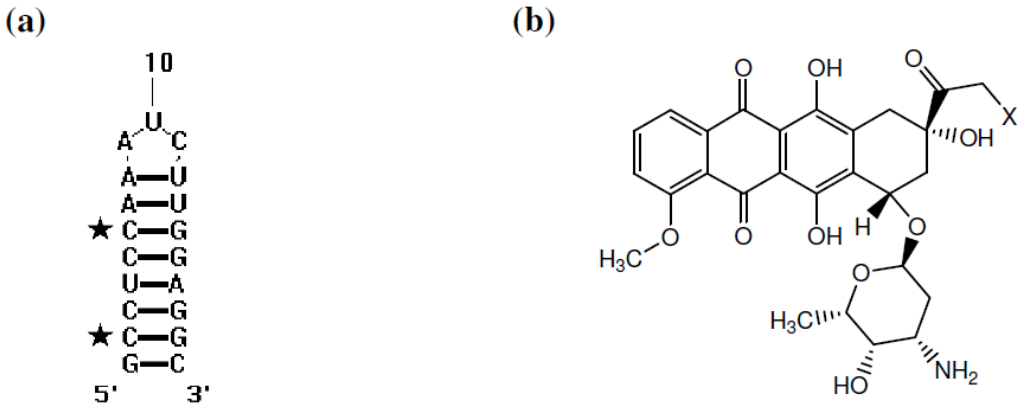

Figure 3.1 (**a**) Wild type (HWT) DNA hairpin structure (stars denote GT mutation sites), (**b**) X = OH, doxorubicin; X = H, daunomycin.

It has been observed that loss of the human mismatch repair (MMR) pathway confers resistance to structurally unrelated anthracyclines including doxorubicin (DOX) (30, 31). In an effort to unravel the connection between anthracyclines and MMR-dependent drug resistance, Larson and Drummond demonstrated that anthracyclines including DOX, DAU, nogalamycin and actinomycin directly inhibit the human MMR pathway (32). The authors suggested that drug intercalation proximal to a mismatch may disrupt structural features essential for the recognition of the base pair mismatch. And in tune with the futile repair model, repeated and failed attempts to remove DNA lesions by the mismatch repair protein, upon base mismatch binding by anthracyclines, could contribute to observed anthracycline cytotoxicity (33, 34). However, this elegant work could not be used to conclusively define the exact molecular mechanism by which anthracyclines disrupt MMR function.

There exists very little support for base mismatch binding by anthracyclines. First, the mismatch-recognition domain of the MMR protein contacts DNA on the minor groove side (35, 36). It is conceivable that the minor groove positioning of the glycone moiety could act as a steric impedance to the MMR protein binding to the base mispair. Supporting this steric impedance model is the observation that ethidium bromide, a DNA intercalator with a smaller minor groove binding moiety, inhibits MMR by about ten orders of magnitude less than DOX (32). Second, recent results from our lab suggest that anthracyclines preferentially bind to the GU wobble pair in ferritin iron-responsive element RNAs (37), thus it is quite possible that they may have a similar DNA base mismatch preference.

To probe the possibility of preferential anthracycline binding at or near DNA mismatches, we have designed three hairpins containing canonical base pairs (wild type) or single and double GT mismatch mutations (Figure 3.1b). We characterized the association of these hairpins with DOX and DAU, two clinically useful anthracyclines, using UV-melting, circular dichroism (CD), fluorescence quenching, and electrospray ionization mass spectrometry (ESI-MS) techniques. The results from these experiments revealed that DOX and DAU have binding preferences for the hairpins containing GT mismatches. An understanding of the binding preferences of anthracycline drugs will not only reveal the specifics of their induced MMR pathway inhibition, but should also prove to be valuable in the rational design of novel, anthracycline based derivatives and facilitate a more detailed assessment of the preferred targets of anthracyclines in the cell.

3.2) Biophysical Characterization of Anthracycline / Hairpin DNA Interaction

Oligonucleotides

The 19mer DNA hairpin targets were designed in such a way as to introduce a GT mismatch at two unique spots without compromising the hairpin structure (Figure 3.1b). A wild type construct with sequence 5'-GCCTCCAAATCTTGGAGGC-3' (designated HWT), a single mutation derivative introducing a C6T mutation with sequence 5'-GCCTCTAAATCTTGGAGGC-3' (designated H6), and a double mutant incorporating both a C6T and C2T mutation with sequence 5'-GTCTCTAAATCTTGGAGGC-3' (designated HD) were procured from the W.M Keck Facility at Yale University (New Haven, CT).

UV-vis melting and Circular Dichroism

UV melting experiments were performed in the absence of drug and in the presence of DOX and DAU at final drug concentrations of 5μM and 20μM. DNA and drug complexes were formed by the addition of an aliquot of stock drug solution in DMSO to a volume of DNA in BPE buffer (6mM Na_2HPO_4, 2 mM $Na_2H_2PO_4$, 1mM EDTA, pH 7.1). The mixture was allowed to equilibrate for at least 20 minutes at 4 ºC to ensure complete association. The drug stock was prepared so that upon reaching the desired concentration of drug, the amount of DMSO in the sample was no more than 1% (v/v). Melting studies were performed over a temperature range of 25-90 ºC, using a melting rate of 1 ºC/min data were collected every half degree. To form hairpins, constructs were heated at 99 ºC for one minute, then slowly cooled (1 ºC /min) to 10 ºC prior to being melted from 25-90 ºC (38). For melting experiments absorbance was measured at

260nm, the temperature was controlled with a Quantum Northwest TC 125 temperature control unit, drug concentration varied between 5 and 20 μM, and the concentration of DNA was held constant at 2.5μM. The T_m was taken as the midpoint of the melting transition as determined by the maxima of first derivative plots. All T_ms were reproducible to within ± 1ºC. The T_m of DNA in the absence of drug did not vary with increase in DNA concentration (Data not shown).

CD spectra were acquired on a JASCO J-810 CD spectropolarimeter at 25ºC and were baseline corrected by subtracting a buffer only spectrum. Samples were prepared in an identical fashion to those for UV-vis experiments. Each presented spectrum is the average of three individual scans.

Fluorescence Quenching Experiments

Quenching of a drug's fluorescence upon binding to DNA was monitored in titrations of a constant concentration of drug (7μM) with DNA of increasing concentration (0.1-20μM). Quenching experiments were performed in a 96 well black microplate following the protocol described by Hergenrother *et al.* (39). Fluorescence emission at 556nm was recorded on a Molecular Devices SpectraMAX Gemini microplate reader after excitation at 480nm. All experiments were repeated at least four times. The data collected in the fluorescence quenching titrations were fit to a second order decay curve utilizing TableCurve 2D v5.01, equation 8107 (39):

$$y = \frac{a * b}{b + x}$$

Where *b* is the apparent dissociation constant, x is the DNA concentration, *y* is the relative fluorescence intensity (I / I_o), and *a* is the asymptotic limit.

A stock solution of 4M NaCl in BPE buffer was diluted with BPE to achieve the various salt concentrations listed in the paper.

Mass Spectrometry

Drugs were dissolved in DMSO in stock solutions from 100 µM to 10 mM. The hairpins were annealed in BPE buffer by cooling the samples overnight from 90°C to room temperature. Annealed samples were stored at -20 °C. Each annealed hairpin (10 µM) was incubated with the desired concentration of the appropriate ligand for 20 minutes at 4 °C to allow for equilibration, and then 50 mM ammonium acetate was added prior to ESI-MS analysis to assist with desalting. ESI-MS was performed on a Thermo Scientific (San Jose, CA) LTQ-XL linear ion trap mass spectrometer. The source conditions were optimized to minimize disruption of the hairpin/ligand complexes by maintaining the capillary temperature at 90°C and source voltage at 3.5 kV. The tube lens voltage was set to -150 V, and all analyses were performed in the negative mode. The extent of DNA binding is expressed as a "relative binding percentage". For the calculation of relative binding percentages, peak areas were determined using Origin 7.0, and the peak areas of all hairpin/ligand complexes were summed and divided by the summed peak areas of all DNA species as shown in the equation below:

$$Relative\ Binding\ (\%) = \frac{PA_{\frac{HP}{L_1}} + PA_{\frac{HP}{L_2}} + \cdots + PA_{\frac{HP}{L_n}}}{PA_{HP} + PA_{\frac{HP}{L_1}} + PA_{\frac{HP}{L_2}} + \cdots + PA_{\frac{HP}{L_n}}} * 100$$

Where PA_{HP} is the peak area of the free hairpin and $PA_{HP/Ln}$ are the peak areas of the complexes containing each hairpin bound to n ligands. Higher values of the relative binding percentages indicate greater hairpin/ligand binding affinities. Three replicates were undertaken for each solution.

RESULTS

UV-vis melting and Circular Dichroism

The change in nucleic acid T_m after ligand binding ($\Delta T_m = T_m$ (DNA + ligand) - T_m (DNA)) is an indication of the affinity of the ligand for the nucleic acid. When comparing wild type to mutant DNA $\Delta\Delta T_m$ ($\Delta\Delta T_m = \Delta T_m$ (mutant) - ΔT_m (wild type)), is an indicator of the contribution of the mutation to the affinity of the drug for the target DNA (40). As an initial assessment of binding affinity, DNA targets were melted in the presence and absence of 5μM and 20μM either DOX or DAU. The resultant T_m and calculated ΔT_m and $\Delta\Delta T_m$ values are presented in Table 3.1. The wild type construct, HWT, produced a maximal shift in melting temperature of 15 °C in the presence of 20μM DOX. In comparison the H6 construct containing a single GT mismatch yielded a 21 °C increase in melting temperature under the same conditions. This represents an increase of 6 °C ($\Delta\Delta T_m$) when compared to HWT. More notably HD in the presence of 20μM DOX showed a $\Delta\Delta T_m$ value of 18 °C. A similar concentration dependent trend was seen in the interaction of DAU with the DNA hairpins. In the presence of 20μM DAU $\Delta\Delta T_m$ values of 7 °C and 16 °C were observed for H6 and HD respectively.

Table 3.1 Average T_m values (°C) and ΔG values (kcal mol^{-1}) for all drug and DNA hairpin combinations.

	HWT	H6	HD
Tm	61.4	46.3	24.7
5 µM DOX			
Tm	70.3	59.9	50.0
ΔTm	8.9	13.6	25.3
ΔΔTm		4.7	16.4
20 µM DOX			
Tm	75.7	66.9	57.5
ΔTm	14.3	20.6	32.8
ΔΔTm		6.3	18.5
5 µM DAU			
Tm	70.2	60.2	47.6
ΔTm	8.8	13.9	22.9
ΔΔTm		5.1	14.1
20 µM DAU			
Tm	75.2	67.0	55.4
ΔTm	13.8	20.6	30.7
ΔΔTm		6.8	16.9
DOX ΔG°	-0.2	-0.4	NA
DAU ΔG°	-0.3	-0.5	NA
DOX ΔG_T	-1.0	-1.2	NA
DOX $\Delta\Delta G_T$		-0.2	NA
DAU ΔG_T	-1.4	-1.7	NA
DAU $\Delta\Delta G_T$		-0.3	NA

The CD spectra of 2.5μM HWT, H6 and HD in the absence and presence of 20 μM DOX are presented in Figures 3.2a and 3.2b, respectively. The HWT construct in the absence of drug (Figure 3.2a, solid) produces a CD signal with clear positive and negative peaks at about 280nm and 250nm respectively. Similarly, construct HD in the absence of drug (Figure 3.2a, dashed) showed positive and negative CD signals, albeit with markedly less intensity than those of HWT. Hairpin H6 in the absence of drug (Figure2a, dotted) lacked the symmetry and intensity of the CD signal of HWT. Upon addition of 20 μM DOX, all three constructs showed a dramatic change in their CD signal (Figure 3.2b).

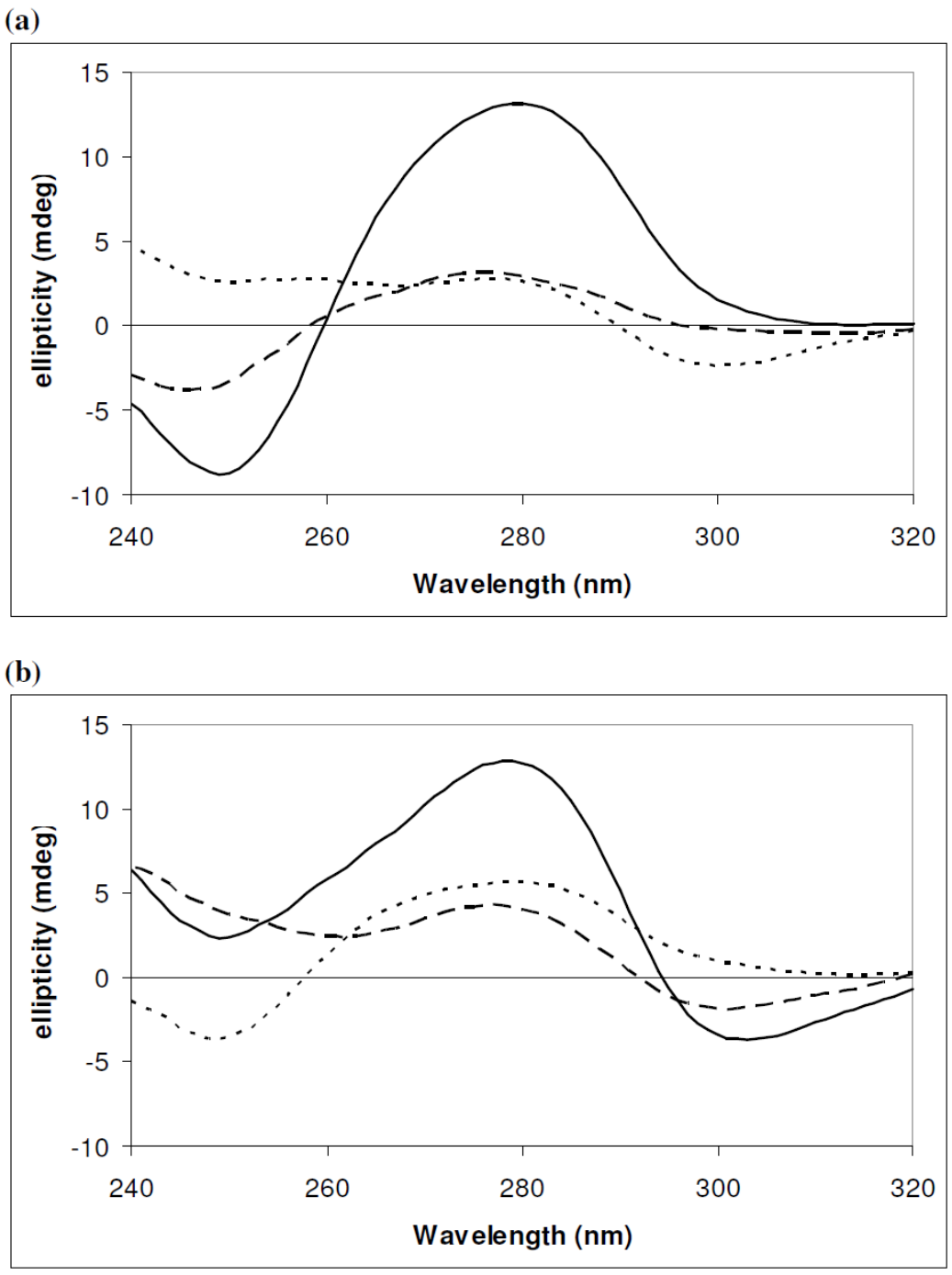

Figure 3.2 (**a**) CD spectra of 2.5 µM HWT (solid), H6 (dotted), and HD (dashed) DNA constructs in the absence of drug. (**b)** CD spectra of 2.5 µM HWT (solid), H6 (dotted), and HD (dashed) DNA constructs in the presence of 20 µM DOX.

Fluorescence Quenching

The conjugated ring system of anthracycline molecules makes them natural fluorophores and the binding of the molecule via intercalation leads to the quenching of this fluorescence (39). The natural fluorescence of DOX subsequent to excitation was monitored upon titration of increasing concentration of all three DNA constructs and the resulting data was used to compute thermodynamic parameters. The resultant decay curves in BPE were fitted and yielded apparent dissociation constants of 1.43 ± 0.077 μM, 1.20 ± 0.053 μM, and 1.22 ± 0.048 μM for HWT, H6 and HD, respectively. It is important to note that this apparent K_D is a total dissociation constant, and does not differentiate between the contribution of direct drug binding (e.g. intercalation) and the contribution of electrostatic interaction due to the charged nature of the anthracycline molecule.

To partition the binding free energies of anthracyclines with the DNA hairpins into their non-electrostatic and polyelectrolyte contributions, fluorescence quenching was monitored over a range of Na^+ concentrations, and a Stern-Volmer plot for each was plotted as described previously (18, 37). Stern-Volmer plots for HWT and H6 in the presence of both DOX and DAU can be found in Figure 3.3. Binding energy analysis was not done for HD because its T_m in the absence of drug is near room temperature. The quenching constant (K_{sv}) was determined for each curve and was then used to calculate the standard Gibbs free energy (ΔG°) using the equation:

$$\Delta G^\circ = -RT \ln K_{sv}$$

Where R is the gas constant (1.987 cal K^{-1} mol^{-1}) and T is the temperature in Kelvin. The wild type construct yielded K_{sv} values of 1.5×10^6 M^{-1} and 1.7×10^6 M^{-1} in the presence of DOX and DAU, respectively. The single mutant construct, H6, yielded K_{sv} values of 2.1×10^6 M^{-1} and

$2.3x10^6$ M^{-1} in the presence of DOX and DAU, respectively. A subsequent plot of log K_{sv} vs. log [Na^+] yielded the salt dependence of the binding constant defined by the slope (SK) of such plots. The SK value was used in the following equation to determine the polyelectrolyte contribution (ΔG_{pe}) at a given salt concentration (18):

$$\Delta G_{pe} = (SK)\ RT\ \ln\ [Na^+]$$

To determine the non-electrostatic contribution to binding energy, the thermodynamic free energy change (ΔG_t) was calculated according to the equation (18):

$$\Delta G_t = \Delta G^\circ - \Delta G_{pe}$$

The ΔG°, ΔG_t and $\Delta\Delta G_t$ values obtained for the binding of DOX and DAU to HWT and H6 (BPE buffer, 25°C, 16mM Na^+) can be found in Table 1. We observed that the free energies change associated with drug binding to the mutant hairpin are lower (i.e. stronger affinities) than that of the wild-type hairpin. The error associated with these values is estimated to be ±0.055 kcal mol^{-1}.

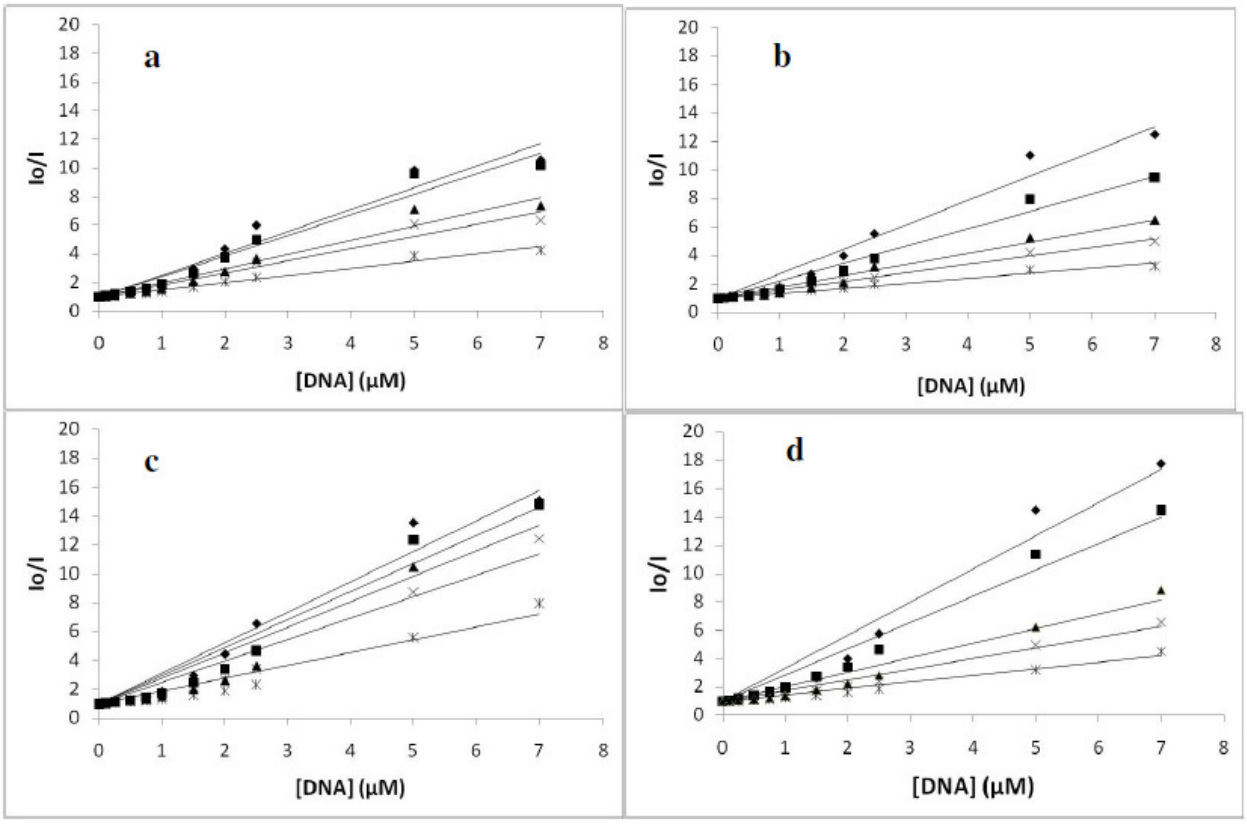

Figure 3.3 Stern-Volmer plots of 7 μM drug in the presence of DNA at the following Na+ concentrations: 16 mM (diamond), 46 mM (square), 116 mM (triangle), 216 mM (x), and 516 mM (star). **(a)** HWT and DOX, **(b)** HWT and DAU, **(c)** H6 and DOX, **(d)** H6 and DAU.

Mass Spectrometry

Electrospray ionization mass spectrometry (ESI-MS) was utilized to monitor the binding of drugs to all three DNA hairpin targets at various drug-DNA ratios. Hairpin/ligand complexes were abundant and easily identified in the resulting ESI-mass spectra. As an example, Figure 3.4 shows an ESI mass spectrum of hairpin HWT in the presence of 5 μM DOX (i.e. a 2:1 hairpin: ligand concentration ratio). Complexes containing up to two DOX ligands bound to the hairpin are observed. The deoxyoligonucleotides and complexes tend to have slightly higher levels of

salt adduction than are normally observed by ESI-MS due to the presence of the BPE buffer. The relative binding affinities of the ligands to each hairpin were calculated according to Equation 1 based on integration of peak areas of the various complexes and unbound hairpin in the ESI mass spectra for each incubate. The results of the ESI-MS analyses over a range of ligand concentrations (and a constant hairpin concentration of 10 μM) until virtually saturated at 20 μM ligand, are summarized in Figure 3.5. As expected, the relative binding percentages increase with increasing ligand concentration.

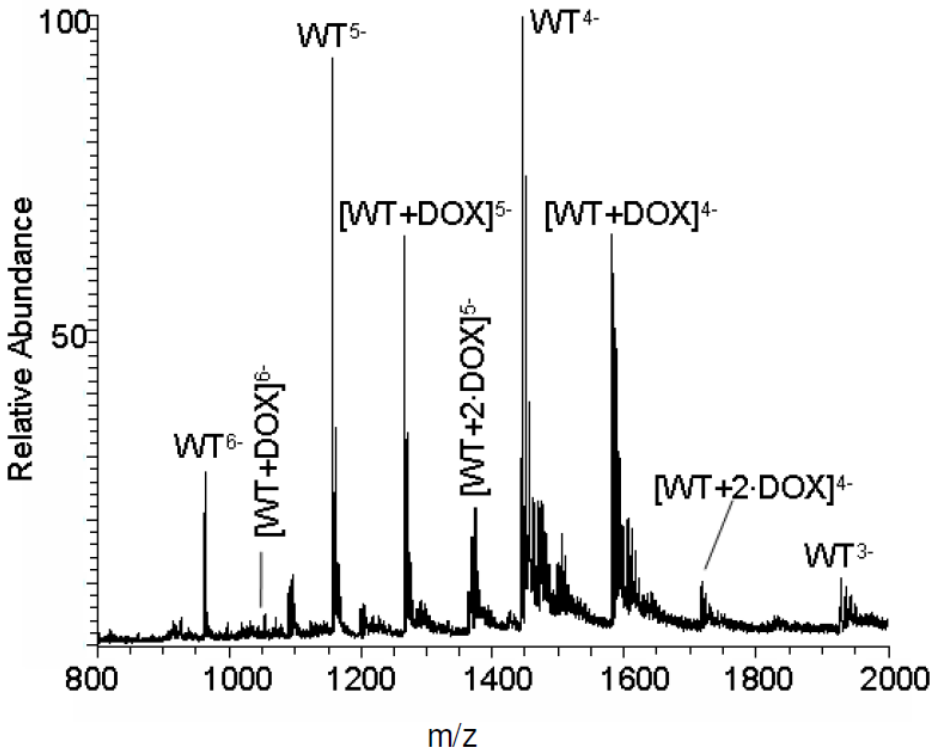

Figure 3.4 Negative ESI mass spectrum of hairpin HWT (10 μM) after incubation with DOX (5 μM).

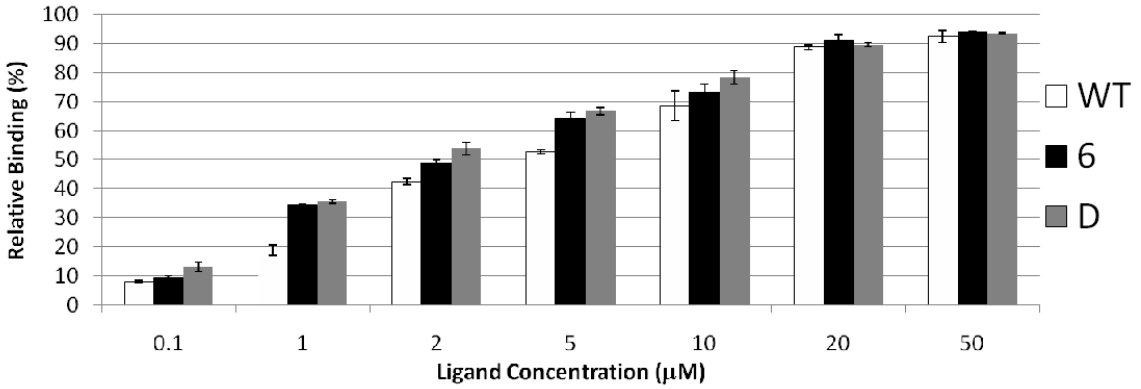

Figure 3.5 Relative binding percentages for the three hairpins HWT, H6, and HD with DOX at the given concentrations.

3.3) Discussion

The specific binding of anthracyclines to Watson-Crick DNA base pairs is well understood (2-27). However the exact mechanisms of anthracycline chemotherapeutic and cytotoxic effects are still not agreed upon in the literature. Furthermore, it remains unclear exactly how anthracyclines induce an inhibition of the human MMR pathway. Previous work by our group (37) provided a unique perspective from which to address these questions by investigating a possible DNA mismatch base pair preference of the anthracycline class of drugs. The affinity of the anthracycline molecule to bind at or near a mismatch base pair, such as the GT wobble pair, has not previously been evaluated to the best of our knowledge. The GT base pair imparts a unique geometry to the phosphodiester backbone of helical DNA (41) that may make it more accessible to a small molecule intercalator. The presence of a GT wobble pair has been shown to be an absolute necessity in some molecular recognition events (42).

In this article we provide evidence suggesting that DOX and DAU, two representative examples of clinically useful anthracyclines, exhibit greater binding affinities for DNA hairpins containing GT mismatches compared to the WT hairpin. The first evidence of this specificity is illustrated by the large positive $\Delta\Delta T_m$ values observed when comparing construct HWT to H6 and HD. An increase in melting temperature of 4 degrees or more is considered an indication of the preference of a ligand for a target (43). The $\Delta\Delta T_m$ values in the presence of 20 μM DOX and DAU for H6 of 6 °C and 7°C respectively and for HD of 19 °C and 17 °C, respectively (Table 3.1). The positive values of $\Delta\Delta T_m$ provide preliminary evidence for a strong specificity of anthracyclines for GT mismatch sites. It is important to note that the design of the double mismatch HD construct would allow binding of two DOX molecules at or near the mutation sites without violating the nearest neighbor exclusion rule (44). A more quantitative indicator of

binding affinity is the drug binding free energy difference between the wild-type and mutant hairpins ($\Delta\Delta G_t$) (18). As shown in Table 1, introduction of a single GT base mismatch favored (negative $\Delta\Delta G_t$) DOX and DAU binding to the mutant hairpin H6 by 0.2 and 0.3 kcal mol^{-1}, respectively. Although the magnitude of $\Delta\Delta G_t$ is small and we could not distinguish between two drugs, the data nevertheless is in agreement with the observed positive $\Delta\Delta T_m$ values. Together, these data give a clear indication of the preference of the drug molecule for the introduced mutation (18). Additionally, apparent dissociation constants for all three constructs in the very low micromolar range suggest a strong interaction between anthracycline and DNA.

Circular dichroism has been used to characterize anthracyclines and the binding of anthracyclines to DNA targets (45-49). Changes in the CD spectrum of an oligo in the presence and absence of drug, or in comparing wild type to mutant constructs under similar conditions, can be used to determine if there are changes in the oligos secondary structure. Changes in this structure could point to changes in the binding environment of the ligand. Thus, comparison of CD spectra (Figure 3.2a and 3.2b) allows a glimpse at changes in the structure of the DNA hairpins upon DOX binding. As expected, the CD signal of HWT in the absence of drug (Figure 3.2a) is characteristic of a B-form DNA helix (47, 48). Also as expected the mutant constructs H6 and HD do not yield the symmetry or intensity of HWT's CD signal as their structures are likely altered by the presence of the GT mismatches. This difference in the mutant constructs' CD spectra could indicate a unique small molecule binding environment when compared to the HWT hairpin. The marked changes in the CD spectra of all three constructs upon incubation with the drugs (Figure 3.2b) are further evidence of ligand binding and subsequent induced changes in structure. The enhanced binding of drug to the mutant DNA hairpins may be related to not only the structure of DNA before binding, but also to the propagated structural changes to the helix

subsequent to the binding of one or more drug molecules (50). The structural changes to the double stranded DNA helix are expected to be evident in the mutant hairpins, relative to the wild-type, due to ease of unwinding at or near the base mismatch sites. It is these changes in structure that have been proposed to be related to the observed MMR pathway inhibition by anthracyclines (32).

Electrospray ionization (ESI) allows the transfer of non-covalent complexes from solution to the gas-phase, thus facilitating the analysis of many types of biological complexes by mass spectrometry. This permits the study of duplex (51-53), triplex (54) and quadruplex (54-60) DNA structures, as well as the determination of binding selectivities, stoichiometries, and binding affinities of metal-mediated DNA complexes (61, 62), DNA/protein complexes (63, 64), and other DNA/ligand complexes (61, 65-70). Perhaps the most compelling evidence for the possible drug GT mismatch preference comes from the ESI-MS results (Figure 3.4). First, the detection of DNA-drug complexes suggests that these complexes are sufficiently stable even in the gas phase. More importantly however, comparison of the relative binding percentages for DOX and DAU concentration ranging from 1 to 10 μM indicate that they exhibit greater binding affinities for the mismatched hairpins H6 and HD compared to the HWT hairpin (Figure 3.5). The differences were significant to a 95% confidence interval in most cases. For the solutions containing the greater ligand concentrations (20 and 50 μM), the relative binding percentages were similar for all three hairpins (Figure 3.5), suggesting a possible drug saturation at higher ligand concentrations.

Collectively, the evidence presented in this study suggests a strong and specific preference of the anthracycline drugs for GT mismatch base pairs. This result agrees with our previous observations regarding the specificity of anthracyclines for RNA GU mismatches (37).

While it cannot be said with certainty that the preferential interaction of drug at mismatch sites, and the resulting change in binding environment, plays a role in anthracycline induced MMR pathway inhibition, it does corroborate the theory proposed by Larson and Drummond (32). Further studies involving anthracycline derivatives, namely derivatives with changes made to the glycone moiety of the molecule, will be needed to assess the exact structural basis for MMR inhibition resultant to anthracycline exposure. A detailed understanding of this interaction could prove to help elucidate the preferred nucleic acid targets of anthracycline drugs. In turn this will facilitate the future design of unique, anthracycline based drugs to be employed not only as structural probes, but also as novel therapeutic agents with differential pharmacokinetic parameters. Toward this end, one of the ongoing efforts in our lab is the design, synthesis, and characterization of novel anthracycline derivatives.

This work was done in collaboration with Sarah E. Pierce and Dr. Jennifer S. Brodbelt at The University of Texas at Austin. With the exception of the ESI-MS results, Joshua Canzoneri performed all other work presented.

3.4 References

1) Singal, P., Iliskovic, N., (1998) Doxorubicin-induced cardiomyopathy. *N Engl J Med* **339**, 900-905.

2) Quigley, G.J., Wang, A. H.-J., Ughetto, G., van der Marel, G., van Boom, J.H., Rich, A. (1980) Molecular structure of an anti cancer drug-DNA complex: Daunomycin plus d(CpGpTpApCpGp). *Proc Natl Acad Sci USA* **77**, 7204-7208.

3) Wang, A. H.-J., Ughetto, G., Quigley, G. J., Rich, A. (1987) The interactions between an anthracycline antibiotic and DNA: Molecular structure of daunomycin complexed to d(CpGpTpApCpG) at 1.2 Å resolution. *Biochemistry* **26***,* 1152-1163.

4) Coll, M., Frederick, C.A., Wang, A, H-J., Rich, A. (1987) A bifurcated hydrogen-bonded conformation in the d(AT) base pairs of the DNA dodecamer d(CGCAAATTTGCG) and its complex with distamycin. *Proc Natl Acad Sci USA* **84**, 8385-8389.

5) Frederick, C.A., Williams, L.D., Ughetto, G., van der Marel, G.A., van Boom, J.H., Rich, A., Wang, A. H.-J. (1990) Structural comparison of anticancer drug-DNA complexes: Adriamycin and daunomycin. *Biochemistry* **29**, 2538-2549.

6) Williams, L.D., Frederick, C.A., Ughetto, G., Rich, A. (1990) Ternary interactions of spermine with DNA: 4`-epiadrriamycin and other DNA: anthracycline complexes. *Nucleic Acids Res* **18**, 5533-5541.

7) Wang, A. H.-J., Gao, Y.-G., Liaw, Y.-C., Li, Y.-K. (1991) Formaldehyde crosslinks daunorubicin and DNA efficiently: HPLC and X-ray diffraction studies. *Biochemistry* **30***,* 3812-3815.

8) Zhang, H., Gao, Y.-G., van der Marel, G. A., van Boom, J. H., Wang, A. H.-J. (1993) Simultaneous incorporations of two anticancer drugs into DNA:The structures of formaldehyde-crosslinked adducts of daunorubicin-d(CG[araC]GCG) and doxorubicin-d(CA[araC]GTCG) complexes. *J Biol Chem* **268***,* 10095 - 10101.

9) Leonard, G. A., Hambley, T. W., McAuley-Hecht, K., Brown, T., Hunter, W. N. (1993) Anthracycline-DNA interactions at unfavourable base-pair triplet-binding sites: Structures of d(CGGCCG)/daunomycin and d(TGGCCA)/adriamycin complexes. *Acta Crystallogr* **D49***,* 458-467.

10) Hu, G. G., Shui, X., Leng, F., Priebe, W., Chaires, J. B., Williams L. D. (1997) Structure of a DNA-bisdaunomycin complex. *Biochemistry* **36**, 5940 – 5946.

11) Chaires, J. B., Dattagupta, N., Crothers, D. M. (1982) Studies on interaction of anthracycline antibiotics and deoxyribonucleic acid: equilibrium binding studies on interaction of daunomycin with deoxyribonucleic acid. *Biochemistry* **21***,* 3933-3940.

12) Graves, D. E., Krugh, T. R. (1983) Adriamycin and daunorubicin bind in a cooperative manner to deoxyribonucleic acid. *Biochemistry* **22,** 3941–3947.

13) Chaires, J. B., Dattagupta, N., Crothers, D. M. (1985) Kinetics of the daunomycin-DNA interaction. *Biochemistry* **24**, 260-267.

14) Fritzsche, H., Berg, H. (1987) Analysis of equilibrium, kinetic and structural data of anthracycline-DNA interaction. *Gazz Chim Ital* **117**, 331-352.

15) Rizzo, V., Sacchi, N., Menozzi, M. (1989) Kinetic studies of anthracycline-DNA interaction by fluorescence stopped flow confirm a complex association mechanism. *Biochemistry* **28**, 274-282.

16) Chaires, J. B., Herrera, J. E., Waring, M. J. (1990) Preferential binding of daunomycin to 5'TACG and 5'TAGC sequences revealed by footprinting titration experiments. *Biochemistry* **29**, 6145-6153.

17) Pullman, B. (1991) Sequence specificity in the binding of anti-tumor anthracyclines to DNA: A success of theory. *Anti-Cancer Drug Des* **6**, 95-105.

18) Chaires, J. B., Satyanarayana, S., Suh, D., Fokt, I., Przewloka, T., Priebe, W. (1996) Parsing the free energy of anthracycline antibiotic binding to DNA. *Biochemistry* **35**, 2047 -2053.

19) Chaires, J. B., Leng, F., Przewloka, T., Fokt, I., Ling, Y-H., Perez-Soler, R., Priebe, W. (1997) Structure-based design of a new bisintercalating anthracycline antibiotic. *J Med Chem* **40**, 261 – 266.

20) Qu, X., Trent, J. O., Fokt, I., Priebe, W., Chaires, J. B. (2000) Allosteric, chiral-selective drug binding to DNA. *Proc Natl Acad Sci U.S.A.* **97**, 12032–12037.

21) Priebe, W. (1995) Mechanism of action-governed design of anthracycline antibiotics: A "turn-off/turn-on" approach. *Curr Pharmaceut Design* **1**, 51 -68.

22) Zeman, S., Phillips, D., Crothers, D. (1998) Characterization of covalent Adriamycin-DNA adducts. *Proc Natl Acad Sci* **95** 11561-11565.

23) Rabbani, A., Finn, R., Thambirajah, A., Ausio, J. (2004) Binding of antitumor antibiotic daunomycin to histones in chromatin and in solution. *Biochemistry* **43**, 16497-16504.

24) Chaires, J. (1990) Biophysical chemistry of the daunomycin-DNA interaction. *Biophys Chem* **35**, 191-202.

25) Neidle, S., Sanderson, A. (1983) The interaction of daunomycin and adryamycin with nucleic acids, *Molecular Aspects of Anti-cancer Drug Action* Verlag Chemie: Weiheim, **35**.

26) Patel, D. J., Kozlowski, S. A., Rice, J. A. (1981) Hydrogen bonding, overlap geometry and sequence specificty in anthracycline antitumor antibiotics: DNA complexes in solution. *Proc Nat Acad Sci* **78**, 3333.

27) Pearlman, L. P., Simpkins, H. (1985) The differential effects produced by daunomycin and adriamycin on RNA, polynucleotides, single stranded, supercoiled DNA and nucleosomes. *Biochem Biophys Res Comm* **131**, 1033.

28) Gewirtz, D. A. (1999) A critical evaluation of the mechanisms of action proposed for the antitumor effects of the anthracycline antibiotics adriamycin and daunorubicin. *Biochem Pharmacol* **57**, 727–741.

29) Minotti, G., Menna, P., Salvatorelli, E., Cairo, G., Gianni, L. (2004) Anthracyclines: molecular advances and pharmacologic developments in antitumor activity and cardiotoxicity. *Pharmacol Rev* **56**, 185-22.

30) Earnshaw, W. C., Halligan, B., Cooke, C. A., Heck, M. M. *S*., Liu, L. E. (1985) Topoisomerase II is a structural component of mitotic chromosome scaffolds. *J Cell Biol* **100**, 1706-1715.

31) DiNardo, S., Voelkel, K., Sternglanz, R. DNA (1984) Topoisomerase II mutant of Saccharomyces cerevisiae: Topoisomerase II is required for segregation of daughter molecules at the termination of DNA replication. *Proc Natl Acad Sci USA* **81**, 2616-2120.

32) Larson, E. D. Drummond, J. T. (2001) Human mismatch repair and G-T mismatch binding by hMutS *in vitro* is inhibited by adriamycin, actinomycin D, and nogalamycin. *J Biol Chem* **276**, 9775-9783.

33) Karran, P., Bignami, M. (1994) DNA damage tolerance, mismatch repair and genome instability. *Bioessays* **16**, 833-839.

34) Goldmacher, V. S., Cuzick, R. A., Jr, Thilly, W. G. (1986) Isolation and partial characterization of human cell mutants differing in sensitivity to killing and mutation by methylnitrosourea and N-methyl-N'-nitro-N-nitrosoguanidine. *J Biol Chem* **261**, 12462–12471.

35) Lamers, M. H., Perrakis, A., Enzlin, J. H., Winterwerp, H. H. K., de Wind, N., Sixma, T.K. (2000) The crystal structure of DNA mismatch repair protein MutS binding to a G-T mismatch. *Nature* **407**, 711-717.

36) Obmolova, G., Ban, C., Hsieh, P., Yang, W. (2000) Crystal structures of mismatch repair protein MutS and its complex with a substrate DNA. *Nature* **407**, 703-710.

37) Canzoneri, J. C., Oyelere, A. K. (2008) Interaction of anthracyclines with iron responsive element mRNAs. *Nucleic Acids Res*, **36**, 6825-6834.

38) Proctor, D., Kierzek, E., Kierzek, R., Bevilacqua, P. (2003) Restricting the conformational heterogeneity of RNA by specific incorporation of 8-bromoguanosine. *J Am Chem Soc* **125**, 2390-2391.

39) Thomas, J., Liu, X., Hergenrother, P. (2005) Size-specific ligands for RNA hairpin loops**.** *J AmChem Soc* **127**, 12434-12435.

40) Ortega, J-A., Blas, J. R., Orozco, M., Grandas, A., Pedroso, E., Robles, J. (2007) Binding affinities of oligonucleotides and PNAs containing phenoxazine and G-clamp cytosine analogues are unusually sequence-dependent. *Org Lett* **9**, 4503-4506.

41) Early, T. A., Olmsted, J. III, Kearns, D. R., Lezius, A. G. (1978) Base pairing structure in the poly d(GT) double helix: wobble base pairs. *Nucleic Acids Res* **5**, 1955-1970.

42) Spiro, C., Richards, J. P., Chandrasekaran, S., Brennan, R. G., McMurray, C.T. (1993) Secondary structure creates mismatched base pairs required for high-affinity binding of cAMP response element-binding protein to the human enkephalin enhancer. *Proc Natl Acad Sci USA* **90**, 4606-4610.

43) Wilson, W. D., Tanious, F. A., Fernandez-Saiz, M., Rigl, C. T. (1997) Evaluation of drug–nucleic acid interactions by thermal melting curves. *Drug-DNA Interaction Protocols* Humana Press Inc.,Totowa, NJ, 219-240.

44) Chaires, J., Dattagupta, N., Crothers, D. (1982) Studies on interaction of anthracycline antibiotics and deoxyribonucleic acid: equilibrium binding studies on the interaction of daunomycin with deoxyribonucleic acid. *Biochemistry* **21**, 3933-3940.

45) Li, X., Peng, Y., Ren, J., Qu, X. (2006) Effect of DNA flanking sequence on charge transport on short DNA duplexes. *Biochemistry* **45**, 13543-13550.

46) Suh, D., Oh, Y., Ahn, B., Hur, M., Kim, H., Lee, M., Joo, H., Auh, C. (2002) Comparitive binding of antitumor drugs to DNA containing the telomere repeat sequence. *Exp Mol Med* **34**, 326-331.

47) Horowitz, E.D., Hud, N.V. (2009) Ethidium and proflavine binding 2`,5`-linked RNA duplex. *J Am Chem Soc* **128**, 15380-15381.

48) Fiallo, M.M., Tayeb, H., Suarato, A., Garnier-Suillerot, A. (1998) Circular dichroism studies on anthracycline antitumor compounds- relationship between the molecular structure and the spectroscopic data. *J Pharm Sci* **87**, 967-975.

49) Cera, C., Palu, G., Marciano Magno, S., Palumbo, M. (1991) Interaction between second generation anthracyclines and DNA in the nucleosomal structure. *Nucleic Acids Res* **19**, 2309-2314.

50) Williams, L.D., Gao, Q. (1992) DNA-ditercalinium interactions: Implications for recognition of damaged DNA. *Biochemistry* **31**, 4315-4324.

51) Gabelica, V., De Pauw, E. (2002) Collision-induced dissociation of 16-mer DNA duplexes with various sequences: evidence for conservation of the double helix conformation in the gas phase. *Int J Mass Spectrom* **219**, 151-159.

52) Gabelica, V., De Pauw, E. (2002) Comparison of the collision-induced dissociation of duplex DNA at different collision regimes: evidence for a multistep dissociation mechanism. *J Am Soc Mass Spectrom* **13**, 91-98.

53) Hofstadler, S. A., Griffey, R. H. (2001) Analysis of noncovalent complexes of DNA and RNA by mass spectrometry. *Chem Rev (Washington, D. C.)* **101**, 377-390.

54) Rosu, F., Gabelica, V., Houssier, C., Colson, P., De Pauw, E. (2002) Triplex and quadruplex DNA structures studied by electrospray mass spectrometry. *Rapid Commun Mass Spectro* **16**, 1729-1736.

55) Baker, E. S., Bernstein, S. L., Gabelica, V., De Pauw, E., Bowers, M. T. (2006) G-quadruplexes in telomeric repeats are conserved in a solvent-free environment. *Int J Mass Spectrom* **253**, 225-237.

56) David, W. M., Brodbelt, J., Kerwin, S. M., Thomas, P. W. (2002) Investigation of quadruplex oligonucleotide-drug interactions by electrospray ionization mass spectrometry. *Anal Chem* **74**, 2029-2033.

57) Gabelica, V., Rosu, F., Witt, M., Baykut, G., De Pauw, E. (2005) Fast gas-phase hydrogen/deuterium exchange observed for a DNA G-quadruplex. *Rapid Commun Mass Spectrom* **19**, 201-208.

58) Guo, X., Liu, S., Yu, Z. (2007) Bimolecular Quadruplexes and Their Transitions to Higher-Order Molecular Structures Detected by ESI-FTICR-MS. *J Am Soc Mass Spectrom* **18**, 1467-1476.

59) Rosu, F., De Pauw, E., Guittat, L., Alberti, P., Lacroix, L., Mailliet, P., Riou, J. F., Mergny, J. L. (2003) Selective interaction of ethidium derivatives with quadruplexes: an equilibrium dialysis and electrospray ionization mass spectrometry analysis. *Biochemistry* **42**, 10361-10371.

60) Rosu, F., Gabelica, V., Shin-ya, K., De Pauw, E. (2003) Telomestatin-induced stabilization of the human telomeric DNA quadruplex monitored by electrospray mass spectrometry. *Chem Comm* **7**, 2702-273.

61) Beck, J. L., Colgrave, M. L., Ralph, S. F., Sheil, M. M. (2001) Electrospray ionization mass spectrometry of oligonucleotide complexes with drugs, metals, and proteins. *Mass Spectrom Rev* **20**, 61-87.

62) Mazzitelli, C. L., Rodriguez, M., Kerwin, S. M., Brodbelt, J. S. (2008) Evaluation of metal-mediated DNA binding of benzoxazole ligands by electrospray ionization mass spectrometry. *J Am Soc Mass Spectrom* **19**, 209-218.

63) Cheng, X., Harms, A. C., Goudreau, P. N., Terwilliger, T. C., Smith, R. D. (1996) Direct measurement of oligonucleotide binding stoichiometry of gene V protein by mass spectrometry. *Proc Natl Acad Sci USA* **93**, 7022-7027.

64) Akashi, S., Osawa, R., Nishimura, Y. (2005) Evaluation of protein-DNA binding affinity by electrospray ionization mass spectrometry. *J Am Soc Mass Spectrom* **16**, 116-125.

65) Colgrave, M. L., Beck, J. L., Sheil, M. M., Searle, M. S. (2002) Electrospray ionisation mass spectrometric detection of weak non-covalent interactions in nogalamycin-DNA complexes. *Chem Comm* **6**, 556-557.

66) Apruzzese, W. A., Vouros, P. (1998) Analysis of DNA adducts by capillary methods coupled to mass spectrometry: a perspective. *J Chromatogr A* **794**, 97-108.

67) Smith, S. I., Guziec, L. J., Guziec, F. S., Hasinoff, B. B., Brodbelt, J. S. (2007) Evaluation of relative DNA binding affinities of anthrapyrazoles by electrospray ionization mass spectrometry. *J Mass Spectrom* **42**, 681-688.

68) Iannitti-Tito, P., Weimann, A., Wickham, G., Sheil, M. M. (2000) Structural analysis of drug-DNA adducts by tandem mass spectrometry. *Analyst* **125**, 627-633.

69) Mazzitelli, C. L., Brodbelt, J. S., Kern, J. T., Rodriguez, M., Kerwin, S. M.(2006) Investigation of silver binding to polyamidoamine (PAMAM) dendrimers by ESI tandem mass spectrometry. *J Am Soc Mass Spectrom* **17**, 593-604.

70) Mazzitelli, C. L., Chu, Y. J., Reczek, J. J., Iverson, B. L., Brodbelt, J. S. (2007) Screening of threading bis-intercalators binding to duplex DNA by electrospray ionization tandem mass spectrometry. *J Am Soc Mass Spectrom* **18**, 311-321.

CHAPTER 4: EXPLORING THE RIBOSOME WITH NOVEL MACROLIDE-PEPTIDE CONJUGATES

4.1 Architecture of the Ribosomal Exit Tunnel

The ribosome is one the most complex molecular machines found in nature. The peptide producing mechanisms of the ribosome are so finely orchestrated and perfectly tuned that they are one of the more conserved features in the tree of life. Once described simply as a small particle containing peptides and nucleic acids, the ribosome is far better understood today, but still presents some mystery. While crystal structures have allowed the identity of all ribosomal components to be elucidated, the exact role that each of the structures play during translation remains unclear (1-4). The ribosomal exit tunnel is an example of such a component that has yet to be fully characterized. The 80 Å long, 20 Å wide, rRNA lined exit tunnel serves as the route of egress for nascent peptides to move away from the petidyl transferase center (PTC) towards the exterior surface of the ribosome (5,6). The unobstructed pathway from the PTC along the exit tunnel and out of the ribosome was initially believed to be Teflon-like in nature and to have little impact on the escape of the nascent chain. However, it has been shown that specific peptide sequences allow the nascent chain to interact with the walls of the exit tunnel, thereby influencing translation (7). While specific sequences have been identified to stall translation, it is still not fully understood why the majority of peptides pass through the tunnel unhindered while others can halt translation (8,9).

4.2 Peptolide Design and Synthesis

In an attempt to interrogate the exact nature of the exit tunnel, we describe here the rational design, synthesis and characterization of a novel class of peptide-ketolide ("peptolide") molecular probes. Ketolides are a class of antibiotic small molecules, largely known as macrolides, which interfere with the prokaryotic ribosome by physically blocking a portion of the exit tunnel near the PTC (Figure 4.1) (10). As an inspiration in the design of the peptolide probes we looked to the ketolide telithromycin (TEL). Unique to TEL is a flexible alkyl-aryl moiety (Figure 4.2a). This flexible arm of the TEL molecule has been shown via crystallographic studies to adopt several different binding motifs (11). The arm can either extend back up the exit tunnel towards the PTC, follow the expected path of a nascent chain down the exit tunnel away from the PTC, or extend to the side as observed in the large ribosome subunit (50S) from archaeal *Haloarcula marismortui* (H50S), bacterial *Deinococcus radiodurans* (D50S), and *E. coli,* respectively (Figure 4.2b).

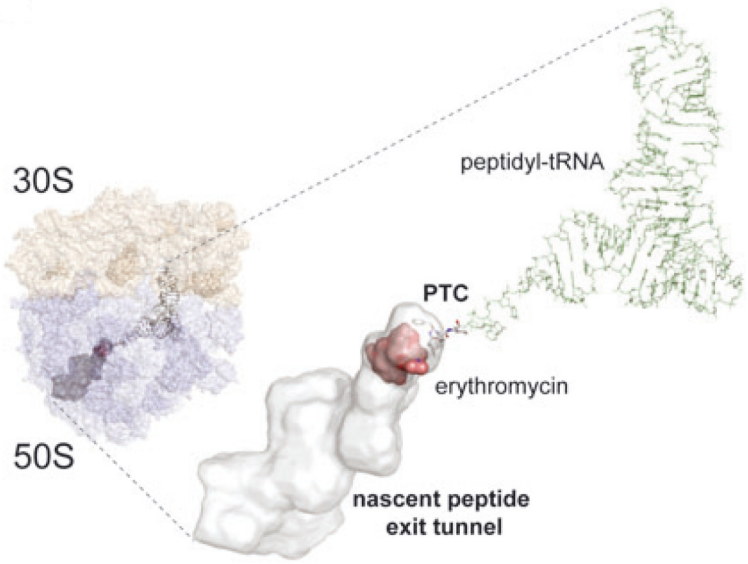

Figure 4.1 Erythromycin bound to the macrolide binding pocket adjacent to both the PTC and exit tunnel. The white surface indicates the walls of the exit tunnel. Figure adapted from (10).

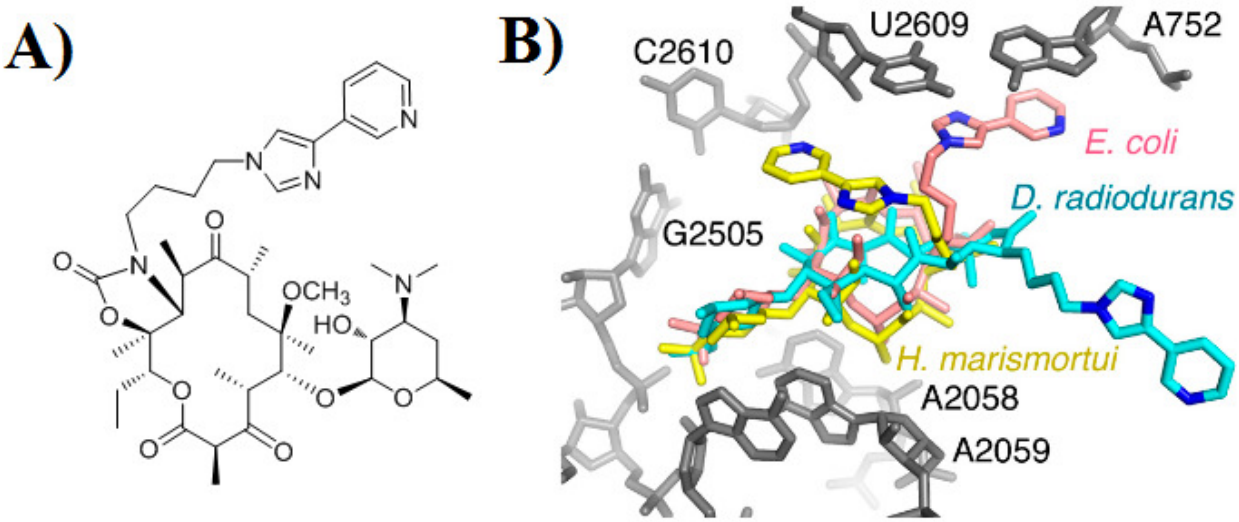

Figure 4.2 A) Structure of the macrolide class drug, telithromycin (TEL). B) Crystal structure of TEL bound to the large ribosomal subunit of H50S (gold, extending toward PTC), D50S (cyan, extending toward exit tunnel), and E. coli (pink) Figure adapted from (11).

It is evident in all three crystal structures that the bound TEL molecule is stabilized by similar stacking interactions between the aryl moiety of the arm and pyrimidine bases of the ribosomal rRNA. As long as this crucial energy minimizing interaction remains intact, it is feasible that the arm could be modified beyond the aryl group and allow new ligands to be added while preserving the antibiotic binding mode. By utilizing Cu (I) catalyzed Huigsen cycloaddition (click chemistry) as the crucial fragment joining reaction, we can replace the imidazole ring of the aryl group with the structural similar triazole linkage (Figure 4.3). Thus, the dynamic nature of TEL's aryl alkyl arm could provide an optimal, flexible linker by which to attach a variety of peptide moieties to the macrolide head group. By employing the macrolide as an anchor, any attached peptide sequence would be presented to the exit tunnel and its binding mode and affinity could be analyzed to glean insight as to the nature of interaction with the local environment.

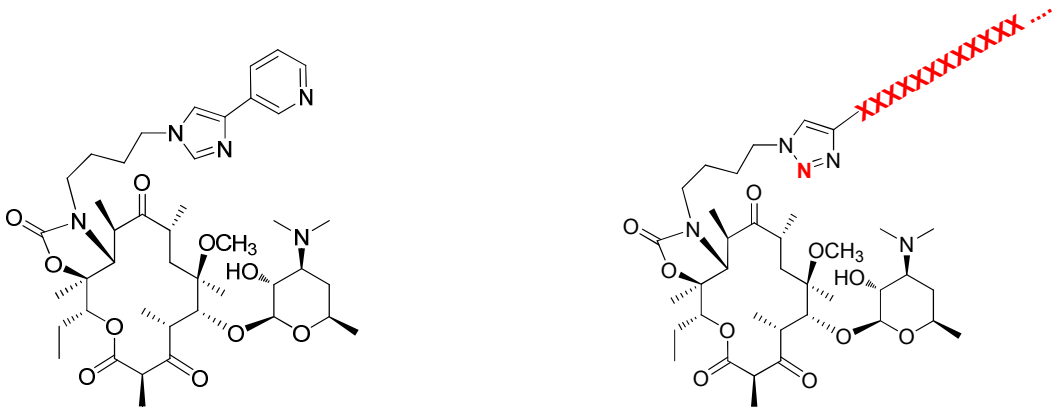

Figure 4.3 Changes (in red) to the TEL molecule (left) to yield the target peptolide probes (right).

We rationally designed and successfully synthesized a series of peptolide probes via an 11 step synthetic route starting with clarithromycin (Figure 4.4) (Synthesis performed by Derek Benicewicz). We created an azide-ketolide intermediate that could be used as the universal head group for all compounds created. Thus a peptide of any design, so long as it was functionalized with an alkyne, could be attached to create a complete peptolide. We produced four unique structural motifs by varying the peptide tail in amino acid composition, size and direction of attachment (Figure 4.4). Additionally, each of the four unique peptolide motifs were further differentiated by two linker lengths, 3 carbon and 4 carbon, or n=0 and n=1 respectively in Figure 4.4, between the ketolide and peptide, giving us a total of eight structurally differentiated peptolide probes. These probes were named by their linker length (3C or 4C) as well as by their protein tail identity (NLS, rNLS, RGD PLI) (Figure 4.4).

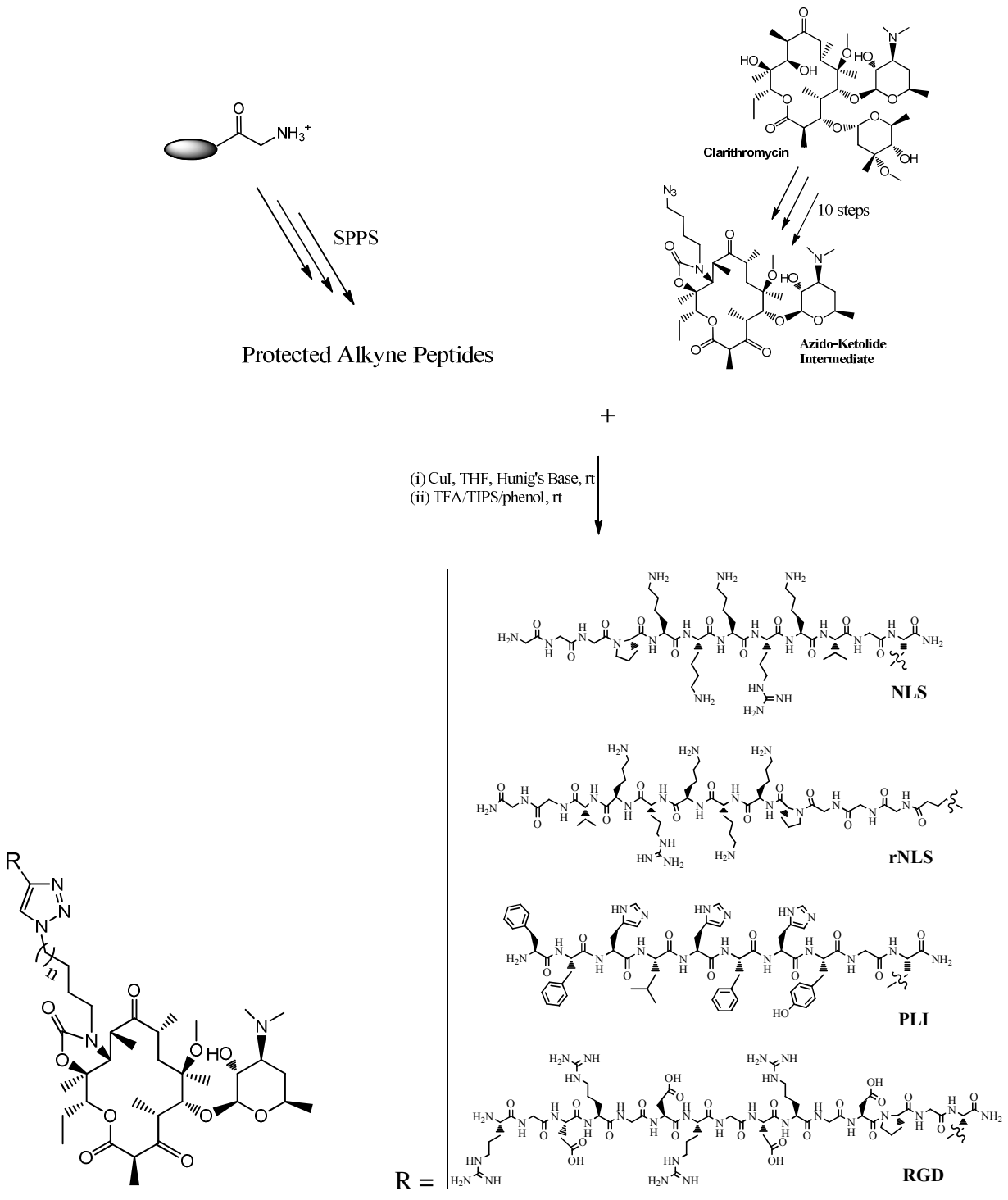

Figure 4.4 Synthetic scheme for peptolide molecules.

4.3 *In vitro* Cell Extract Inhibition Assays

As a first indication of the effects of our newly created peptolide probes on the fidelity of ribosomal function, we subjected them to a pair of distinct cell free transcription/translation assay kits and determined their inhibitory IC_{50} values. The first of the assays, representing a prokaryotic system, is based on a whole cell extract of *E. coli* (*E. coli* T7 S30 Extract System for Circular DNA, Promega). The second assay is a eukaryotic system comprised of rabbit reticulocyte whole cell extract (Rabbit Reticulocyte Lysate System, Nuclease Treated, Promega). Assays were performed in accordance with the suggested manufacturer's instructions (Promega) (12, 13). Both assays utilize a luciferase based reporter whereby protein expression, or the inhibition thereof, is monitored via the inherent luminescence of the encoded luciferase protein product. In the case of the prokaryotic system, transcription and translation occur simultaneously due to the lack of a defined nucleus. Thus a DNA template of the luciferase product is introduced to the reaction mixture for subsequent and simultaneous transcription and translation. In contrast, in the eukaryotic assay the production of luciferase is solely dependent on translation as only an RNA template of the luciferase product is present in the reaction mixture. Also tested for inhibition were the unattached peptides. The results of these assays can be found in Table 4.1.

Table 4.1 IC_{50} values of *in vitro*, cell free assays performed on peptolide compounds.

	E.coli	**Rabb. Retic.**
Description	IC50	IC50
NLS 3C	1.4 µM	> 250 µM
NLS 4C	1.0 µM	> 250 µM
NLS peptide	> 250 µM	> 250 µM
rNLS 3C	1.4 µM	> 250 µM
rNLS 4C	1.4 µM	> 250 µM
rNLS peptide	> 250 µM	> 250 µM
PLI 3C	4.6 µM	140 µM
PLI 4C	1.7 µM	38 µM
PLI peptide	>250 µM	205 µM
RGD 3C	60 µM	> 250 µM
RGD 4C	5.9 µM	> 250 µM
RGD only	> 250 µM	> 250 µM
macrolide only	1.8 µM	> 250 µM

4.4 Chemical Footprinting of *E. coli* 23S rRNA

Chemical footprinting of the *E. coli* 23S rRNA was performed with dimethyl sulfate (DMS) and 1-cyclohexyl-(2-morpholinoethyl)carbodiimide metho-p-toluene sulfonate (CMCT) according to the following protocol (14):

Peptolide Binding

All peptolides and the azido-macrolide precursor were incubated at a final concentration of 150 µM with 100 pmol *E. coli* 70S ribosome (New England Biolabs), whereas clarithromycin was incubated at a concentration of 50 µM. Binding was performed in binding buffer (10 mM HEPES, 10 mM $MgCl_2$, 60mM NH_4Cl) at 37°C for 30 minutes (15).

DMS Chemical modification

DMS chemical modification was performed on intact 70S *E. coli* ribosomes in the absence and presence of bound drug. Approximately 50 µg of intact ribosome, or ribosome-peptolide complex, in 25 µM DMS buffer (80 mM K-HEPES, 10 mM $MgCl_2$, 100 mM NH_4Cl) was alliquoted and to this was added 1 µl DMS Stock (880 mM DMS in abs. EtOH) and the mixture was then incubated for 10 minutes at 37°C. The reaction was terminated by the addition of 12.5 µl of DMS stop buffer (1 M tris-HCl, 0.1 M EDTA, 1 M 2-mercaptoethanol, pH7.5). Ethanol precipitation was followed by RNA extraction: The RNA pellet was resuspended in 400 µL extraction buffer [0.3 M NaOAc (pH 6.5), 0.5% SDS, 5 mM EDTA (pH 8.0)] at room temperature. This was subsequently extracted three times via addition of 400 µL of acid phenol chloroform (pH 4.5, Invitrogen). The final RNA fraction was ethanol precipitated and the pellet was resuspended in H_2O (0.4 µM). Aliquots were stored at -80^{o}C.

CMCT Modification

CMCT chemical modification was performed on intact 70S *E. coli* ribosomes in the absence and presence of bound drug. Approximately 50 µg of intact ribosome, or ribosome-peptolide complex, in 25 µM CMCT buffer (50 mM potassium borate pH 8.0, 10 mM $MgCl_2$, 100 mM NH_4Cl) was alliquoted and to this was added 12.5 µl CMCT Stock (100 mM CMCT in CMCT buffer) and the mixture was then incubated for 10 minutes at 37°C. The reaction was terminated by the addition of 2.5 volumes of -20°C 95% EtOH. Subsequent ethanol precipitation was followed by RNA extraction as described above.

Reverse Transcription

A list of primer sequences was generously provided by Dr. Alexander Mankin. DNA primers were purchased from Keck Biotechnology (New Haven, CT). An array of primers was initially purchase with the intent of covering as much of the 23S rRNA strand as possible. After footprinting analysis of all primers, the primer yielding the most useful data, named primer 2180, has the following sequence: 5`-GGGTGGTATTTCAAGGTCGG-3` . Primer 2180 is named as such because the 5` G of the primer anneals to position 2180 (*E. coli* numbering) of the 23S rRNA. Primer concentration was determined by UV-vis spectroscopy in 1 cm path length quartz cuvettes using molar extinction coefficients determined by OligoAnalyzer (IDT).

A working primer stock (2.0 µM) in H_2O was made fresh for each reaction. A hybridization buffer (225 mM K-Hepes pH 7.0, 450 mM KCl) was used to bring primer concentration to 1.0 µM. This primer mix (2 µL) was added to tubes containing RNA (0.8 µmol). Annealing proceeded by placing tubes in a water bath at 90^{o}C for 1 min, and allowed to cool to room temperature. While cooling, a master mix was prepared using 20 µL 5x First Strand Buffer (supplied with RT enzyme, Invitrogen), 150 µCi dATPα^{35}S (PerkinElmer), 6.6 µL

dNTP mix (110 μL 1mM d(T, G, C)TP, 6 μL 1 mM dATP, 664 μL H_2O), and 1 μL each of RNasin Plus (Promega) and 100 mM dithiothreitol (DTT).

Upon completion of annealing, samples were briefly centrifuged at room temperature. Each tube received 2 μL master mix and the sequencing tubes received the appropriate ddNTP (1 μL, 9 μM). Added last to each tube was 200U SuperScript II reverse transcripase (Invitrogen). Tubes were gently mixed and centrifuged before being placed in a heating block at 55°C for 30 minutes. Chase was initiated by addition of 1 μL dNTP (100 mM) to each tube and 1 μL appropriate ddNTP (402 mM) to sequencing tubes. Tubes were placed back in the heating block at 55°C for 15 minutes. The reaction was terminated by the addition of precipitation buffer (75 μL, 95% ethanol, 0.3 M NaOAc pH 6.5, 4°C) and centrifuged for 90 min (13,200 rpm, 4°C). The supernatant was removed and the pellets were dried and resuspended in 10 μL loading buffer (95% formamide, 10 mM EDTA, 0.1% xylene cyanol, 0.1% bromophenol blue, pH 11).

Gel Protocol

Samples were analyzed by running on a 5% polyacrylamide gel in a Sequi-Gen GT system (Bio Rad). The gel and 1x TBE buffer (100 mM Tris, 90 mM Boric Acid, and 1 mM EDTA) were brought to temperature by pre-running at 55 W to 50°C. Lanes were thoroughly flushed with buffer and loaded with 1 μL of sample each. Migration occurred from 45 to 90 min at 55W and 50°C. Gels were transferred to Whatman paper and were fixed in 20% EtOH for 20 min. They were then dried under vacuum for 90 min at 80°C. Once dry, gels were exposed onto a phosphor screen (GE Health care) overnight. Screens were scanned on a Typhoon Trio+ (GE Health care) and digital images were analyzed with Multi Gauge (FujiFilm).

The footprinting of *E. coli* 23S rRNA with primer 2180 and DMS modification in the presence of all peptolides can be found in Figure 4.5. Footprinting of CMCT modified 23S

rRNA with primer 2180 can be seen in Figure 4.6.

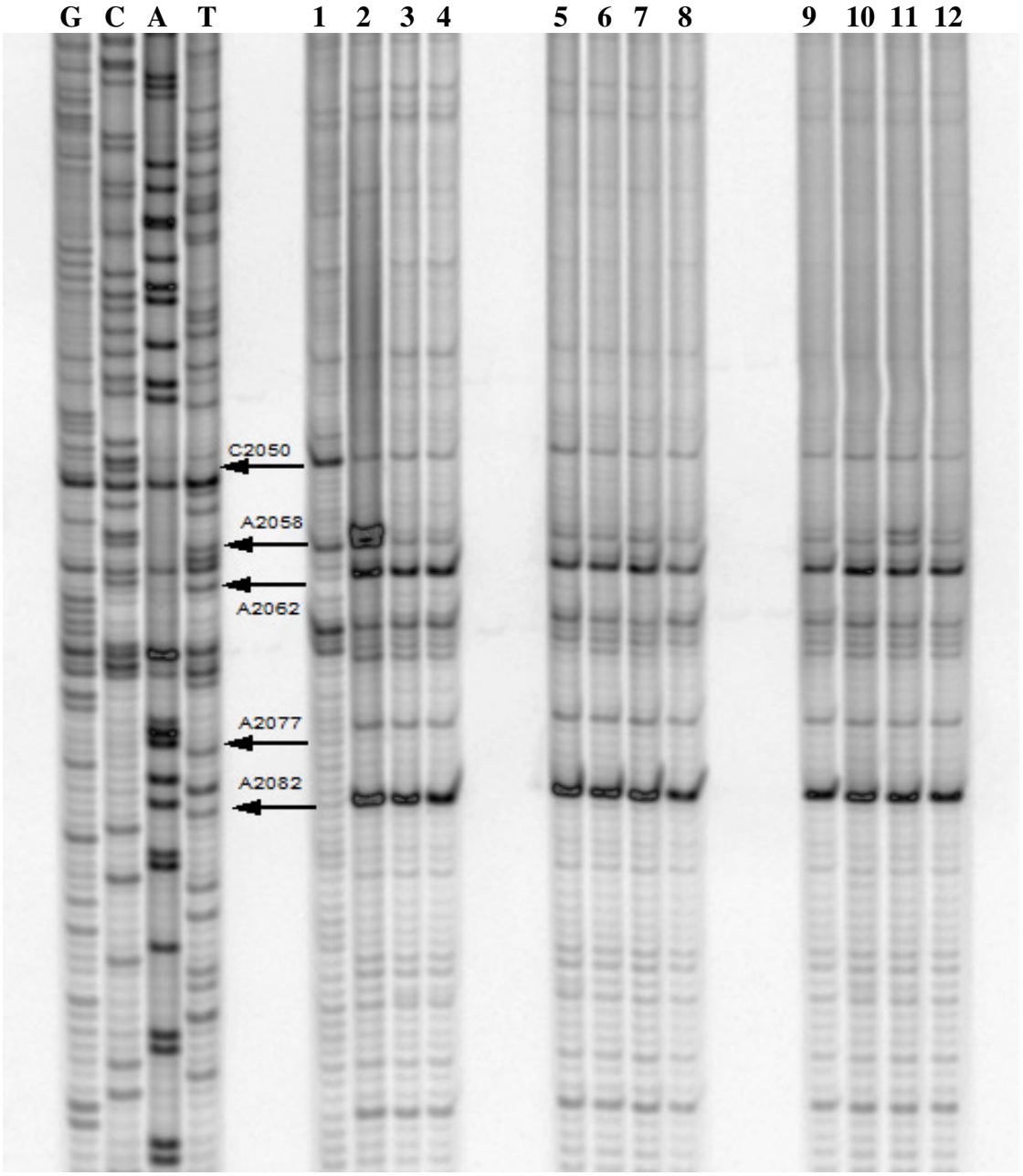

Figure 4.5 Footprinting of 23S rRNA with primer 2180. Dideoxy sequencing lanes G,C,A and T followed by lanes: 1) unmodified rRNA, 2) DMS modified 23S rRNA, 3-4) DMS modified 23S rRNA in presence of clarithromycin and azido-ketolide intermediate, respectively, Lanes 5-12) 23S rRNA DMS modified in the presence of 3C NLS, 4C NLS, 3C rNLS, 4C rNLS, 3C PLI, 4C PLI, 3C RGD, and 4C RGD, respectively.

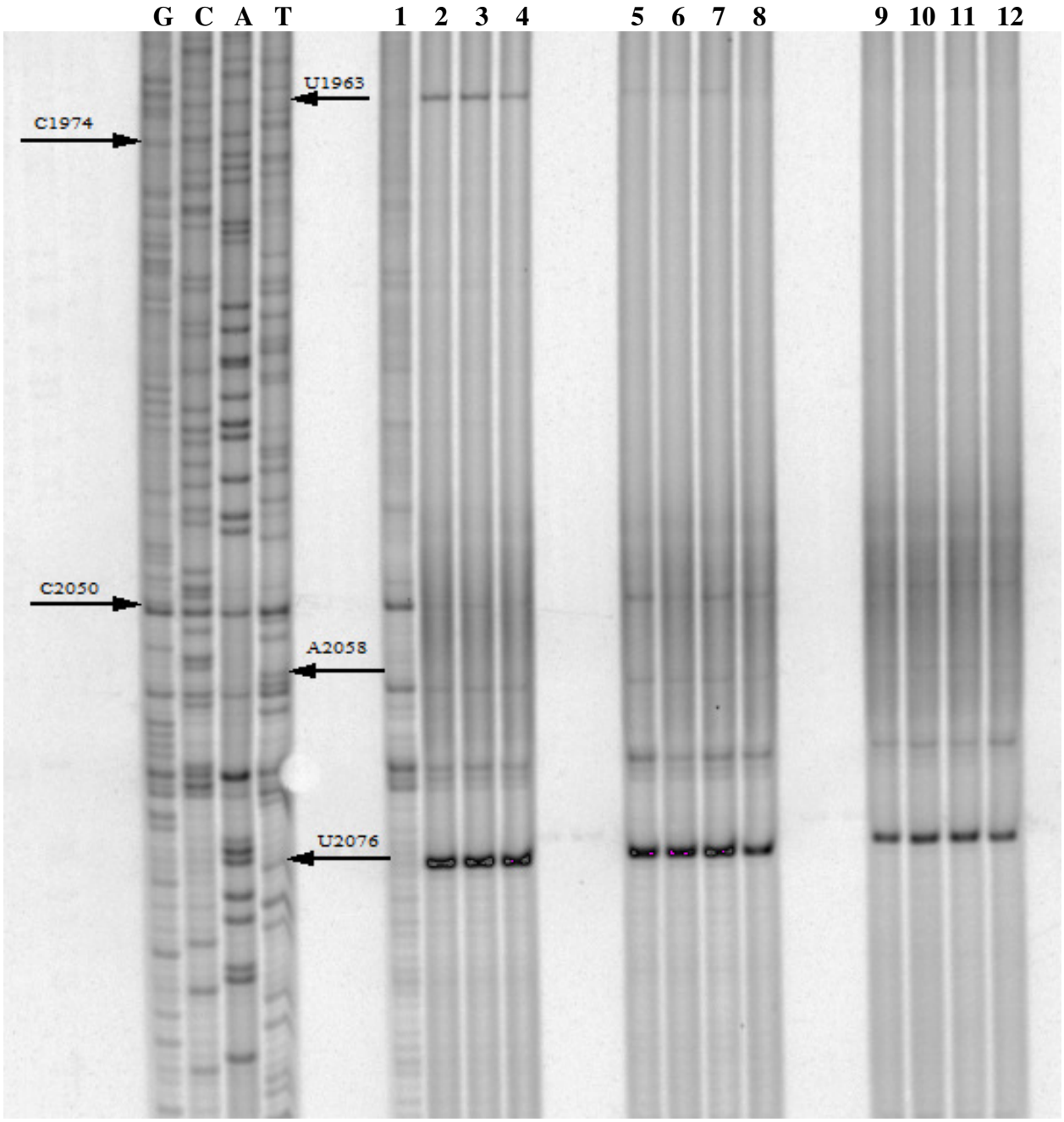

Figure 4.6 Footprinting of 23S rRNA with primer 2180. Dideoxy sequencing lanes G,C,A and T followed by lanes: 1) unmodified rRNA, 2) CMCT modified 23S rRNA, 3-4) CMCT modified 23S rRNA in presence of clarithromycin and azido-ketolide intermediate, respectively, Lanes 5-12) 23S rRNA CMCT modified in the presence of 3C NLS, 4C NLS, 3C rNLS, 4C rNLS, 3C PLI, 4C PLI, 3C RGD, and 4C RGD, respectively (performed by Arren Washington).

4.5 Discussion

As can be seen in Table 4.1, each of the peptolide probes retained some degree of prokaryotic translation inhibition. This data serves as an initial confirmation that the structural changes introduced did not completely diminish the probes' antibiotic properties. Several trends can also be seen in the prokaryotic IC_{50} values. Without exception the peptide tails alone did not cause inhibition, confirming that any inhibitory activity observed is from the conjugated peptolide probe. When comparing the NLS conjugate to the reverse, or rNLS conjugate, it can be seen that directionality of the peptide attachment does not seem to have much of an effect on the translation inhibition of the probe. However, the length of the linker does seem to play an important role in the inhibitory potential of each peptolide with the 4C molecules being more potent inhibitors in all cases except for rNLS.

The most striking difference in inhibition is evident when comparing the amino acid composition of the peptides. The overall charge of the residues comprising the peptides decreases in positive charge in the order NLS & rNLS (+5), PLI (+3), and RGD (zwitterionic). The potency of inhibition also follows this trend with the NLS conjugates being the strongest inhibitors and RGD being the weakest. This can be rationalized by considering the environment present in the exit tunnel. Being lined with almost exclusively rRNA, having a negatively charged backbone, the exit tunnel certainly provides an inviting negatively charged cavity for an electro positive peptide such as NLS to selectively nestle. This favorable charge interaction can also be used to explain the increase in potency seen when comparing the macrolide alone to the NLS peptolide .

The rabbit reticulocyte assay was initially done as a control experiment to confirm the retention of selectivity of the macrolide probes. Interestingly the PLI conjugates, and the PLI

peptide alone, showed some degree of eukaryotic inhibition. The erythromycin macrolide is a prokaryotic selective inhibitor of translation showing no activity in the rabbit reticulocyte assay. The PLI peptide alone showed slight inhibition with an IC_{50} of 205μM. When conjugated with the optimal linker length of 4C the conjugate of the macrolide and PLI peptide showed significant inhibition of eukaryotic translation with an IC_{50} of 38μM.

Footprinting of the 23S rRNA of *E. coli* was performed to further characterize the interaction of the peptolide probes with the ribosome. The modifying agents employed DMS and CMCT. DMS modifies the rRNA by methylating available adenosine and cytosine residues (16). Bases available to modification include those that are single stranded, base paired at the end of a helix, or adjacent to a GU wobble pair. Methylation occurs at the N1 of A and the N3 position of C. Similarly, CMCT modifies the N3 of U and N1 of G of any available bases (17). As the RT enzyme travels down the RNA creating a compliment DNA (cDNA) strand, it will stall at these sites of modification and yield truncated cDNA products. By modifying the rRNA in the absence and presence of the peptolide probes, any changes in availability of certain bases to DMS or CMCT modification can be used to indicate sites of drug interaction.

The footprinting gel in Figure 4.5 shows a clear peptolide footprint at residue A2058 of the *E. coli* 23S rRNA. Lane 1 is unmodified rRNA and lane 2 is DMS modified rRNA in the absence of probes. Any differences between lanes 1 and 2 highlight residues that are available for DMS modification. Similarly, any differences between lane 2 and lanes 3-12, lanes containing rRNA that is DMS modified after drug or probe binding, will highlight any sites that have changes in DMS availability. The bold band at A2058 in lane 2, and its greatly reduced intensity in the presence of all peptolide lanes, is clear evidence of a drug binding footprint. This is certainly an expected site of drug interaction, as A2058 is known to be directly adjacent to the

well-defined macrolide binding pocket of the ribosome as discussed in chapter 1 of this thesis. Thus, this footprinting results verifies that the binding target of the peptolide probes is indeed the same as the parent macrolide drug.

Another significant trend observed in Figure 4.5 can be seen in the A2058 band in the peptolide lanes. In almost all of the lanes the A2058 band is gone or barely visible. The exception to this is the darker A2058 band present in lane 11. This lane is the 23S rRNA DMS modified in the presence of the 3C RGD peptolide probe. The enhanced intensity of this band in copmparison to the other lanes is indicative of a decreased binding affinity of the 3C RGD peptolide for that footprinting site. The weaker the binding, the more accessible the residue is to DMS. Looking back to Table 4.1 it can be seen that the 3C RGD peptolide was in fact the worst performing probe with an IC_{50} value of 60 μM in the *E. coli* assay. This provides a direct correlation between our *in vitro* translation inhibition studies and our DMS footprinting results.

While the footprint observed in Figure 4.5 provided a verification of the macrolide portion of the probes finding themselves at home in the macrolide binding pocket, the CMCT footprint of Figure 4.6 reveals the residence of the peptide tail portion. Lanes 2-4 show a clear band corresponding to U1963. This residue is thus available to CMCT modification in the absence and presence of both clarithromycin and the azido-ketolide intermediate. In marked contrast, residue U1963 is totally protected from modification by CMCT in the presence of all peptolide probes as evidenced by the absence of this band in lanes 5-12 of Figure 4.6. Examining the crystal structure of a macrolide bound to the 50S subunit of the *E. coli* ribosome confirms that residue U1963 is indeed accessible from the macrolide binding pocket (Figure 4.7) (11).

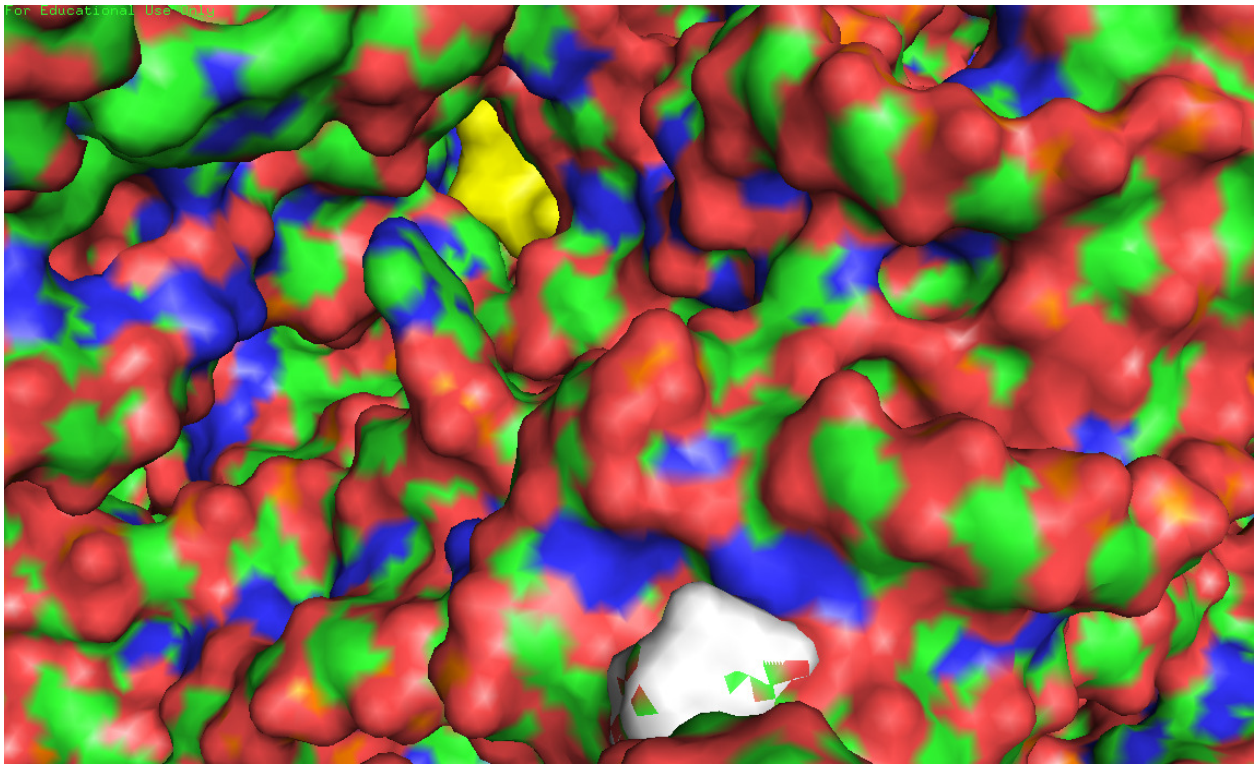

Figure 4.6 Crystal structure of erythromycin (yellow) bound to the 50S subunit of *E. coli*. This image is a complete spacefill of the entire large ribosomal subunit. U1963 (white) lies on the surface of the 50S subunit, at the 30S interface, and is reachable by the peptolide tail through an opening in the 50S directly adjacent to the macrolide binding pocket.

To conclude, we rationally designed, synthesized and validated the nucleic acid binding target of a novel class of macrolide-peptide conjugate probes known as peptolides. These peptolides are intended to bind in the exit tunnel of the ribosome and provide insight as to the nature of the exit tunnel environment. It was demonstrated that all peptolides created retained some degree of the antibacterial property inherent in the parent macrocyclic molecule. *In vitro* results showed that the size and direction of attachment of the peptide tails did not have much influence on the overall translation inhibition ability of the probes. Contrastingly, the overall charge of the peptide tail proved to have the greatest influence on inhibitory IC_{50} values with the most positively charged peptide, NLS, proving to be the most potent. Additionally, DMS footprinting of the 23S rRNA of the *E. coli* ribosome showed that the peptolide probes retained the interaction mode of the parent molecule by binding to the macrolide binding pocket in the exit tunnel. The location of the peptide tails of the peptolides was also deduced via CMCT footprinting and showed a binding position in the direct vicinity of residue U1963.

The unique peptide tail binding in the direct area of the PTC and subunit interface of the prokaryotic ribosome, coupled with potent translational inhibition *in vitro* could certainly make the peptolide family of probes a viable, novel antibiotic class of drugs. By almost doubling the size of the binding pocket, the novel peptolides compounds may be able to still bind to the ribosome despite mutations that typically lead to resistance. For example, the methylation of A2058 confers macrolide resistance to *E. coli*; by sampling an entirely new portion of the ribosome with its tail portion, a peptolide may still bind tightly even with the additional methyl group in the macrolide binding pocket. Furthermore, as a result of the observation of this thesis work that some peptolides also posses eukaryotic translation inhibition capabilities, they could prove to be useful in preventing the growth of rapidly proliferating eukaryotic cells such as

plasmodium, leishmania, or tumor cells. Additionally, different head groups could be utilized in creating new peptolides; for example, an oxazolidinone antibiotic could be employed to sample a different binding area of the ribosome.

Some of the work presented in this chapter was done in collaboration with Arren Washington. Mr. Washington will continue the analysis of the peptolides presented here, and other novel peptolides, in his future thesis work.

4.6 References

1) Wimberly BT, Brodersen DE, Clemons WM Jr, Morgan-Warren RJ, Carter AP, Vonrhein C, Hartsch T, Ramakrishnan V. (2000) Structure of the 30S ribosomal subunit. *Nature*. **407**, 327-39.
2) Ban N, Nissen P, Hansen J, Moore PB, Steitz TA. (2000) The complete atomic structure of the large ribosomal subunit at 2.4 A resolution. *Science*. **289**, 905-20.
3) Nissen P, Hansen J, Ban N, Moore PB, Steitz TA. (2000) The structural basis of ribosome activity in peptide bond synthesis. *Science*. 289, 920-30.
4) Schluenzen F, Tocilj A, Zarivach R, Harms J, Gluehmann M, Janell D, Bashan A, Bartels H, Agmon I, Franceschi F, Yonath A. (2000) Structure of functionally activated small ribosomal subunit at 3.3 angstroms resolution. *Cell*. **102**, 615-23.
5) Voss NR, Gerstein M, Steitz TA, Moore PB. (2006) The geometry of the ribosomal polypeptide exit tunnel. *J Mol Biol*. **360**, 893-906.
6) Jenni S, Ban N. (2003) The chemistry of protein synthesis and voyage through the ribosomal tunnel. *Curr Opin Struct Biol*. **13**, 212-9.
7) Voss C, Eyol E, Frank M, von der Lieth CW, Berger MR. (2006) Identification and characterization of riproximin, a new type II ribosome-inactivating protein with antineoplastic activity from Ximenia americana. *FASEB J*. **20**, 1194-6.
8) Wilson DN, Beckmann R. (2011) The ribosomal tunnel as a functional environment for nascent polypeptide folding and translational stalling. *Curr Opin Struct Biol*. **21**, 274-82.
9) Ito K, Chiba S, Pogliano K. (2010) Divergent stalling sequences sense and control cellular physiology. *Biochem Biophys Res Commun*. **393**, 1-5.

10) Kannan K, Mankin AS. (2011) Macrolide antibiotics in the ribosome exit tunnel: species-specific binding and action. *Ann N Y Acad Sci*. **1241**, 33-47.

11) Dunkle JA, Xiong L, Mankin AS, Cate JH. (2011) Structures of the Escherichia coli ribosome with antibiotics bound near the peptidyl transferase center explain spectra of drug action. *Proc Natl Acad Sci U S A*. **107**, 17152-7.

12) Pratt SD, David CA, Black-Schaefer C, Dandliker PJ, Xuei X, Warrior U, Burns DJ, Zhong P, Cao Z, Saiki AY, Lerner CG, Chovan LE, Soni NB, Nilius AM, Wagenaar FL, Merta PJ, Traphagen LM, Beutel BA. (2004) A strategy for discovery of novel broad-spectrum antibacterials using a high-throughput Streptococcus pneumoniae transcription/translation screen. *J Biomol Screen*. **9**, 3-11.

13) Thorne, C.A., Lafleur, B., Lewis, M., Hanson, A.J., Jernigan, K.K., Weaver, D.C., Huppert, K.A., Chen, T.W., Wichaidit, C., Cselenyi, C.S., Tahinci, E., Meyers, K.C., Waskow, E., Orton, D., Salic, A., Lee, L.A., Robbins, D.J., Huppert, S.S. and Lee, E. (2011) A biochemical screen for identification of small-molecule regulators of the wnt pathway using Xenopus egg extracts. *J. Biomol. Scr.* **16**, 995–1006.

14) Merryman, C., & H. F. Noller. (1998). Footprinting and modification-interference analysis of binding sites on RNA, p. 237-253. In C. W. J. Smith (ed.), RNA:protein interactions, a practical approach. Oxford University Press, Oxford, United Kingdom.

15) Amit M, Berisio R, Baram D, Harms J, Bashan A, Yonath A. (2005) A crevice adjoining the ribosome tunnel: hints for cotranslational folding. *FEBS Lett*. **579**, 3207-13.

16) Tijerina P, Mohr S, Russell R. (2010) DMS footprinting of structured RNAs and RNA-protein complexes. *Nat Protoc*. **2**, 2608-23.

17) Shaw LC, Lewin AS. (1995) Protein-induced folding of a group I intron in cytochrome b pre-mRNA. *J Biol Chem*. **270**, 21552-62.

CHAPTER 5: CHARACTERIZATION OF NOVEL TOPOISOMERASE II / HISTONE DEACETYLASE INHIBITOR CONJUGATES: NUCLEIC ACID BINDING PROPERIES

Part of this work was published by William Guerrant, Vishal Patil, Joshua Canzoneri, and Adegboyega K. Oyelere in the Journal of Medicinal Chemistry2012 (55), 1465-1477. Sections 5.1-5.7 represent a portion of said published manuscript, and are presented here unchanged. Sections 5.8and 5.9 present and discuss additional work done by Joshua Canzoneri and Junpeng Xu after publication of the said manuscript.

5.1 Introduction

Strategies to ameliorate the flaws of current chemotherapeutic agents, while maintaining potent anticancer activity, are of particular interest. Agents which can modulate multiple targets may have superior utility and fewer side effects than current single-target drugs. To explore the prospect in cancer therapy of a bivalent agent that combines two complimentary chemo-active groups within a single molecular architecture; we have synthesized dual-acting histone deacetylase and topoisomerase II inhibitors. These dual-acting agents are derived from suberoylanilide hydroxamic acid (SAHA) and anthracycline daunorubicin; prototypical histone deacetylase (HDAC) and topoisomerase II (Topo II) inhibitors respectively. We report herein that these agents present the signatures of inhibition of HDAC and Topo II in both cell-free and whole cell assays. Moreover, these agents potently inhibit the proliferation of representative cancer cell lines. Additionally, the ability of these novel compounds to bind to DNA and RNA hairpin targets was investigated, highlighting a preference for the compounds to ding to DNA but not to RNA.

5.2 Rational Design of TopoII / HDACi Conjugates

Several rational pharmacological strategies, including vaccination, gene therapy, immunotherapy, and new target identification and validation, have emerged for the treatment of metastatic diseases. Despite these progresses, chemotherapy remains the primary treatment of choice for most cancer cases. However, almost all chemotherapeutic agents suffer from severe toxicities and other undesirable side-effects. To address these problems, the cancer medicine of the future will incorporate, within a single molecule, elements that allow for simultaneous targeting of multiple cancer-fighting targets while maintaining lower side effects (1-3). This realization has continued to spawn immense efforts in the literature. Studies aimed at identifying multivalent ligands as promising pharmacological tools, that may be more efficacious for various human diseases than highly selective single-target drugs, are ongoing in several academic and pharmaceutical labs (4-7). A subset of these studies has revealed that balanced modulation of a small number of targets may have superior efficacy and fewer side effects than single-target treatments (1,7,8).

Epigenetic control has become widely accepted as a mechanism for cell regulation (9-11). Specifically, histone deacetylase (HDAC) is a class of epigenetic enzymes that has generated much interest in cancer therapeutics literature. HDACs are known to associate with many oncogenes and tumor suppressors, leading to altered expression patterns, and have consequently become attractive targets for small-molecule inhibition (12,13). Histone deacetylase inhibitors (HDACi) have been shown to cause growth arrest, differentiation, and apoptosis in tumor cells and in animal models by inducing histone hyperacetylation and $p21^{waf1}$ expression (14-17). Additionally, modulation of activities of HDACs alters the activity of a

diverse range of proteins, many of which are attractive therapeutic targets themselves, including p53, E2F, tubulin, and Hsp90 (18-22). HDAC inhibition has been clinically validated as a therapeutic strategy for cancer treatment with the FDA approvals of suberoylanilide hydroxamic acid (SAHA) and romidepsin (FK-228) for treatment of cutaneous T cell lymphoma (23-25). However, a large number of the currently known HDACi have elicited only limited *in vivo* antitumor activities and have not progressed beyond preclinical characterizations (26-28). HDACi that modulate the functions of additional intracellular targets, other than the various HDAC isoforms, may be able to ameliorate many of the shortcomings of current inhibitors.

Due to the presence of large hydrophobic patches at the HDAC surface rim it is conceivable that appropriate conjugation of the surface recognition group of a prototypical HDACi to other hydrophobic anti-tumor pharmacophores could furnish a new class of bifunctional agents (29,30). To date, there exist a few examples of this subtype of bifunctional HDACi derived compounds (31-33). Expansion of the repertoire of such bifunctional compounds could lead to broad acting, therapeutically viable anti-cancer agents.

An attractive starting point for a secondary target is the topoisomerase class of enzymes (Topo I and Topo II), which are validated targets for many small molecule inhibitors including clinically useful anthracyclines such as doxorubicin (DOX) and daunomycin (DAU) (Figure 5.1); and camptothecins such as irinotecan and topotecan (34). Topo inhibitors elicit anticancer activities primarily by stabilizing the DNA-enzyme cleavable complex through intercalation between DNA base pairs. However, DNA does not exist as a naked structure in the nucleus. It is non-covalently associated with histones to form the nucleosomes which make up chromatin subunits. Agents, such as HDACi, that induce hyperacetylation of histone proteins complexed with DNA could increase the accessibility of DNA within chromatin and consequently potentiate

the anticancer activities of Topo inhibitors (35-36). Moreover, recent observations have shown that HDAC1, HDAC2 and Topo II co-localize *in vivo* as part of functionally coupled complexes (37-38). This evidence suggests simultaneous Topo and HDAC inhibition could be a viable alternative approach in cancer therapy.

Anthracyclines are one of the most thoroughly studied classes of anticancer agents with copious structure activity relationship (SAR) data to aid the design and characterization of new anthracycline-containing compounds (39-44).

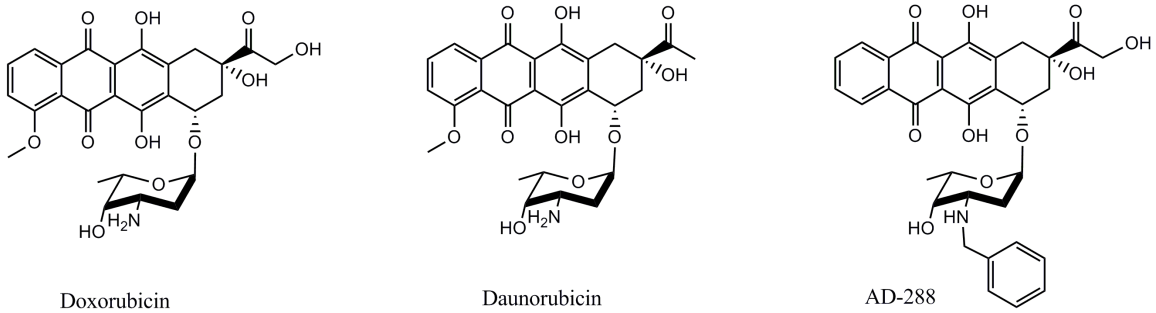

Figure 5.1 Representative structures of anthracycline antibiotics.

Specifically, N-benzylated anthracyclines, such as N-benzyl doxorubicin (AD-288) (Figure 5.1) (42), have enhanced Topo II inhibitory activities, reduced cardiotoxicity activity, and reduced susceptibility to the Pgp-mediated multidrug resistance (45-47). We postulated that introduction of the HDACi via N-benzylation of the DAU amino group would be compatible with Topo II inhibition and possibly engender the positive attributes of N-benzylated anthracyclines to the resulting conjugates. In turn, the anthracycline moiety could serve two other purposes: i) as a surface recognition cap group, allowing favorable orientation of hydroxamic acid within the zinc binding pocket of HDAC, and ii) as a delivery vehicle, since the transport of the anthracycline via proteasome could facilitate nuclear accumulation of HDACi (43). Based on the forgoing, we designed two classes of conjugates - a direct DAU-SAHA conjugate and DAU-triazolylaryl

hydroxamate conjugates (Figure 2). The later conjugates were inspired by our previous studies which revealed that triazole moiety could be incorporated in lieu of amide bond as a surface recognition connecting group in prototypical HDACi (48). A total of 5 unique topoII / HDAC inhibitor conjugates were synthesized by Dr. Vishal Patil (Scheme 5.1 and Scheme 5.2).

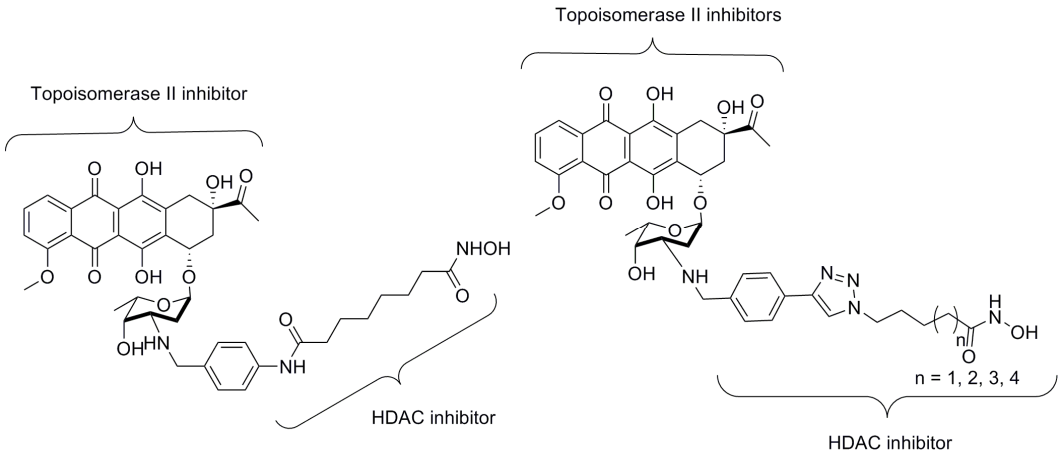

Figure 5.2 Design of dual-acting Topo II-HDAC inhibitors.

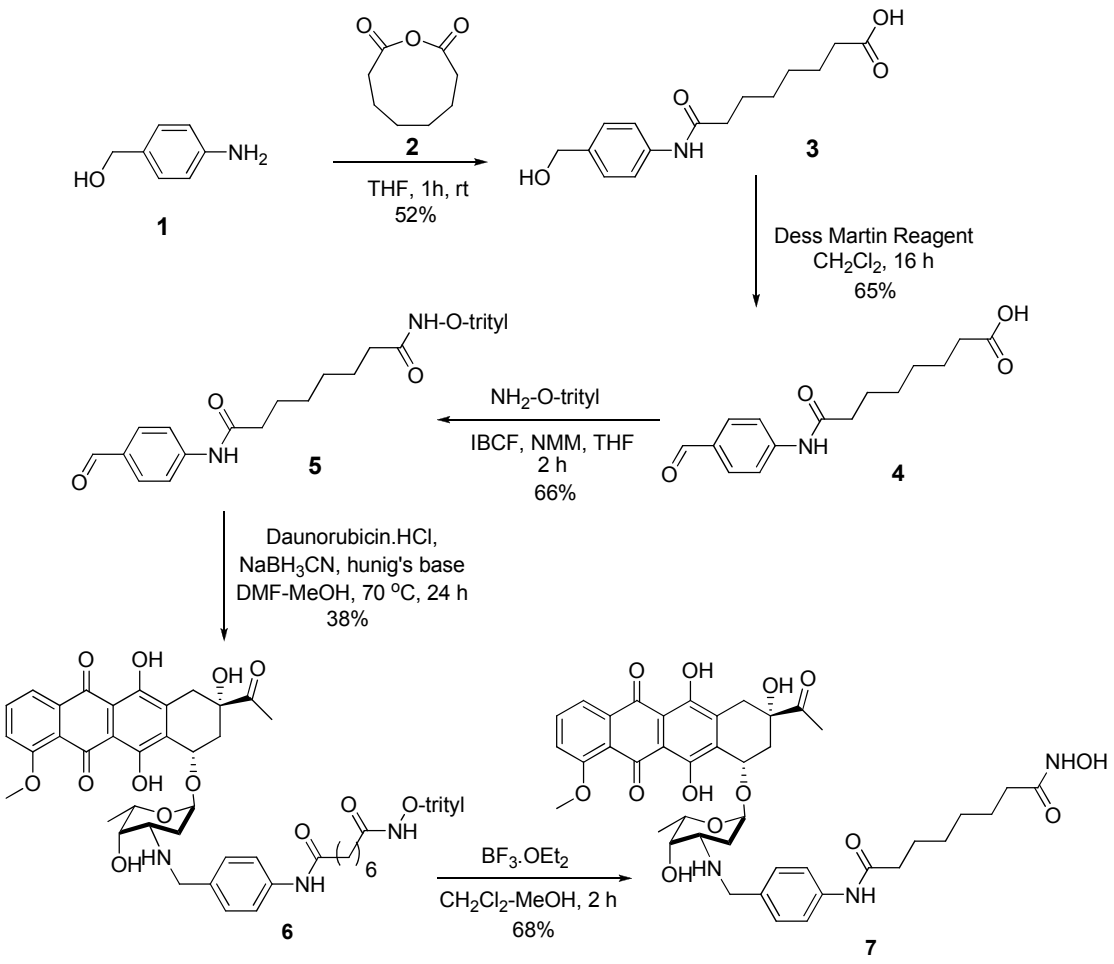

Scheme 5.1 Synthesis of the SAHA-based dual-acting Topo II-HDAC inhibitor.

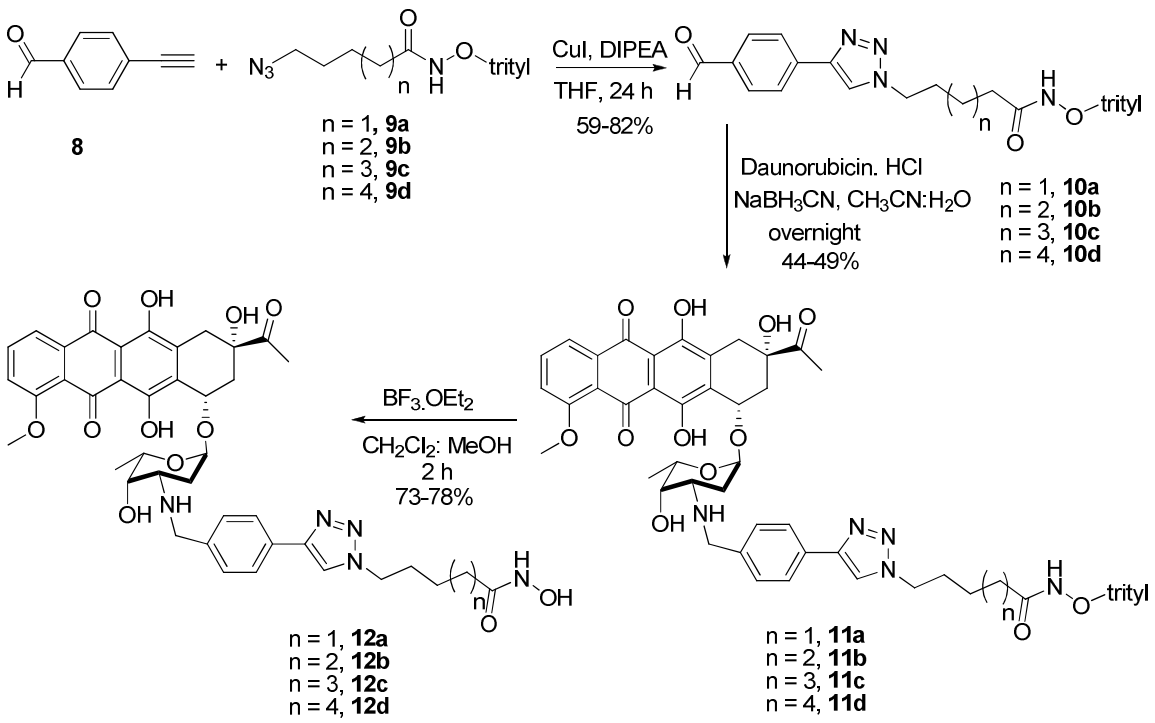

Scheme 5.2 Synthesis of the SAHA-like, triazole-based Topo II-HDACi.

5.3 *In vitro* HDAC Inhibition

We first tested the HDAC inhibition activity of compounds **7** and **12a-d** against crude HeLa cell nuclear extract HDACs using a cell free assay (*Fluor de Lys*) as previously described (48). Overall, these compounds showed inhibition activities against HeLa cell nuclear extract HDACs which are comparable to or exceed that of the standard SAHA (Table 5.1). It is particularly interesting that **7** has identical anti-HDAC activity to SAHA. This result suggests that the attachment of DAU does not impair the interaction between the HDACi component of the conjugate and the HDAC enzyme outer surface residues. It is also conceivable that the conjugate may adopt a conformation whereby the anthracycline moiety can contribute positively to the interaction with the crucial active site or surface residues. All triazole-linked conjugates potently inhibit HeLa cell nuclear extract HDACs with IC_{50} in the low to mid-nanomolar range. Among these conjugates, **12a** is the least active, closely followed by **12d** which is about 20-fold more potent. Compounds **12b** and **12c** have the most potent anti-HDAC activity, with a slight preference for the six methylene-linked **12c**. Interestingly, the triazole-linked compound **12b** is 40-fold more potent than the amide-linked **7**, despite their similar linker length. Relative to the standard SAHA, **12c,** the most potent compound in this series, is 70-fold more potent (Table 5.1). The foregoing results showed that these conjugates followed a trend similar to that which we noted for the previously reported, structurally unrelated, triazole-based HDACi (48).

To obtain evidence for the HDAC isoform selectivity, we tested these dual acting Topo II –HDACi conjugates against selected recombinant HDACs – HDAC 1, HDAC 6 and HDAC 8. The pattern of the anti-HDAC activities of these compounds against HDAC 1 and HDAC 6 is similar to what we observed for the HeLa cell nuclear extract HDACs with few exceptions.

Specifically, compounds **7** and **12b** have indistinguishable activity against HDAC 1 and HDAC 6 (Table 5.1). Additionally, **12a** which has mid-nanomolar IC_{50} against HeLa cell nuclear extract HDACs is almost inactive against HDAC 1 (IC_{50} = 4.6 μM) while it maintains decent activity against HDAC 6 (IC_{50} = 0.6 μM). We are not exactly sure of the cause of this disparity. In general, these compounds are weaker inhibitors of HDAC 8 with the exception of **7**, whose anti-HDAC 8 activity is only about 4-fold less than its anti-HDAC 1 activity (Table 5.1). These data suggest that **7** is a more indiscriminate inhibitor of these sets of HDACs while the rest of the conjugates are more selective.

Table 5.1 *In vitro* HDAC Inhibition.

Compound	n	HDAC 1/2 IC_{50} (nM) [a]	HDAC 1 IC_{50} (nM) [b]	HDAC 6 IC_{50} (nM) [b]	HDAC 8 IC_{50} (nM) [b]
SAHA	**-**	65.0	38± 2	27± 2	1989± 156
DAU	**-**	N.D.	N.T.	N.T.	N.T.
7	**-**	64.7	47± 3	20± 1	220±21
12a	**1**	89.9	4,600± 240	555± 36	N.D.
12b	**2**	1.6	54± 3	30± 2	4,129±421
12c	**3**	0.9	8± 0.4	20± 0.4	710± 43
12d	**4**	4.2	11± 0.4	19± 1	379±37

[a]Inhibition was assayed using the Biomol HDAC Fluorimetric Assay/Drug Discovery Kit.
[b]Data obtained through contract arrangement with BPS Bioscience (San Diego, USA; www.bpsbioscience.com).

5.4 *In vitro* Topoisomerase II Decatenation

We performed a cell-free DNA decatenation assay to determine the Topo II inhibition activity of these Topo II-HDACi conjugates. We used kinetoplast DNA (KDNA), a catenated network of mitochondrial DNA seen in trypanosomes, to quantify the conjugates' Topo II inhibition activity according to a literature protocol (49-50). The substrate KDNA (200ng) and 50μM drug were combined in assay buffer (50 mM Tris–HCl, pH 8, 120 mM KCl, 10 mM $MgCl_2$, 0.5 mM ATP, 0.5 mM dithiothreitol, 300ug/ml bovine serum albumin (BSA)) and incubated for 10 min on ice. Next, 1 U of topoisomerase II was added and the reaction was allowed to proceed for 10 min at 37°C. The reaction was quenched via the addition of loading buffer (1% sarkosyl, 0.025% bromophenol blue, and 5% glycerol), and was then analyzed by electrophoresis on a 1% agarose gel in TBE buffer (89 mM Tris, 89 mM borate, and 2 mM Na–EDTA, pH 8.3) for 3.5 h at 40 V. The gel was stained with SYBR Green I (Molecular Probes) for 30 min and was visualized under UV illumination and photographed on an AlphaImager.

Figure 5.4 illustrates the results obtained from this study. KDNA and decatenated KDNA marker (lanes 1 and 2 respectively) were used as controls. Treatment of KDNA with Topo II within 10 min at 37°C resulted in an extensive DNA decatenation (lane 3). As expected, addition of 50 μM DAU to the decatenation experiment resulted in a severe impairment of DNA decatenation (comparing lanes 3 and 4). Relative to DAU, **12a** and **12d** have lower Topo II inhibition activity, with the worst overall inhibition shown by **12a**, the conjugate with a four methylene linker (lanes 7 and 8). Conjugates **12b** and **7** inhibited Topo II activity at comparable levels to that of DAU at the same drug concentration (lanes 6 and 9, respectively). However, compound **12c** had an enhanced Topo II inhibition activity relative to DAU, resulting in a near

total inhibition at 50 μM (comparing lanes 4 and 5). These results show that the Topo II inhibition activity of DAU is tolerant of an appropriate attachment of HDACi groups and, as in the case of **12c**, such groups could further enhance Topo II inhibition activities of anthracycline derivatives. The molecular basis of the HDACi linker length-dependent enhancement of Topo II inhibition of these dual-acting conjugates isn't entirely clear. It is plausible that the placement of the HDACi group of these conjugates within DNA minor grooves, through the daunosamine sugar could further promote drug-DNA association, thereby enhancing the stability of the biologically relevant drug-DNA-Topo II ternary complex (51).

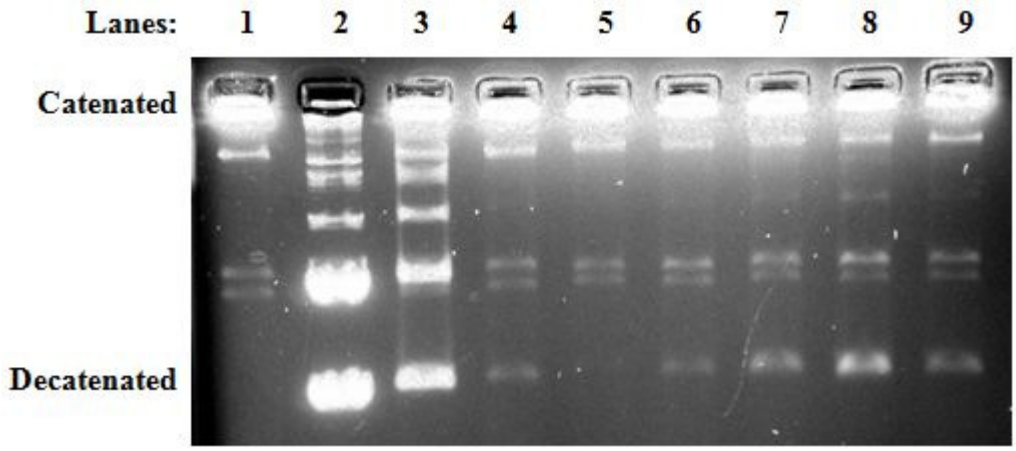

Figure 5.4 Topoisomerase II Decatenation Assay. Lanes 1-3: (1) KDNA, (2) decatenated KDNA marker, (3) KDNA and Topo II. Lanes 4-9: KDNA, Topo II, and 50μM (4) **DAU**, (5) **12c**, (6) **12b**, (7) **12d**, (8) **12a**, (9) **7.**

5.5 *In Vitro* Cell Growth Inhibition

Cell viability experiments were performed to probe for the prospect of biological activity of these compounds in the cellular milieu. DU-145 prostate carcinoma and SK-MES-1 non-small cell lung carcinoma was obtained from ATCC and maintained in the recommended growth mediums. MCF-7 breast cancer cells were a generous gift from Dr. Donald Doyle. All cell lines were maintained in a 37°C incubator with a 5% CO_2 environment. All compounds to be tested were dissolved to a concentration of 10 mM in DMSO and stored at -80°C. Cells were passaged 24 h prior to cell viability experiments. For cancer cell viability experiments, cells were dosed for 72 h and viability was determined both by Trypan Blue staining and through the use of the MTS assay (Promega) according to manufacturer's instructions. Control wells were dosed with fresh media containing 0.1% DMSO.

Three human cancer cell lines were used to quantify IC_{50} values for these compounds. Table 2 shows the IC_{50} values of each compound for all cancer cell types studied. The positive control compounds DAU and SAHA inhibit the proliferation of these tumor cell lines with IC_{50} similar to the values in the literature (52-53). DAU displays cell line dependent cytotoxicity that varies by as much as 10-fold among these three cell lines while SAHA shows no such cell line dependent effect (Table 5.2). Bifunctional compounds **12a-d** show linker length dependent anti-proliferative activities that closely matched their anti-HDAC activities. Among the three transformed cell lines investigated, these compounds decreased the viability of DU-145 the most, while they are least cytotoxicity against MCF-7. Although less pronounced than that seen with DAU, these compounds display cell line-dependent cytotoxicity as well. Nevertheless, the micromolar IC_{50} values and the traction with anti-HDAC activities suggest that HDAC inhibition

is the dominating mode of antiproliferative activities of compounds **12a-d**. Specifically, the anti-proliferative activities of **12c** and SAHA, compounds with similar linker length, are virtually indistinguishable against DU-145 and SK-MES-1 cell lines. This finding is surprising since **12c** displays the most potent HDAC and Topo II inhibition activities. Interestingly, compound **7**, a true hybrid between SAHA and DAU, showed the best cytotoxicity of all the bifunctional compounds across all cell lines, possessing sub-micromolar activities. In fact, the cytotoxicity of **7** closely rivals that of DAU, and they are equipotent against MCF-7. This is contrary to the trend seen in the cell-free assays. The potentiation of the activity of **7** within the cellular environment could be due to many factors, including the predominance of the Topo II inhibition character in dictating the bioactivity of **7**, the indiscriminate inhibition of multiple HDAC isoforms, or an alternative mechanism(s) that is unrelated to the inhibition of the activities of either target.

Table 5.2 Cell Viability Assay.[a]Values are the average of two experiments performed in triplicate. IC_{50} values were determined using the MTS assay (Promega). Performed by Dr. William Guerrant.

compd	*n*	DU-145 IC_{50} (μM)[a]	SK-MES-1 IC_{50} (μM)[a]	MCF-7 IC_{50} (μM)[a]
7		0.13 ± 0.06	0.47 ± 0.02	0.99 ± 0.21
12a	1	5.39 ± 1.02	15.3 ± 3.1	24.5 ± 1.6
12b	2	1.61 ± 0.29	4.68 ± 0.75	13.4 ± 1.85
12c	3	2.92 ± 0.31	3.31 ± 0.23	10.6 ± 0.94
12d	4	2.06 ± 0.33	2.61 ± 0.11	14.8 ± 1.6
DAU		0.09 ± 0.002	0.17 ± 0.09	0.95 ± 0.05
SAHA		2.12 ± 0.25	2.42 ± 0.38	2.50 ± 0.61

5.6 Intracellular Topoisomerase II Inhibition

To obtain information about the intracellular fate of Topo II upon cell exposure to these dual-acting agents, we used an immunoblotting kit to assay compound-induced Topo II inhibition in an intracellular environment (Figure 5.5) (54). DU-145 cells were dosed with drug concentrations corresponding to cell growth inhibition IC_{50}'s while the control cells were dosed with vehicle (0.1% DMSO). The relative levels of stabilized Topo II-DNA cleavage complexes were determined for a 30 min drug treatment, as described by the manufacturer. Within this period, the control cells showed no significant amounts of Topo II inhibition, evidenced by the low levels of Topo II associated DNA (Figure 7a, lane 1). Cells treated with DAU and **12b** contained high levels of Topo II – DNA cleavage complexes, with **12b** showing a significantly higher amount (Figure 7a - lanes 2 and 4, respectively). This result suggests that **12b** could derive its cytotoxic activity, in part, from intracellular Topo II inhibition. Conversely, the levels of Topo II – DNA cleavage complexes in cells exposed to **7** is indistinguishable from that of the control cells (Figure 7, lane 3), suggesting a minimal contribution of Topo II inhibition to the cytotoxic activity of **7** within this period.

To elucidate any contribution Topo II inhibition could be adding to long-term inhibition of cell proliferation, Topo II cleavage complexes were assayed after 72 hours of treatment with compounds (Figure 7b). DU-145 cells were probed for Topo II inhibition with an *in vitro* blotting kit designed to show relative amounts of stabilized Topo II-DNA cleavage complexes (Topoisomerase II *In Vivo* Link Kit, Topogen). Briefly, cells were dosed with Topo II-HDACi's at concentrations pertaining to their respective IC_{50} values for cell viability inhibition. Control cells were dosed with 0.1% DMSO to take into account DMSO from stock solutions of drug. As

recommended in the protocol instructions, cells were dosed for 30 minutes, counted, and lysed with 1% sarkosyl. Alternately, DU-145 cells were dosed for 72 hours, counted, and equalized with the cell count from the 30 min incubation before subsequent lysis. Lysate was collected, loaded on a CsCl gradient, and subjected to centrifugation at 31,000 RPM at room temperature for 12 hours. Aliquots of the gradient separations were then taken and the Topo II-DNA cleavage complexes were identified via absorbance at 260 nm. Aliquots were then loaded into a slot blotting device and subjected to vacuum to load proteins onto a nitrocellulose membrane. Immunoblotting using the Odyssey Imaging System (LiCor Biosciences) revealed Topo II levels associated with the stabilized DNA complexes.

As expected, DAU treatment results in significant inhibition of Topo II activity relative to control levels (Figure 5.5b, comparing lanes 1 and 2). Compound **7** shows a measured increase in Topo II inhibition relative to control levels (Figure 7b, comparing lanes 1 and 3). Interestingly, we observed a drastic drop in the levels of stabilized Topo II-DNA cleavage complexes upon cell exposure to **12b** for 72-hour (comparing lane 4 of Figures 5.5a and 5.5b). This result suggests that the Topo II inhibition activity of **7** increases with time while that of **12** decreases. The persistence of the stabilized Topo II-DNA cleavage complexes over a longer period indicates that Topo II inhibition may contribute significantly to the mechanism of the antiproliferative activity of **7**.

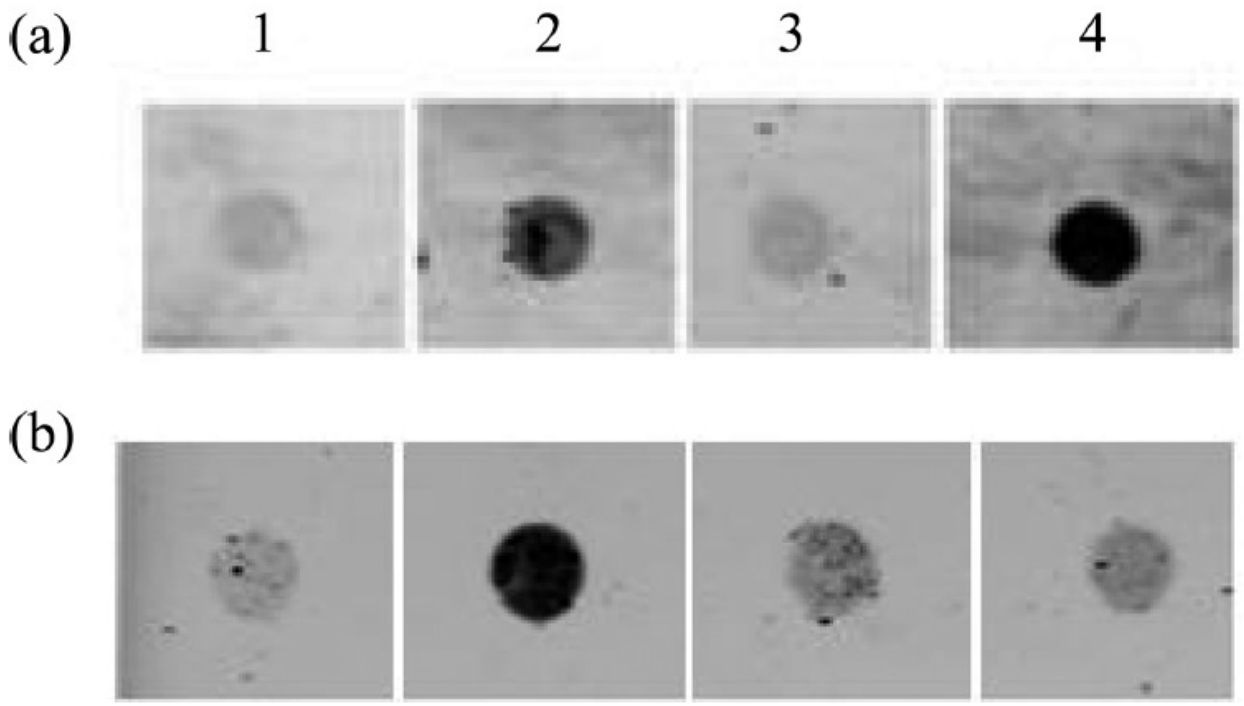

Figure 5.5 Intracellular Topo II Inhibition. DU-145 cells were probed for stabilized DNA-Topo II cleavage complexes upon (a) 30 min treatment; (b) 72 hour treatment with bifunctional compounds: (1) Control, (2) 90 nM **DAU**, (3) 130 nM **7**, (4) 1.6 μM **12b**. Performed by Dr. William Guerrant.

5.7 Cellular Localization

HDAC1 and Topo II, are cell nucleus-localized targets of these bifunctional compounds, while HDAC6 is cytoplasmic. To probe if cell penetration issues could be one of the alternative reasons for the difference in the potencies of compounds **7** and **12b**, we used confocal microscopy to visualize their intracellular localization (Figure 8). Cells were plated on glass coverslips in 35mm dishes 24 h before the experiment. They were then incubated with fresh media containing the indicated compounds at concentration of 1 μM. After 4 hours, cells were washed with PBS Cover slips were then mounted and viewed under a confocal microscope (DAU λ_{ex} = 488nm,; Zeiss LSM 510 UV confocal microscope). We exposed DU-145 cells to 1 μM of DAU, **7** and **12b**. After 4 hours incubation time, cells were monitored at 488nm, the excitation wavelength (λ_{ex}) of DAU, and we observed clear differences in the intracellular distribution profiles of the tested compounds. In agreement with previous study in the literature, DAU is localized within the nuclear and perinuclear regions of DU-145 cells (55). Although it shows a less nuclear localization, compound **7** is more widely distributed within the cytosol with evidence for perinuclear localization in similar to that of DAU. In contrast, **12b** shows a highly diminished intracellular distribution with the bulk of the compound trapped in vesicle-like bodies within the cell (Figure 5.6). The relatively poor intracellular distribution of **12b** could be due to low cell membrane penetration or an enhanced pump-induced efflux of compound from within the cell (56). We obtained a similar result with a lung tumor derived A549 cells (supporting information Figure S1). These results show that **7** and **12b** have different intracellular residency which may affect access to their targets and consequently offer additional insight into underlying factors that could contribute to the disparity in the *in vitro* potency of these compounds.

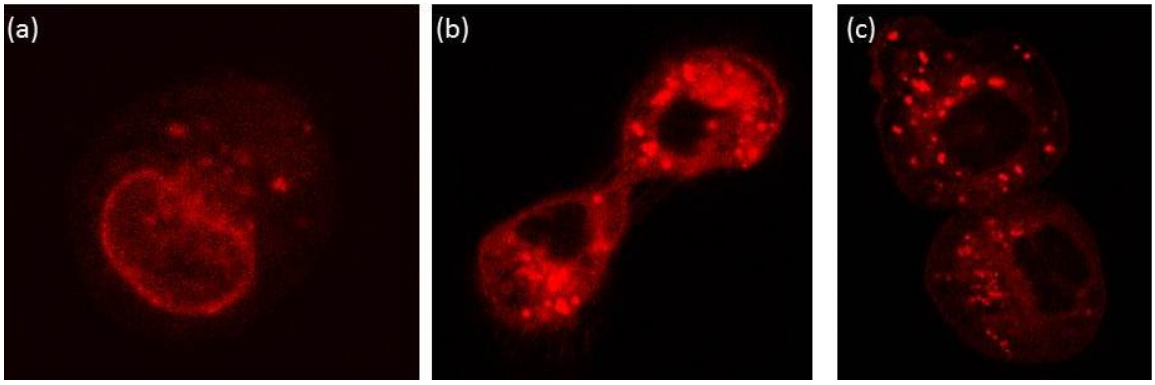

Figure 5.6 Cellular Localization of Dual-Acting Inhibitors. (a) **DAU**, (b) **7**, (c) **12b**. DU-145 cells were dosed at 1μM for 4 hours with indicated compounds and visualized by confocal microscopy.

5.8 Interaction of Topo II/HDAC Inhibitor Conjugates with DNA and RNA

In an attempt to better understand the results of the *in vitro* and *in vivo* experiments detailed above, it was next investigated how the changes to the classic anthracycline pharmacophore in the conjugate TopoII/HDACi molecules altered their ability to bind to nucleic acid targets. A 32-mer RNA and DNA hairpin construct of the same sequence 5`-GCUCUCUGCGAACUCGUAAGAGGAGGUAUAGGGAGC-3` and 5`-GCTCTCTGCGAACTCGTAAGAGGAGGTATAGGGAGC-3` were used in melting experiments and fluorescence quenching experiments to determine the affinity of the novel compounds for nucleic acids (Figure 5.7). These constructs were designed to include many of the representative small molecule binding structural motifs found in nucleic acids including a helical region, mismatch pair, internal bulge and loop regions as well as a tetraloop.

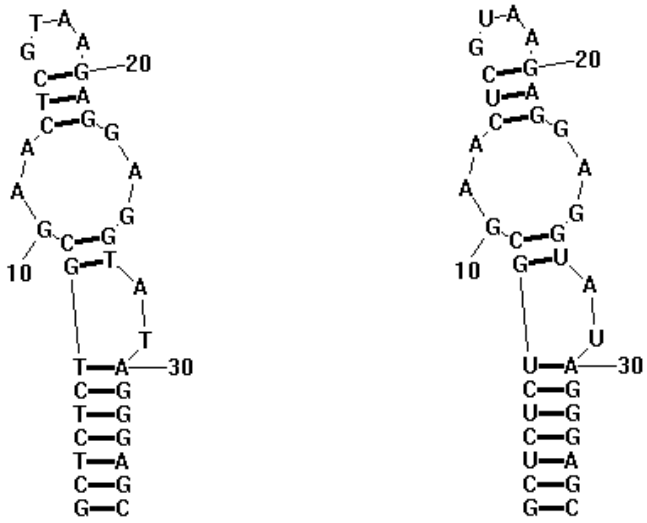

Figure 5.7 Secondary structure of the DNA and RNA constructs used in melting and quenching.

UV-vis melting experiments

UV melting experiments were performed in the absence of drug and in the presence of drug at a final concentration of 20 μM while the concentration of DNA or RNA was held constant at 2.5 μM. Nucleic acid and drug complexes were formed by the addition of an aliquot of stock drug solution in DMSO to a volume of DNA or RNA in BPE buffer (6mM Na_2HPO_4, 2mM $Na_2H_2PO_4$, 1mM EDTA, pH 7.1). The mixture was allowed to equilibrate for at least 20 min at 4°C to ensure complete association. The drug stock was prepared so that upon reaching the desired concentration of drug, the amount of DMSO in the sample was no >1% of the total volume. Melting studies were performed over a temperature range of 25–90°C, using a melting rate of 1°C/min and data were collected every half degree. In order to favor hairpin formation and avoid self-association, constructs were heated at 99°C for 1 min, then slowly cooled (1°C/min) to 10°C prior to being melted from 25°C to 90°C (57). For melting experiments, absorbance was measured at 260 nm, and the temperature was controlled with a Quantum Northwest TC 125 temperature control unit. The T_m was taken as the midpoint of the melting transition as determined by the maxima of first derivative plots. All T_ms were reproducible to within ±1°C. Repeated recording of heating and cooling profiles indicates that no hysteresis occurs in the absence or presence of ligand. Results of the melting studies including change in melting temperature (T_m) as well as change in Tm (ΔT_m) for DNA and RNA can be found in Table 5.3 and Table 5.4, respectively.

Fluorescence quenching experiments

Quenching of the drugs' natural fluorescence upon binding to DNA was monitored via titrations of a constant concentration of drug (7 μM) with DNA of increasing concentration (0.1–7 μM). Quenching experiments were performed in a 96-well black microplate following the protocol described by Hergenrother et al. (58). Fluorescence emission at 556nm was recorded on a Molecular Devices SpectraMAX Gemini microplate reader after excitation at 485nm. All experiments were repeated at least four times. The data collected in the fluorescence quenching titrations was fit to the linear Stern-Volmer equation (59):

$$I_o / I = 1 + K_{sv} * [Q]$$

Where I_o is the fluorescence intensity of drug in the absence of quencher, I is the fluorescence intensity after introduction of quencher, K_{sv} is the slope of the linear fit and Stern-Volmer constant, and [Q] is the concentration of quencher, in this case DNA. Stern-Volmer constants for DAU and all conjugate compounds can be found in Table 5.3. Stern-Volmer plots for all compounds can be found in Figure 5.8.

Table 5.3 Melting temperature, shift in melting temperature, and Stern-Volmer constants for all compounds and DNA.

	T_m	ΔT_m	K_{sv} (μmol^{-1})
No Drug	38.3	N/A	N/A
20 μM DAU	64.5	26.3	13
20 μM 7	62.2	23.9	8.0
20 μM 12a	42.2	3.9	2.0
20 μM 12b	41.5	3.3	0.58
20 μM 12c	52.0	13.8	0.21
20 μM 12d	61.3	23.1	5.1

Table 5.4 Melting temperature and shift in melting temperature for all compounds and RNA.

	T_m	ΔT_m
No Drug	51.6	N/A
20 μM DAU	56.0	4.4
20 μM 7	52.1	0.5
20 μM 12a	52.1	0.5
20 μM 12b	53.4	1.8
20 μM 12c	52.0	0.4
20 μM 12d	52.0	0.4

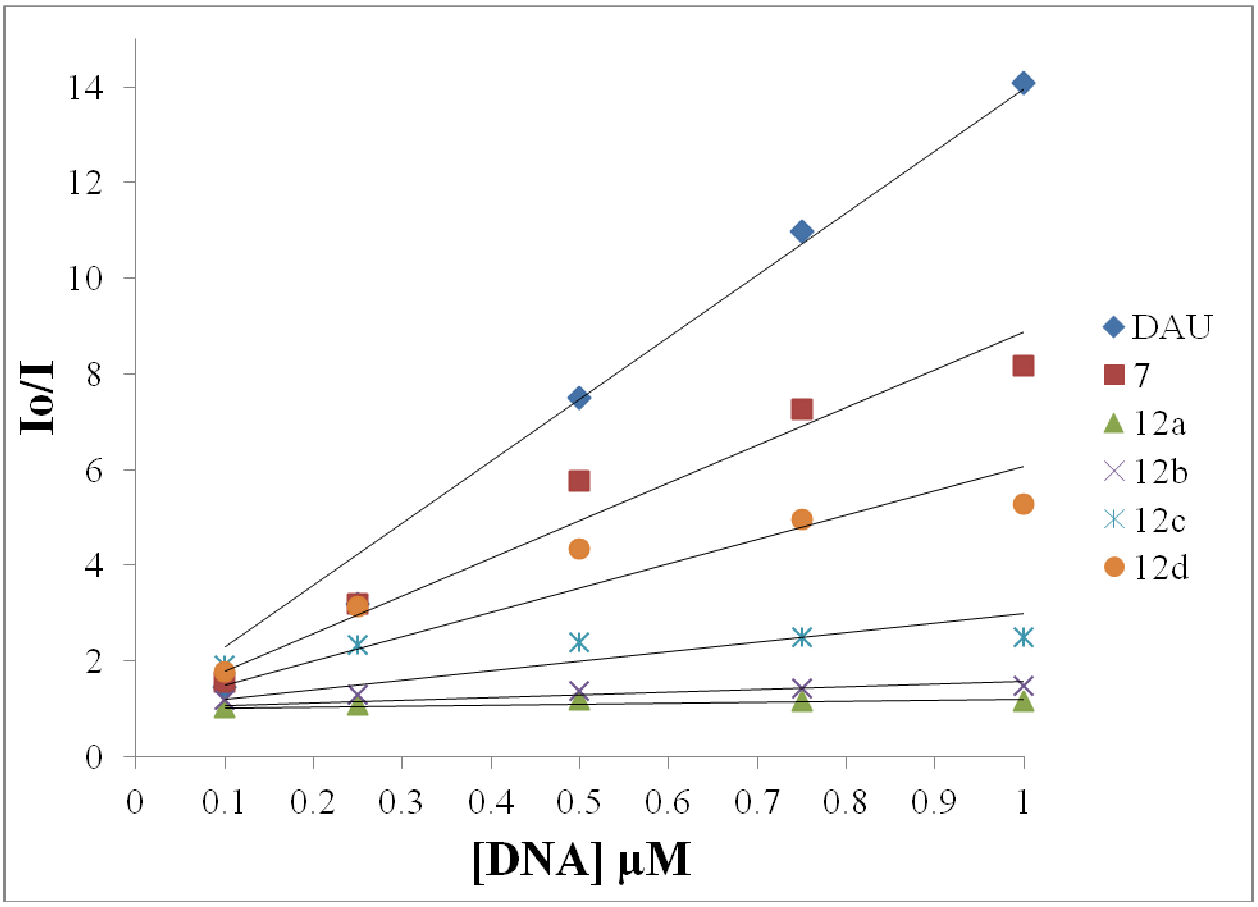

Figure 5.8 Stern-Volmer plots for all compounds and DNA.

5.9 Discussion

There is evidence for the synergistic effect of combined Topo II and HDAC inhibitors on cancer (38). However, this synergy is schedule dependent, hence traditional combination therapy involving Topo and HDAC inhibitors may be complicated by the inherent pharmacokinetic disadvantage of two separate drugs. To critically delineate the benefits of simultaneous Topo and HDAC inhibition in cancer therapy, it will be of interest to identify agents that possess Topo and HDAC inhibition activities within a single molecule. Toward this goal, we have rationally designed, successfully synthesized, and extensively characterized a novel class of Topo II / HDAC inhibitor conjugates joining the parent molecules of DAU and SAHA in two unique fashions. These conjugates were demonstrated to retain the activity of both parent molecules to some degree. *In vitro* HDAC inhibition assays showed that compound **7** most closely mirrored the inhibitory profile of SAHA while compound **12a** was shown to be the worst inhibitor. Compounds **12b-12d** displayed an impressive increase in HDAC inhibition of isoforms 1 and 2 (Table 5.1). All compounds were shown to retain Topo II inhibition through an *in vitro* KDNA decatenation assay (Figure 5.4). Compound **12b** was more potent than even DAU at inhibiting Topo II, and **12a** was the least effective inhibitor.

Whole cell viability assays demonstrated that with the retention of parent molecule activity came the retention of antiproliferative ability (Table 5.2). Compound **7** showed an incredibly potent inhibitory profile like DAU, while compounds **12a-12d** most imitated the profile of SAHA. It is this *in vivo* assay of activity that is most telling about the mode of action of the conjugates in that **7** most likely relies heavily on its DAU-like moiety to inhibit growth while **12a-12d** utilize their SAHA-like functionality. While the intracellular Topo II inhibition

assay showed compound **7** was unable to poison Topo II by stalling it in the cleavable ternary complex with itself and DNA (Figure 5.5 column 3), it has been demonstrated that this poisoning event is not necessary to retain topo II inhibition *in vivo* and is variable amongst cell lines (REF). Fluorescence microscopy studies further showed **7** to be a viable drug in that its localization in the cell most closely resembled DAU while **12b** seemed to suffer from poor uptake or an efflux mechanism (Figure 5.6).

To further characterize the novel TopoII / HDAC inhibitors, their ability to bind to nucleic acids was assessed in both a DNA and RNA hairpin target. The change in melting temperature observed after the binding of a small molecule drug to DNA can be used to assess the affinity of the molecule for its nucleic acid target (59). Table 5.3 shows that all conjugates retain the ability to bind to DNA to some extent. However, a drastic difference can be seen with the binding affinities of **7** and **12d** closely mimicking that of DAUthe (nearly identical ΔT_m) while **12c** induced a median shift in T_m. Compounds **12a** and **12b** caused minimal perturbation to T_m showing that their ability to bind to DNA has been severely hindered. This trend reveals that the amide linker of **7** is well tolerated, possibly allowing the daunosamine sugar to maintain its role in the minor groove interaction that compliments the DNA base-pair intercalative interaction of the aromatic aglycone portion of the anthracycline molecule. Interestingly, the data suggest that the triazole linker hinders the daunosamine sugar minor groove interaction when the linker length is too short. As evidenced by the increase in ΔT_m of **12d,** DNA binding capability is restored with a long enough linker. This is undoubtedly due to the inherent flexibility of a longer linker, yielding a more plastic nature of the tail moiety upon intercalation. In agreement with this are the Stern-Volmer constants derived for these compounds while binding to DNA (Table 5.4). The Stern-Volmer constant can be used to determine to the efficiency of a fluorescence

quencher. In this case the quencher is DNA and the quenching mechanism is attributed to the intercalation of the fluorophoric anthracycline ring system. Thus it is no surprise that DAU has the largest K_{sv} (13 μmol^{-1}) followed most nearly by **7** (8.0 μmol^{-1}) and next by **12d** (5.1 μmol^{-1}). The DNA target proved to be a poor quencher of compounds **12a-c** as evidenced by the flatness of their respective Stern-Volmer plots (Figure 5.8). This is likely attributable to the conjugates reduced ability to bind the DNA construct used in this study. However, when considered with the relatively large ΔT_m of 13.8 °C, the relatively small K_{sv} value of **12c** stands out. This would suggest that tail portion of the molecule is able to add to the overall binding ability via optimal positioning of hydrogen bond participants with respect to the minor groove.

Through melting studies performed with an RNA hairpin target, it was determined that the conjugates did not possess the parent DAU molecule's ability to bind to ribonucleic acid (Table 5.4). With the possibly detrimental interaction of anthracyclines with IRE RNA detailed in chapter 2 of this thesis, it would be of tremendous interest to see if there is any change in the deleterious side effects of these novel conjugates that seem to lack the ability to bind to RNA.

With the vast compliment of data presented to characterize the biological activity of the novel conjugates synthesized in this work, it is clear that each compound presents its own repertoire of affinities and activities. It is this uniqueness that warrants the future study of all of the compounds presented here in more complex biological systems.

Supporting Information Supporting information is available Appendix B.

5.10 References

1.) Morphy, R.; Kay, C.; Rankovic, Z. From magic bullets to designed multiple ligands. *Drug Disco*v *Today.* ***2004,*** 9, 641-651.

2.) Morphy, R.; Rankovic, Z. Designed Multiple Ligands. An Emerging Drug Discovery Paradigm. *J. Med. Chem.* **2005**, 48, 6523–6543.

3.) Frantz, S. Drug discovery: Playing dirty. *Nature.* **2005,** 437, 942-943**.**

4.) Roth, B. L.; Sheffler, D. J.; Kroeze, W. K. Magic shotguns versus magic bullets: Selectively non-selective drugs for mood disorders and schizophrenia. *Nat. Re*v. *Drug Disco*v. **2004,** 3, 353-359.

5.) Hopkins, A. L.; Mason, J. S.; Overington, J. P. Can we rationally design promiscuous drugs? *Curr. Opinion Struct. Biol*. **2006**, 16, 127-136

6.) Cmeserly, P.; Agoston, V.; Pongor, S. The efficiency of multi-target drugs: The network approach might help drug design. *Trends Pharmacol. Sci.* **2005***,* 26, 178-182.

7.) Fray, M.J; Bish, G.; Brown, A.D.; Fish, P.V.; Stobie, A.; Wakenhut, F.; Whitlock, G.A. *N*-(1,2-Diphenylethyl)piperazines: A new class of dual serotonin/noradrenaline reuptake inhibitor. *Bioorg. Med. Chem. Lett.* **2006**, 16, 4345-4348.

8.) Neumeyer, J.L.; Peng, X.; Knapp, B.I.; Bidlack, J.M.; Lazarus, L.H.; Salvadori, S.; Trapella, C.; Balboni, G. New opioid designed multiple ligand from Dmt-Tic and Morphinan pharmacophores. *J.Med. Chem.* **2006**, 49, 5640-5643.

9.) Jones, P. A.; Baylin, S. B. The epigenomics of cancer. *Cell.,* **2007,** 128, 683-692.

10.) Kouzarides, T. Chromatin modifications and their function. *Cell.* **2007,** 128, 693-705.

11.) Shilatifard, A. Chromatin modifications by methylation and ubiquitination: implications in the regulation of gene expression. *Ann. Rev. Biochem.* **2006,** 75, 243-269.

12.) Ropero, S; Esteller, M. The role of histone deacetylases (HDACs) in human cancer. *Mol. Oncol,* **2007**, 1, 19-25.

13.) Marks, P. A.; Richon, V. M.; Rifkind, R. A. Histone deacetylase inhibitors: inducers of differentiation or apoptosis of transformed cells. *J. Natl. Cancer Inst*. **2000**, 92, 1210-1216.

14.) Saito, A.; Yamashita, T.; Mariko, Y.; Nosaka, Y.; Tsuchiya, K.; Ando, T.; Suzuki, T.; Tsuruo, T.; Nakanishi, O. A synthetic inhibitor of histone deacetylase, MS-275, with marked *in vivo* antitumor activity against human tumors. *PNAS*. **1999**, 96, 4592-4597.

15.) Glick, R. D.; Swindemen, S. L.; Coffey, D. C.; Rifkind, R. A.; Marks, P. A.; Richon, V. M.; La Quaglia, M. P. Hybrid polar histone deacetylase induces apoptosis and CD95/CD95 ligand expression in human neuroblastoma. *Cancer Res*. **1999**, 59, 4392-4399.

16.) Butler, L. M.; Agus, D. B.; Scher, H. I.; Higgins, B.; Rose, A.; Cordon-Cardo, C.; Thaler, H. T.; Rifkind, R. A.; Marks, P.A.; Richon, V.M. Suberoylanilide hydroxamic acid, an inhibitor of histone deacetylase, suppresses the growth of prostate cancer cells *in vitro* and *in vivo*. *Cancer Res*. **2000**, 60, 5165-5170.

17.) Oyelere, A.K.; Chen, P.C.; Guerrant, W.; Mwakwari, S.C.; Hood, R.; Zhang, Y.; Fan, Y. Non-peptide macrocyclic histone deacetylases inhibitors. *J. Med. Chem*. **2009**, 52, 456-468.

18.) Gu, W and Roeder, RG. Activation of p53 sequence-specific DNA binding by acetylation of the p53 C-terminal domain. *Cell*. **1997**, 90, 595-606.

19.) Martinez-Balbás, M.A.; Bauer, U.M.; Nielsen, S.J.; Brehm, A.; Kouzarides, T. Regulation of E2F1 activity by acetylation. *EMBO J*. **2000**, 19, 662-671.

20.) Marzio, G.; Wagener, C.; Gutierrez, M.I.; Cartwright, P.; Helin, K.; Giacca, M. E2F family members are differentially regulated by reversible acetylation. *J. Biol. Chem*. **2000**, 275, 10887-10892.

21.) Hubbert, C.; Guardiola, A.; Shao, R.; Kawaguchi, Y.; Ito, A.; Nixon, A.; Yoshida, M.; Wang, X.F.; Yao, T.P. HDAC6 is a microtubule-associated deacetylase. *Nature*. **2002**, 417, 455-458.

22.) Kovacs, J.J.; Murphy, P.J.; Gaillard, S.; Zhao, X.; Wu, J.T.; Nicchitta, C.V.; Yoshida, M.; Toft, D.O.; Pratt, W.B.; Yao, T.P. HDAC6 regulates Hsp90 acetylation and chaperone-dependent activation of glucocorticoid receptor. *Mol. Cell*. **2005**, 18, 601-607.

23.) Mann, B.S.; Johnson, J.R.; Cohen, M.H.; Justice, R.; Padzur, R. FDA approval summary: vorinostat for treatment of advanced primary cutaneous T-cell lymphoma. *Oncologist*. **2007**, 12, 1247-1252.

24.) Grant, C.; Rahman, F.; Piekarz, R.; Peer, C.; Frye, R.; Robey, R.W.; Gardner, E.R.; Figg, W.D.; Bates, S.E. Romidepsin; a new therapy for cutaneous T-cell lymphoma and a potential therapy for solid tumors. *Expert Rev. Anticancer Ther.* **2010**, 10, 997-1008.

25.) Mwakwari, S.C.; Patil, V.; Guerrant, W.; Oyelere, A.K. Macrocyclic histone deacetylases inhibitors. *Curr. Top. Med. Chem.* **2010**, 10, 1423-1440.

26.) Kelly, W. K; O'Connor, O. A.; Marks, P. A. Histone deacetylase inhibitors: from target to clinical trials. *Expert. Opin. Investig. Drugs.* **2002**, 11, 1695-1713.

27.) Rosato, R. R.; Grant, S. Histone deacetylase inhibitors in clinical development. *Expert Opin. Invest. Drugs.* **2004**, 13, 21-38.

28.) Yoo, C. B.; Jones, P. A. Epigenetic therapy of cancer: past, present and future. *Nature Rev. Drug Discov.* **2006**, 5, 37-50.

29.) Finnin, M. S.; Donigian, J. R.; Cohen, A.; Richon, V.M.; Rifkind, R.A.; Marks, P.A.; Breslow, R.; Pavletich, N.P. Structures of a histone deacetylase homologue bound to the TSA and SAHA inhibitors. *Nature.* **1999**, *401*, 188–193.

30.) Wang, D.-F.; Wiest, O.; Helquist, P.; Lan-Hargest, H-Y; Wiech, N.L. On the function of the 14 Å long internal cavity of histone deacetylase-like protein: implication for the design of histone deacetylase inhibitors. *J. Med. Chem.* **2004**, *47*, 3409–3417.

31.) Chen, L.; Wilson, D.; Jayaram, H.N.; Pankiewicz, K.W. Dual inhibitors of inosine monophosphate dehydrogenase and histone deacetylases for cancer treatment. *J. Med. Chem.* **2007**, 50, 26, 6685-6691.

32.) Mahboobi, S.; Dove, S.; Sellmer, A.; Winkler, M.; Eichhorn, E.; Pongratz, H.; Ciossek, T.; Baer, T.; Maier, T.; Beckers, T. Design of chimeric histone deacetylase- and tyrosine kinase-inhibitors: a series of iminatib hybrids as potent inhibitors of wild-type and mutant BCR-ABL, PDGF-Rβ, and histone deacetylases. *J. Med. Chem*. **2009**, 52, 8, 2265-2279.

33.) Cai, X.; Zhai, H-X.; Wang, J.; Forrester, J.; Qu, H.; Yin, L.; Cheng-Jung, L.; Bao, R.; Qian, C. Discovery of 7-(4-(3-ethynylphenylamino)-7-methoxyquinazolin-6-yloxy)-N-hydroxyheptanamide (CUDC-101) as a potent multi-acting HDAC, EGFR, and HER2 inhibitor for the treatment of cancer. *J. Med. Chem*. **2010**, 53, 5, 2000-2009.

34.) Piccart-Gebhart, M. J. Anthracyclines and the tailoring of treatment for early breast cancer. *N. Engl. J. Med*. **2006**, 354, 2177-2179.

35.) Kim, M. S.; Blake, M.; Baek, J. H.; Kohlhagen, G.; Pommier, Y.; Carrier, F. Inhibition of histone deacetylase increases cytotoxicity to anticancer drugs targeting DNA. *Cancer Res.* **2003**, 63, 7291–7300.

36.) Catalano, M.G.; Fortunati, N.; Pugliese, M.; Poli, R.; Bosco, O.; Mastrocola, R.; Aragno, M.; Bocuzzi, G. Valproic acid, a histone deacetylase inhibitor, enhances sensitivity to doxorubicin in anaplastic thyroid cancer cells. *J. Endocrinol*. **2006**, 191, 2, 465-472.

37.) Johnson, C.A.; Padget, K.; Austin, C.A.; Turner, B.M. Deacetylase activity associates with topoisomerase II and is necessary for etoposide-induced apoptosis. *J. Biol. Chem*. **2001**, 276, 7, 4539-4542.

38.) Marchion, D.C.; Bicaku, E.; Daud, A.I.; Richon, V.; Sullivan, D.M.; Munster, P.N. Sequence-specific potentiation of topoisomerase II inhibitors by the histone deacetylase inhibitor suberoylanilide hydroxamic acid. *J. Cell Biochem.* **2004**, 92, 2, 223-237.

39.) Tewey, K.M.; Rowe, T.C.; Yang, L.; Halligan, B.D.; Liu, L.F. Adriamycin-induced DNA damage mediated by mammalian DNA topoisomerase II. *Science*. **1984**, 226, 466-468.

40.) Binaschi, M.; Bigioni, M.; Cipollone, A.; Rossi, C.; Goso, C.; Maggi, C.A.; Capranico, G.; Animati, F. Anthracyclines: selected new developments. *Curr. Med. Chem. Anticancer Agents*. **2001**, 1, 2, 113-130.

41.) Pommier, Y.; Schwartz, R.E.; Kohn, K.W.; Zwelling, L.A. Formation and rejoining of deoxyribonucleic acid double-strand breaks induced in isolated nuclei by antineoplastic intercalating agents. *Biochemistry*. **1984**, 23, 3194-3201.

42.) Kiyomiya, K.; Matsuo, S.; Kurebe, M. Proteasome is a carrier to translocate doxorubicin from cytoplasm into nucleus. *Life Sci*. **1998**, 62, 20, 1853-1860.

43.) Kiyomiya, K.; Matsuo, S.; Kurebe, M. Mechanism of specific nuclear transport of adriamycin: the mode of nuclear translocation of adriamycin-proteasome complex. *Cancer Res*. **2001**, 61, 2467-2471.

44.) Tong, G.L.; Wu, H.Y.; Smith, T.H.; Henry, D.W. Adriamycin analogs. 3. synthesis of N-alkylated anthracyclines with enhanced efficacy and reduced toxicity. *J. Med. Chem.* **1979**, 22, 912-918.

45.) Martín, B.; Vaquero, A.; Priebe, W.; Portugal, J. Bisanthracycline WP631 inhibits basal and Sp1-activated transcription initiated *in vitro*. *Nucleic Acids Res*. **1999**, 27, 3402-3409.

46.) Lothstein, L.; Israel, M.; Sweatman, T.W. Anthracycline drug targeting: cytoplasmic versus nuclear – a fork in the road. *Drug Resist. Updat*. **2001**, 4, 169-177.

47.) Gate, L.; Couvreur, P.; Nguyen-Ba, G.; Tapiero, H. N-methylation of anthracyclines modulates their cytotoxicity and pharmacokinetics in wild type and multidrug resistant cells. *Biomed & Pharmacotherapy*. **2003**, 57, 301-308.

48.) (a) Mwakwari, S.C.; Guerrant, W.; Patil, V.; Khan, S.I.; Tekwani, B.L.; Gurard-Levin, Z.A.; Mrksich, M.; Oyelere, A.K. Non-peptide histone deacetylases inhibitors derived from tricyclic ketolide skeleton. *J. Med. Chem*. **2010**, 53, 6100-6111.; (b) Chen, P.C.; Patil, V.; Guerrant, W.; Green, P.; Oyelere, A.K. Synthesis and structure-activity relationship of histone deacetylase (HDAC) inhibitors with triazole-linked cap group. *Bioorg. Med. Chem*. **2008**, 16, 4839-4853.

49.) Marini, J.C.; Miller, K.G.; Englund, P.T. Decatenation of kinetoplast DNA by topoisomerases. *J. Biol. Chem*. **1980**, 255, 11, 4976-4979.

50.) Sahai, B and Kaplan, *J.* A quantitative decatenation assay for type II topoisomerases. *Anal. Biochem*. **1986**, 156, 2, 364-379.

51.) Qu, X.; Wan, C.; Becker, H.C.; Zhong, D.; Zewail, A.H. The anticancer drug-DNA complex: femtosecond primary dynamics for anthracycline antibiotics function. *PNAS*. **2001**, 98, 25, 14212-14217.

52.) Kulp, S.K.; Chen, C.S.; Wang, D.S.; Chen, C.Y.; Chen, C.S. Antitumor effects of a novel phenylbutyrate-based histone deacetylases inhibitor, (*S*)-HDAC-42, in prostate cancer. *Clin. Cancer Res*. **2006**, 12, 5199-5206.

53.) Doyle, L.A.; Abruzzo, Y.W.; Krogmann, T.; Yongming, G.; Rishi, A.K.; Ross, D.D. A multidrug resistance transporter from human MCF-7 breast cancer cells. *PNAS*. **1998**, 95, 15665-15670.

54.) Gao, H.; Huang, K.C.; Yamasaki, E.F.; Chan, K.K.; Chohan, L.; Snapka, R.M. XK469, a selective topoisomerase IIβ poison. *Proc. Natl. Acad. Sci*. **1999**, 96, 12168-12173.

55.) Kiyomiya, K.; Satoh, J.; Horie,H. ;Kurebe, M.; Nakagawa, H.; Matsuo, S. Correlation between nuclear action of anthracycline anticancer agents and their binding affinity to the proteosome. *Int. J. Oncol.* **2002**, 21, 5, 1081-1085.

56.) Marbeuf-Gueye, C.; Ettori, D.; Priebe, W.; Kozlowski, H.; Garnier-Suillerot, A. Correlation between the kinetics of anthracycline uptake and the resistance factor in cancer cells expressing the multidrug resistance protein or the P-glycoprotein**.** *Biochim Biophys Acta.* **1999,** 1450, 3, 374-384..

57.) Proctor,D., Kierzek,E., Kierzek,R. and Bevilacqua,P. (2003) Restricting the conformational heterogeneity of RNA by specific incorporation of 8-bromoguanosine. *J. Am. Chem. Soc*., **125**, 2390–2391.

58.) Thomas,J., Liu,X. and Hergenrother,P. (2005) Size-specific ligands for RNA hairpin loops. *J. Am. Chem. Soc*., **127**, 12434–12435.

59.) Canzoneri JC, Oyelere AK. (2008) Interaction of anthracyclines with iron responsive element mRNAs. *Nucleic Acids Res*. **36**, 6825-34.

CHAPTER 6: MOLECULAR ARCHITECTURE OF ZINC BINDING SMALL MOLECULES THAT INHIBIT SPLICESOME ASSEMBLY

This work was published by Vishal Patil, Joshua Canzoneri, Timur R. Samatov, Reinhard Lührmann, and Adegboyega K. Oyelere in RNA 2012 (in press). That manuscript is presented here unchanged.

6.1 Introduction

The removal of intervening sequences (introns) from a primary RNA transcript is catalyzed by the spliceosome, a large ribonucleoprotein complex. At the start of each splicing cycle the spliceosome assembles anew on the pre-mRNA intron to be removed, in a sequentially ordered manner. We describe here the identification of a series of naphthalen-2-yl hydroxamate compounds that inhibit pre-mRNA splicing in vitro with mid- to high-micromolar values of IC_{50}. These hydroxamates stall the spliceosome assembly at the "A complex" stage. A structure–activity analysis on lead compounds revealed three pharmacophores that are essential for splicing inhibition. Specifically, a hydroxamate as a zinc-binding group and a 6-methoxynaphthalene cap group are both critical, and a linker chain comprising 8–9 methylene groups is also important, for the specific binding to the docking site of target protein molecule and precise positioning of the zinc binding group. As we found no correlation between the inhibition patterns of known histone deacetylases on the one hand and pre-mRNA splicing on the other, we conclude that these compounds may function through the inhibition of the activities of other, at present, unknown spliceosome-associated zinc metalloprotein(s).

The removal of introns from a primary RNA transcript is catalyzed by a large RNP complex termed the spliceosome. This is a highly complex and dynamic RNP machine. It is composed of the five snRNPs U1, U2, U4, U5, and U6 and a large number of non-snRNP proteins (Wahl et al., 2009). Spliceosomes assemble in a stepwise manner and thus pass through a series of distinct complexes. Initially, the U1 and U2 snRNPs bind the pre-mRNA, forming the

A complex. Subsequently, the U4/U6.U5 tri-snRNP associates, and the precatalytic B complex is generated. After major rearrangements resulting in the displacement of U1 and U4, the activated spliceosome (B^{act}) is formed, followed by additional restructuring and catalysis of step 1 of splicing. This involves cleavage at the 5' splice site of the pre-mRNA and the ligation of the 5' end of the intron to the so-called branch site to form a lariat-like structure. This leads to formation of the spliceosomal C complex, which catalyzes step 2 of splicing, during which the intron is excised and the exons are ligated together to form mRNA. After this the spliceosome dissociates and the snRNPs are recycled for additional rounds of splicing.

Aberrant pre-mRNA splicing is associated with many human diseases, including cancer, neurodegenerative and autoimmune diseases, making the spliceosome a highly attractive drug target (Tazi et al., 2005b). Small molecules arresting spliceosome assembly at defined points would also be of great use for the detailed investigation of the structure and function of the spliceosome.

To date, only a limited number of small-molecule inhibitors of pre-mRNA splicing have been identified. These include antibiotics (erythromycin, Cl-tetracycline, and streptomycin) (Hertweck et al., 2002), a biflavonoid (isoginkgetin) (O'Brien et al., 2008), inhibitors of the kinase activity of topoisomerase I (Pilch et al., 2001; Tazi et al., 2005a), antitumor drugs targeting the U2 snRNP Spliceostatin A (Kaida et al., 2007) and pladienolide (Kotake et al., 2007), selected inhibitors of histone deacetylases and histone acetyltransferases (Kuhn et al., 2009), lichen secondary metabolites (Samatov et al., 2012) and 1,4-naphthoquinones and 1,4-heterocyclic quinones with known anticancer activity (Berg et al., 2012). The specific spliceosome targets have been identified for only a few of those compounds. The lack of clear understanding may be partly due to the structural complexities of many of these compounds.

Several spliceosome-associated proteins possess potential enzymatic activities whose function in the splicing reaction remains unclear (Rappsilber et al., 2002; Zhou et al., 2002; Hartmuth et al., 2002; Jurica and Moore, 2003; Deckert et al., 2006). For example, numerous peptidyl–prolyl isomerases have been found, even though it is not clear whether the isomerase activity is required at all, or whether their domains are involved in protein–protein interactions. In addition, many proteins exhibit zinc-binding motifs, suggesting that zinc ions may have functional and/or structural roles in splicing (Rappsilber et al., 2002; Zhou et al., 2002; Jurica and Moore, 2003; Agafonov et al., 2011). Additionally, the activity of histone deacetylases (HDACs), which are classical zinc metalloproteases, has been shown to be important for splicing catalysis, although their precise functions in the splicing process are not clear (Hnilicova et al., 2011). In fact, zinc depletion by the chelator 1,10-phenanthroline (1,10-phe) has been shown to inhibit the second step of splicing (Shomron et al., 2002). It has been demonstrated that specific zinc-chelating agents that perturb protein acetylation state (through inhibition of HDACs activity) block the splicing cycle (Kuhn et al., 2009). The exact relationship between zinc chelation, protein acetylation state and splicing reaction integrity was not clear from that study, as only a limited set of HDAC inhibitors (HDACi) was screened. In the present work, we sought to clarify this relationship by screening a HDACi library that was structurally more diverse (Canzoneri et al., 2009; Chen et al., 2008; Mwakwari et al., 2010a; Mwakwari et al., 2010b; Oyelere et al., 2009; Patil et al., 2010). We report here the elucidation of unique molecular features that confer splicing inhibition upon zinc-chelating agents with HDACi activity. Native gel analysis of the spliceosome assembly revealed that it is inhibited at an early stage, and the formation even of the A complex is compromised. The absence of correlation between HDAC

and the splicing-inhibition activities of these compounds suggests that the primary target(s) of their splicing inhibition are not HDACs. However, the existence of certain similarities does suggest possible structural resemblance(s) in the docking site and a common involvement of zinc ions.

6.2 Screening of Structurally Diverse HDACi for Splicing Inhibition

Earlier work had demonstrated the presence of HDACs in purified population of spliceosome (Rappsilber et al., 2002; Zhou et al., 2002; Gunderson et al., 2011), and on this basis we previously investigated the prospect of splicing inhibition by selected HDACi (Kuhn et al., 2009). These HDACi inhibited splicing with sub- to low-millimolar values of IC50 (the concentration giving 50% inhibition). However, there was no clear evidence linking the effects of these HDACi on splicing with their actual HDAC inhibition, especially as their IC50 values in splicing were found to be several orders of magnitude higher than the reported values for HDAC inhibition. HDAC has 18 known isoforms, organized into four different classes. Classes I, II, and IV depend on a catalytic zinc ion and differ in their cellular location, while Class III HDACs require NAD+ (Ropero and Esteller, 2007). The prototypic pharmacophore for HDACi consists of three distinct structural motifs: a recognition cap group, a hydrophobic linker, and the zinc-binding group (Fig. 6.1; Mwakwari et al., 2010b; Miller et al., 2003).

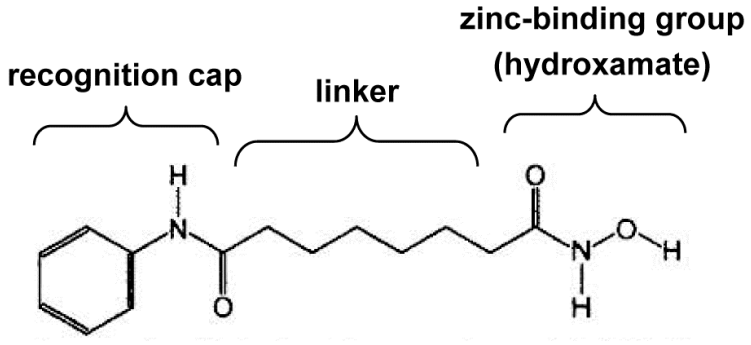

Figure 6.1 The prototypic pharmacophore for histone deacetylase inhibitors (here SAHA), which typically is comprised of three distinct structural motifs: a recognition cap group, a hydrophilic linker and a zinc-binding group.

The HDACi recognition cap group moieties undergo interaction with amino-acid residues on the surface of HDACs and present excellent opportunities for the selective modulation of their biological activities (Mwakwari et al., 2010b). We surmised that profiling the splicing inhibition activities of HDACi that differ in respect of their three distinct structural motifs might help us to discern possible links between HDAC inhibition and inhibitory effects on the splicing reaction. To this end, we first screened a small (63-member), yet structurally diverse HDACi library (See Supplemental Table S1 for the structures) at 100 μM using a conventional in vitro splicing assay. The HDACi activity of compounds in the screened library against HDAC1 and HeLa cell nuclear extract HDACs ranges from single digit- to mid-nanomolar (Canzoneri et al., 2009; Chen et al., 2008; Mwakwari et al., 2010a; Oyelere et al., 2009; Patil et al., 2010). Despite their potency, these HDACi did not broadly inhibit splicing. We identified only two compounds – 6-methoxynaphthalen-2-yl hydroxamates **24** and **25** that noticeably inhibit splicing at 100 μM (Fig. 6.2). The structures of these compounds are almost identical, differing only in the length of a hydrophobic linker, 6 methylene groups for **24** and 7 for **25**. More detailed investigation revealed that these compounds inhibit pre-mRNA splicing with the same efficiency (Fig. 2B). Complete inhibition of splicing was observed at 150 μM (Fig. 2B, lanes 4 and 8), with an IC50 value of approximately 130 μM for both compounds (Table 6.1).

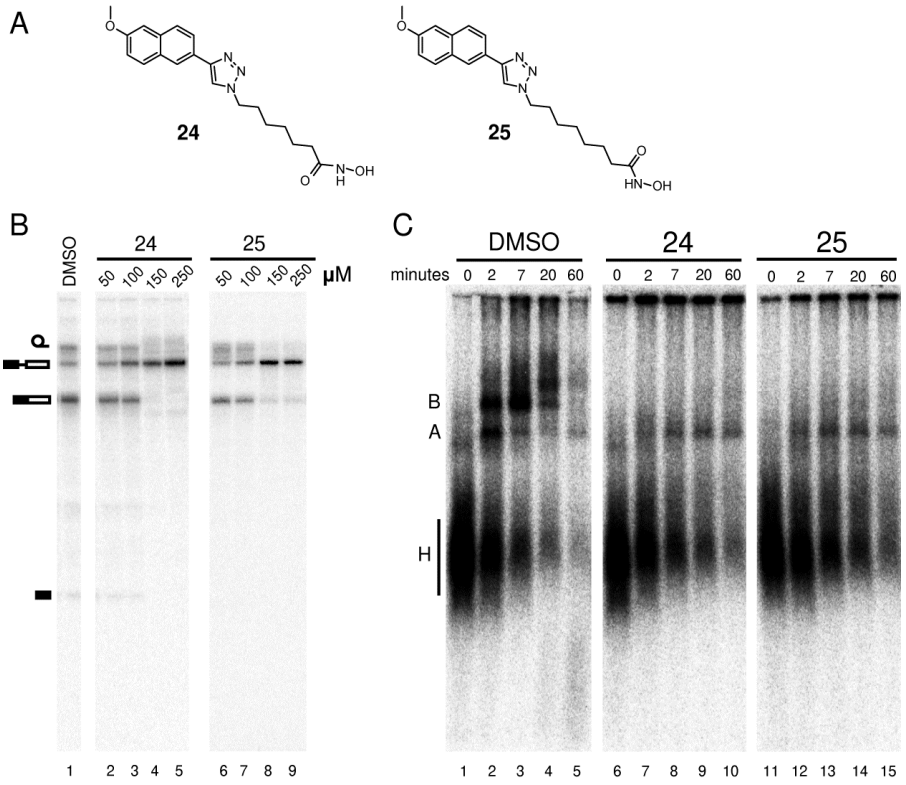

Figure 6.2 Hit compounds **24** and **25** inhibit pre-mRNA splicing in vitro and lead to an accumulation of spliceosome assembly intermediates: (*A*) Structures of the compounds. (*B*) Increasing concentrations of compounds **24** and **25** were tested for their effect on the splicing of ^{32}P-labeled MINX pre-mRNA. After splicing, the radiolabeled RNA was analyzed by denaturing PAGE followed by autoradiography. The leftmost lane shows the DMSO control experiment. Compound numbers are shown in the top panel, and drug concentrations tested are shown immediately below the compound numbers. The positions of lariat-intron, pre-mRNA, fully spliced mRNA, and 5'-exon (top to bottom) are indicated on the left. (*C*) Formation of splicing complex on ^{32}P-labeled MINX pre-mRNA in the presence of 250 µM of the respective compounds. Reactions were stopped at the time points indicated, and the products were analyzed on a native agarose gel. Bands were visualized by phosphor imaging. The positions of the splicing complexes (H, A and B) are indicated.

Table 6.1 Structure–activity relationships of the splicing inhibition activities of 6-methoxynaphthalen-2-yl hydroxamates. [a]Cited from refs (Chen et al., 2008; Patil et al., 2010) – activities against HeLa nuclear extract (HDAC 1 & 2). NT, not tested; NI, no significant inhibition (below 20%). % HDAC inhibition activities of the compounds at 10 µM are given if the IC_{50} was above 10 µM.

Modified structural motif	Number of methylene groups of the linker	Compounds	IC_{50}			
			HDAC1	HDAC6	HDAC8	pre-mRNA splicing
Linker	6	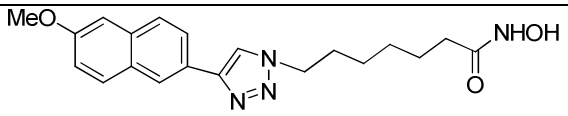 **24**	15.3[a] nM	NT	NT	134+/- 8 µM
Linker	7	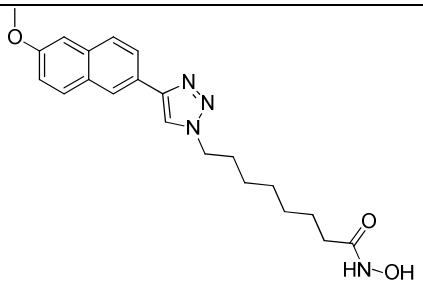 **25**	226.1[a] nM	NT	NT	129+/- 4 µM
Linker	8	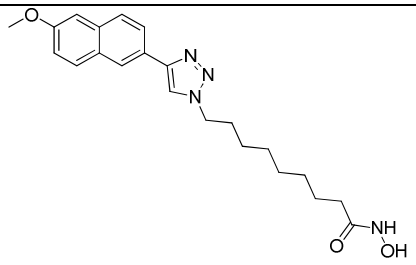 **67a**	55+/- 4 nM	93+/- 7 nM	NI	94+/- 3 µM

Table 6.1 Continued

Linker	9	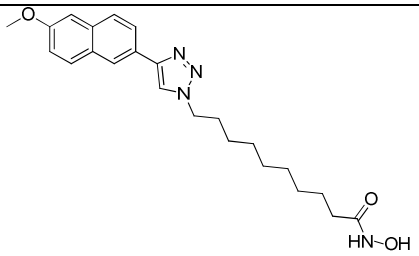 **67b**	155+/- 17 nM	212+/- 26 nM	NI	78+/- 10 µM
Linker	10	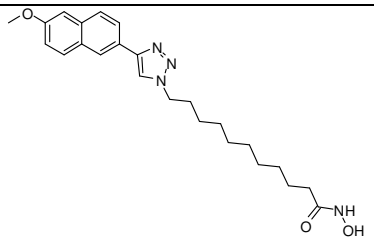 **67c**	9298+/- 1453 nM	400+/- 29 nM	245+/- 18 nM	135+/- 12 µM
Linker	11	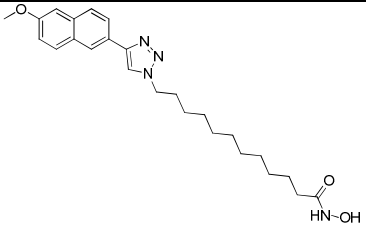 **67d**	28%	5390+/- 734 nM	NI	161+/- 23 µM
Cap group	6	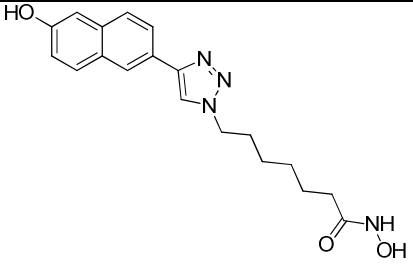 **70b**	1+/- 0.1 nM	2 +/- 0.1 nM	252+/- 28 nM	NI
Cap group	6	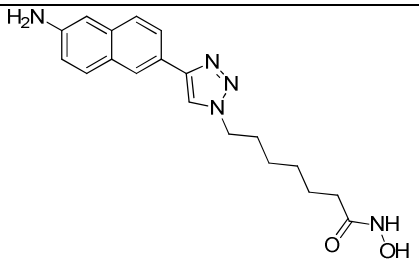	1+/- 0.1 nM	5+/- 0.6 nM	810+/- 158 nM	NI

Table 6.1 Continued

		70c				
Cap group	7	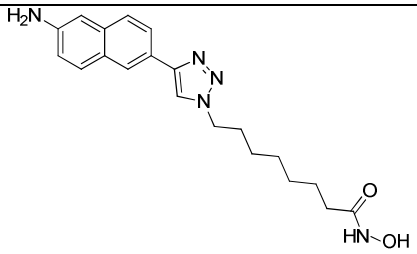 **70d**	5 +/- 0.4 nM	49+/- 2.6 nM	2300+/- 540 nM	NI
Cap group	7	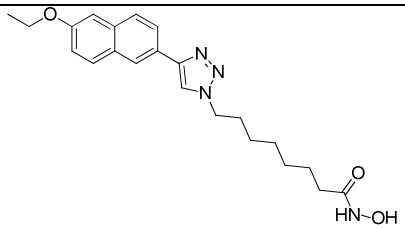 **74a**	25+/-2 nM	47+/-4 nM	5292+/- 605 nM	142+/- 11 µM
Cap group	9	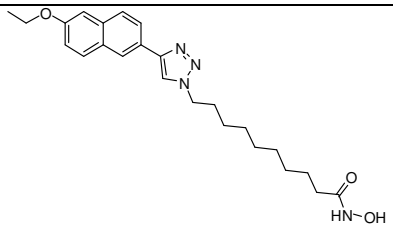 **74b**	311+/- 32 nM	251+/- 26 nM	4706+/- 561 nM	81+/- 8 µM
Zinc-binding group	6	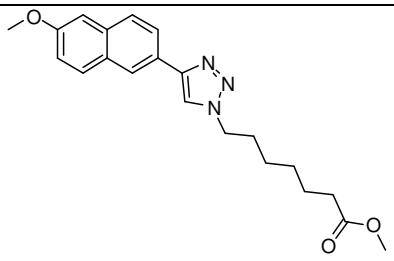 **80**	NI	NI	NI	NI

Table 6.1 Continued

Zinc-binding group	6	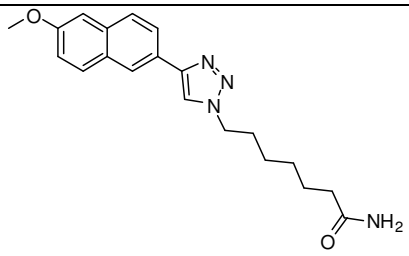 **82**	NI	22%	27%	NI
Zinc-binding group	9	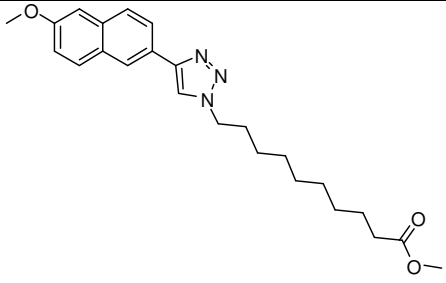 **81**	NI	NI	NI	NI
—	—	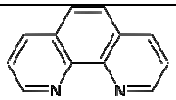 **1,10-phe**	NT	NT	NT	2950+/-210 μM

Table 6.1 Continued

To determine at which stage splicing complex formation is inhibited, we performed a splicing time-course experiment. The spliceosomal complexes formed were analyzed by native agarose gel electrophoresis. After 2 min of splicing, predominantly A and B complexes were visible in the DMSO control (Fig. 6.2C, lane 2). After 7 min, most A complexes had been converted into B complexes, which were in turn converted into later complexes (B^{act}, C) after 20 min. After 60 min only small amounts of the A, B^{act} and C were still visible (lanes 3-5). In the presence of 250 μM of compound **24** or **25**, the kinetics of splicing complex assembly appeared similar to each other and differed dramatically from those in a DSMO control (Fig. 6.2C, lanes 6-15). Mainly A complexes accumulated at all of the time points analyzed. Thus, the formation of B complexes is inhibited, indicating that one or more protein factors required for it are inactivated by these compounds. Besides, the amount of stalled A complexes was significantly lower than in the DMSO control reaction (compare the 2-minute time point, lane 2). This indicates that the formation of A complexes is compromised by these HDACi. These data imply that potential targets of the compounds are also among the proteins needed for assembly of the A complex. Remarkably, compound **24** has an HDACi activity 15 times higher than that of compound **25** (Table 6.1; Patil et al., 2010), yet both compounds stalled the spliceosome assembly to about the same extent. Another intriguing observation is the fact that compound **9** (Supplemental Table S1), an analog of **24** with a single methylene chain deletion, and a more than 8-fold stronger HDACi than **24** (Chen et al., 2008), was not identified as a splicing inhibitor in the primary screen. These data, together with the fact that only two structurally related compounds have been identified among the 63 diverse potent HDAC inhibitors, suggest that the target(s) of splicing inhibition by these compounds may not be HDACs.

The screening of the HDACi library (Oyelere et al., 2009; Patil et al., 2010) for splicing inhibition identified 6-methoxynaphthalen-2-yl hydroxamates **24** and **25** as small molecules that inhibit splicing in a specific context. Both compounds inhibit spliceosome assembly at an early stage, to about the same extent, with IC50 values close to 130 μM (Table 6.1). These data provided the initial indication that the inhibition of splicing may be not due to HDAC targets. To investigate this question further we carried out a detailed structure–activity analysis of the compounds. We synthesized a series of structural analogs of compounds **24** and **25** and tested their effect on the in vitro splicing of ^{32}P-labeled MINX pre-mRNA as well as their HDAC inhibition activity against representative class I and class II HDAC isoforms – HDAC1, HDAC6 and HDAC8. First, we investigated the length of a hydrophobic linker between a recognition cap and zinc-binding groups. Compounds **24** and **25** have 6- and 7-methylene chain linkers, respectively (Table 6.1). A shorter version present in the initial compound collection, with 5 methylene groups, was filtered out as inactive against splicing (compound **9**, Supplemental Table S1). We experimented with introducing longer linkers. Indeed, the single (compound **67a**) as well as the double (compound **67b**) methylene chain extensions significantly increased the potency (Table 6.1). Further increase in the length resulted in compounds that were less active, **67c** and the slightly less potent **67d** (although these were still almost as potent as the lead compounds **24** and **25**). Thus there is a correlation between the anti-splicing activity and the length of the linker, with an optimum number of methylene groups of 8 and 9. As for the HDACi activity, compounds **67a** and **67b** inhibited HDAC1 and HDAC6 with mid-nanomolar IC_{50}s and were completely inactive against HDAC8, while **67c** potently inhibited HDAC6 and HDAC8 and was almost inactive against HDAC1. Interestingly compound **67d** had the poorest HDAC

inhibition activity; it was found to be inactive against HDAC1 and HDAC6 and weakly active against HDAC8, yet it showed significant inhibition of splicing.

Another structural motif of the pharmacophore that we investigated was the naphthalene cap group. The substitution of 6-methoxy moiety by a protic electron-donating group such as OH or NH_2 is detrimental to the function of the compounds, as these changes abolished splicing inhibitory activity (Table 6.1; compare **70b** and **70c** with **24**; **70d** with **25**). In contrast, compounds **70b**, **70c** and **70d** were found to be broadly active against the HDAC isoforms tested, with single-digit nanomolar to mid-nanomolar IC_{50}s against HDAC1 and HDAC6. The observation that there is no correlation between anti-HDAC and anti-splicing activities of these molecules supports the suggestion that the targets of these compounds in splicing are not HDACs. Besides, these data suggest that the naphthalene cap group needs to be specifically recognized by the target protein(s). It is noteworthy that compounds **74a** and **74b** – with a single methylene extension of the naphthalene cap 6-ether moiety compared with **25** and **67b**, respectively – possess almost the same splicing inhibitory activity as the initial molecules.

To investigate the role of zinc chelation in the splicing-inhibitory activity of these naphthalene-2-yl hydroxamates, we synthesized methyl esters **80** and **81**, and carboxamide **82**. These compounds are the derivatives of the hydroxamates **24** and **67b**. As expected, all of these non-hydroxamate analogs lacked HDAC-inhibition activity. Significantly, they also failed to inhibit splicing in vitro (Table 6.1). These results indicate that zinc coordination is important for both anti-HDAC and anti-splicing activities. An add-back experiment was performed to test whether the inhibition is indeed due to the chelation of zinc (Fig. 6.3).

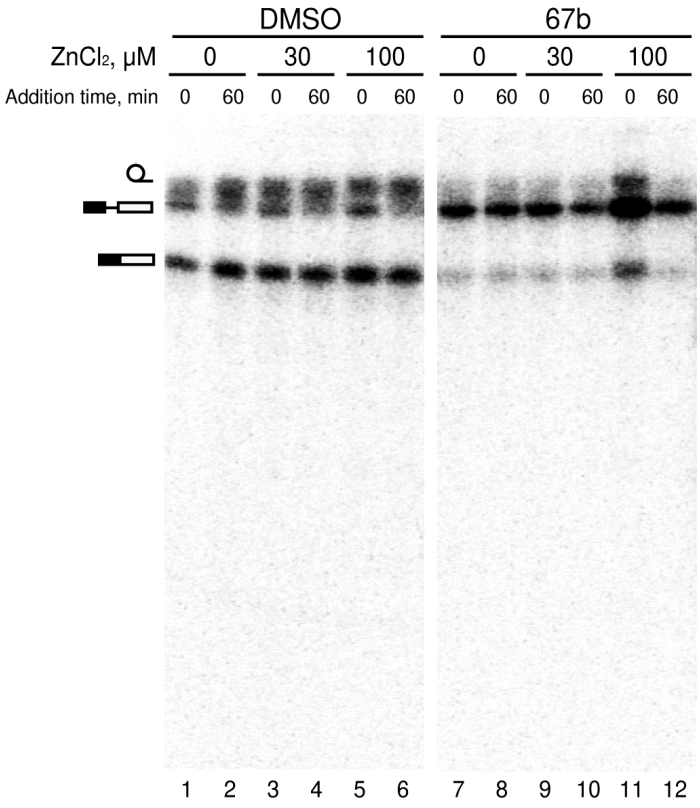

Figure 6.3 Relieving the inhibitory effect of the compound **67b**. Radiolabeled MINX pre-mRNA was incubated in nuclear extract under standard splicing conditions in the presence of DMSO (lanes 1–6) or semi-inhibitory 100 μM concentration of the compound **67b** (lanes 7–12) and the indicated concentrations of $ZnCl_2$ added at the indicated reaction time points. After splicing, the radiolabeled RNA was analyzed by denaturing PAGE followed by autoradiography. The positions of lariat-intron, pre-mRNA, and fully spliced mRNA (top to bottom) are indicated on the left.

The indicated concentrations of $ZnCl_2$ were added at the beginning of the splicing reaction (addition time 0 min, odd lanes) or after 1 h incubation (addition time 60 min, even lanes), followed by another 60 min incubation under splicing conditions. The addition of 30 and 100 μM $ZnCl_2$ to the control reaction with DMSO had little effect on splicing, although the pre-mRNA substrate appeared to be slightly stabilized in some cases (lanes 1-6). The splicing reaction was substantially inhibited in the presence of 100 μM **67b**, one of the most potent

compounds described here (lanes 7 and 8). Addition of 30 μM $ZnCl_2$ before initiation of the splicing reaction, did not reverse inhibition by **67b**, whereas addition of 100 μM $ZnCl_2$ restored splicing efficiency to near control levels (lanes 9 and 11). Addition of 100 μM $ZnCl_2$ also led to a general increase in the amount of the splicing substrate, but the observed increase in the splicing products is not due solely to this apparent stabilization effect. Interestingly, addition of $ZnCl_2$ to the inhibited splicing reaction 1 h later had no effect (lanes 10 and 12). These data suggest that compound **67b** irreversibly inhibits splicing; once it binds to its target protein and chelates its zinc ion, the inhibitory effect, which could potentially involve a structural change in the targeted protein, can no longer be reversed by exogeneously added zinc ions. In contrast, allowing compound **67b** to bind zinc prior to interacting with its target protein, neutralizes its inhibitory effect, presumably by preventing **67b** from removing the zinc that is normally bound by its target protein. This result confirms the principal role of zinc chelation in the mechanism of action of the compounds described. However, one should note the dramatic difference between the effects observed here, and those of the zinc chelation by 1,10-phe, which requires millimolar concentrations and results in the reversible inhibition of the step 2 of splicing (Table 6.1; Shomron et al., 2002).

6.3 Conclusions

All three structural motifs of the pharmacophore for HDACi exhibit a synergistic activity, as the cap group and linker are both important for the specific binding to the docking site of the target protein molecule and precise positioning of the zinc-binding group for effective zinc chelation. The SAR analysis of the compounds identified that inhibit splicing reveals that all three groups are important for splicing inhibition activity, though to different degrees: the intact zinc-binding group is absolutely essential, and the naphthalene cap group is also important; the hydrophobic linker has a more pronounced length restriction in that linkers with 8 and 9 methylene groups confer the highest activity upon the compounds. Taken together, our data suggest that splicing inhibition involves not only the interaction of the inhibitor with one or more splicing factor, but also, that its zinc binding group is positioned close to zinc binding group of the target protein, leading to chelation of its zinc. They furthermore suggest that the target proteins are not HDACs. In fact, there are a number of spliceosomal proteins that contain zinc finger motifs and associate with different complexes during the spliceosome assembly pathway (Rappsilber et al., 2002; Zhou et al., 2002; Agafonov et al., 2011; Jurica and Moore, 2003; Bessonov et al., 2008; Bessonov et al., 2010). Their detailed biochemical function is not yet clear, and they could well be targets of the compounds presented here. Our future work will include the affinity labeling of these compounds, which it is hoped will aid the identification of the target(s) in the spliceosome, and thus provide insight into the mechanism of splicing inhibition.

6.4 Materials and Methods

HDAC Assay Inhibition

In vitro HDAC inhibition was assayed using the HDAC Fluorimetric Assay/Drug Discovery Kit as previously described (Chen et al., 2008; Mwakwari et al., 2010a; Oyelere et al., 2009). Briefly, 15 μL of HeLa nuclear extract was mixed with 5 μL of 10× compound and 5 μL of assay buffer. Fluorogenic substrate (25 μL) was added, and reaction was allowed to proceed for 15 min at room temperature and then stopped by addition of a developer containing TSA. Fluorescence was monitored after 15 min at excitation and emission wavelengths of 360 and 460 nm, respectively. IC_{50} values were determined using logit plots. Assays of HDAC1, HDAC6 and HDAC8 activity were performed according to the manufacturer's instructions.

Splicing substrates, reactions, and spliceosome complex analysis

Uniformly ^{32}P-labeled, m^{7}G(5')ppp(5')G-capped MINX pre-mRNA was synthesized in vitro by T7 runoff transcription. Splicing reactions contained 30% (v/v) HeLa nuclear extract in buffer D [20 mM HEPES-KOH at pH 7.9, 100 mM KCl, 1.5 mM $MgCl_2$, 0.2 mM EDTA, 20% (v/v) glycerol, 0.5 mM DTT, 0.5 mM PMSF], 25 mM KCl, 3 mM $MgCl_2$, 20 mM creatine phosphate, 2 mM ATP, 3 nM ^{32}P-labeled pre-mRNA, 2.5% (v/v) DMSO, and the indicated concentration of the chemicals tested for their effect on splicing. For the analysis of the splicing products, the reactions were stopped after 60 min incubation at 30 ºC; RNA was isolated by proteinase K treatment, phenol extraction, and ethanol precipitation; separated by denaturing polyacrylamide gel electrophoresis on an 7 M urea / 14% (w/v) polyacrylamide gel; and visualized by phosphor imaging (Typhoon 8600, GE Healthcare). For the analysis of the spliceosomal complexes, 10 μL of the splicing reaction were added to 2.5 μL of loading buffer

[1× TBE, 30% (v/v) glycerol, 1.25 mg/mL heparin] at the time points indicated, and the mixture was then placed on ice. Complexes were separated on 1.5% (w/v) agarose gels.

ACKNOWLEDGEMENTS

We are grateful to Bob Chen, Sandra Mwakwari and William Guerrant for their contribution to the library used in the original screening assay. This work was financially supported by NIH Grant R01 A131217 and a grant from the Deutsche Forschungsgemeinschaft (FOR 806) to R.L.

SUPPLEMENTAL MATERIAL

Supplemental material is available for this article.

6.5 References

Agafonov DE, Deckert J, Wolf E, Odenwälder P, Bessonov S, Will CL, Urlaub H, Lührmann R. 2011. Semiquantitative proteomic analysis of the human spliceosome via a novel two-dimensional gel electrophoresis method. *Mol Cell Biol* **31:** 2667-2682.

Berg MG, Wan L, Younis I, Diem MD, Soo M, Wang C, Dreyfuss G. 2012. A quantitative high-throughput in vitro splicing assay identifies inhibitors of spliceosome catalysis. *Mol Cell Biol* **32:** 1271-1278.

Bessonov S, Anokhina M, Krasauskas A, Golas MM, Sander B, Will CL, Urlaub H, Stark H, Lührmann R. 2010. Characterization of purified human B^{act} spliceosomal complexes reveals compositional and morphological changes during spliceosome activation and first step catalysis. *RNA* **16:** 2384-2403.

Bessonov S, Anokhina M, Will CL, Urlaub H, Lührmann R. 2008. Isolation of an active step I spliceosome and composition of its RNP core. *Nature* **452:** 846-850.

Canzoneri JC, Chen P, Oyelere AK. 2009. Design and synthesis of novel histone deacetylase inhibitor derived from nuclear localization signal peptide. *Bioorg Med Chem Lett* **19:** 6588-6590.

Chen P, Patil V, Guerrant W, Green P, Oyelere AK. 2008. Synthesis and structure-activity relationship of histone deacetylase (HDAC) inhibitors with triazole-linked cap group. *Bioorg Med Chem* **16:** 4839-4853.

Deckert J, Hartmuth K, Boehringer D, Behzadnia N, Will CL, Kastner B, Stark H, Urlaub H, Lührmann R. 2006. Protein composition and electron microscopy structure of affinity-purified human spliceosomal B complexes isolated under physiological conditions. *Mol Cell Biol* **26:** 5528-5543.

Gunderson FQ, Merkhofer EC, Johnson TL. 2011. Dynamic histone acetylation is critical for cotranscriptional spliceosome assembly and spliceosomal rearrangements. *Proc Natl Acad Sci* **108:** 2004-2009.

Hartmuth K, Urlaub H, Vornlocher HP, Will CL, Gentzel M, Wilm M, Lührmann R. 2002. Protein composition of human prespliceosomes isolated by a tobramycin affinity-selection method. *Proc Natl Acad Sci* **99:** 16719-16724.

Hertweck M, Hiller R, Mueller MW. 2002. Inhibition of nuclear pre-mRNA splicing by antibiotics in vitro. *Eur J Biochem* **269:** 175-183.

Hnilicová J, Hozeifi S, Dušková E, Icha J, Tománková T, Staněk D. 2011. Histone deacetylase activity modulates alternative splicing. *PLoS One* **6:** e16727.

Jurica MS, Moore MJ. 2003. Pre-mRNA splicing: awash in a sea of proteins. *Mol Cell* **12:** 5-14.

Kaida D, Motoyoshi H, Tashiro E, Nojima T, Hagiwara M, Ishigami K, Watanabe H, Kitahara T, Yoshida T, Nakajima H, Tani T, Horinouchi S, Yoshida M. 2007. Spliceostatin A targets SF3b and inhibits both splicing and nuclear retention of pre-mRNA. *Nat Chem Biol* **3:** 576-583.

Kotake Y, Sagane K, Owa T, Mimori-Kiyosue Y, Shimizu H, Uesugi M, Ishihama Y, Iwata M, Mizui Y. 2007. Splicing factor SF3b as a target of the antitumor natural product pladienolide. *Nat Chem Biol* **3:** 570-575.

Kuhn AN, van Santen MA, Schwienhorst A, Urlaub H, Lührmann R. 2009. Stalling of spliceosome assembly at distinct stages by small-molecule inhibitors of protein acetylation and deacetylation. *RNA* **15:** 153-175.

Miller TA, Witter DJ, Belvedere S. 2003. Histone deacetylase inhibitors. *J Med Chem* **46:** 5097-5116.

Mwakwari SC, Guerrant W, Patil V, Khan SI, Tekwani BL, Gurard-Levin ZA, Mrksich M, Oyelere AK. 2010a. Non-peptide macrocyclic histone deacetylase inhibitors derived from tricyclic ketolide skeleton. *J Med Chem* **53:** 6100-6111.

Mwakwari SC, Patil V, Guerrant W, Oyelere AK. 2010b. Macrocyclic histone deacetylase inhibitors. *Curr Top Med Chem* **10:** 1423-1440.

O'Brien K, Matlin AJ, Lowell AM, Moore MJ. 2008. The biflavonoid isoginkgetin is a general inhibitor of pre-mRNA splicing. *J Biol Chem* **283:** 33147-33154.

Oyelere AK, Chen P, Guerrant W, Mwakwari SC, Hood R, Zhang Y, Fan Y. 2009. Non-peptide macrocyclic histone deacetylase inhibitors. *J Med Chem* **52:** 456-468.

Patil V, Guerrant W, Chen P, Gryder B, Benicewicz DB, Khan SI, Tekwani BL, Oyelere AK. 2010. Antimalarial and antileishmanial activities of histone deacetylase inhibitors with triazole-linked cap group. *Bioorg Med Chem* **18:** 415-425.

Pilch B, Allemand E, Facompré M, Bailly C, Riou JF, Soret J, Tazi J. 2001. Specific inhibition of serine- and arginine-rich splicing factors phosphorylation, spliceosome assembly, and splicing by the antitumor drug NB-506. *Cancer Res* **61:** 6876-6884.

Rappsilber J, Ryder U, Lamond AI, Mann M. 2002. Large-scale proteomic analysis of the human spliceosome. *Genome Res* **12:** 1231-1245.

Ropero S, Esteller M. 2007. The role of histone deacetylases (HDACs) in human cancer. *Mol Oncol* **1:** 19-25.

Samatov TR, Wolf A, Odenwälder P, Bessonov S, Deraeve C, Bon RS, Waldmann H, Lührmann R. 2012. Psoromic acid derivatives: a new family of small-molecule pre-mRNA

splicing inhibitors discovered by a stage-specific high-throughput in vitro splicing assay. *Chembiochem* **13:** 640-644.

Shomron N, Malca H, Vig I, Ast G. 2002. Reversible inhibition of the second step of splicing suggests a possible role of zinc in the second step of splicing. *Nucleic Acids Res* **30:** 4127-4137.

Tazi J, Bakkour N, Soret J, Zekri L, Hazra B, Laine W, Baldeyrou B, Lansiaux A, Bailly C. 2005a. Selective inhibition of topoisomerase I and various steps of spliceosome assembly by diospyrin derivatives. *Mol Pharmacol* **67:** 1186-1194.

Tazi J, Durand S, Jeanteur P. 2005b. The spliceosome: a novel multi-faceted target for therapy. *Trends Biochem Sci* **30:** 469-478.

Wahl MC, Will CL, Lührmann R. 2009. The spliceosome: Design principles of a dynamic RNP machine. *Cell* **136**: 701-718.

Zhou Z, Licklider LJ, Gygi SP, Reed R. 2002. Comprehensive proteomic analysis of the human spliceosome. *Nature* **419:** 182-185.

CHAPTER 7: CONCLUSIONS AND FUTURE DIRECTIONS

The work completed in this thesis will provide the foundation for a wide array of future studies in the lab of Dr. Oyelere. Novel compounds presented here were designed, synthesized, characterized and their biological targets were validated. This is just the beginning of understanding the potential of each novel class of molecules. For example, the anthracycline derivative topoisomerase II / histone deacetylase inhibitor conjugates, with their differential mode of nucleic acid binding, may prove to have a unique side effect profile in a therapeutic application. The peptolide probe family of molecules will also be further investigated. As for the currently synthesized peptolides, future studies could involve their ability to overcome antibiotic resistant strains of prokaryotes due to the vast increase of binding area compared to macrolides alone. As a result of the observation of this thesis work that some peptolides posses eukaryotic translation inhibition capabilities, they could also prove to be useful in preventing the growth of rapidly proliferating eukaryotic cells such as plasmodium, leishmania, or tumor cells. Additionally, different head groups could be used in createing new peptolides; for example, an oxazolidinone antibiotic could be used to sample a different binding area of the ribosome.

APPENDIX A

Supporting Information for Chapter 2

Interaction of Anthracyclines with Iron Responsive Element mRNAs[†]

Joshua C. Canzoneri, Adegboyega K. Oyelere*

School of Chemistry and Biochemistry, Parker H. Petit Institute for Bioengineering and Biosciences, Georgia Institute of Technology, Atlanta, GA 30332-0400

*To whom all correspondence should be addressed.

Supporting Information

A

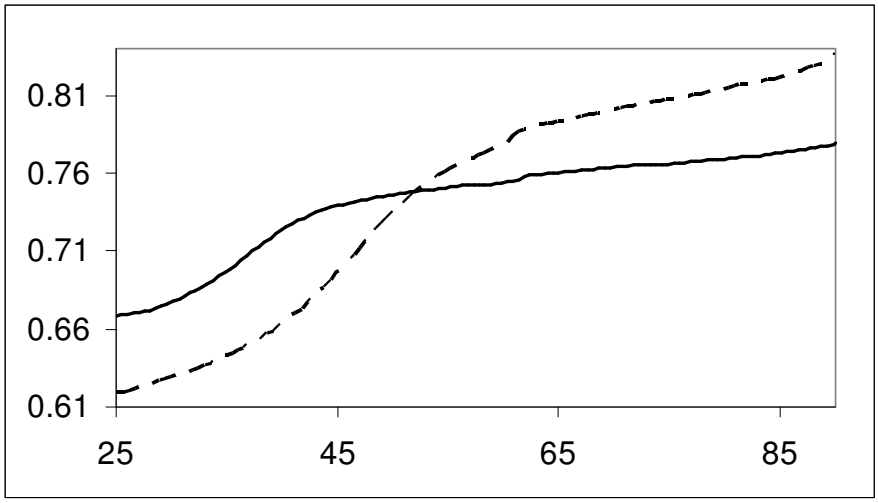
0.81
0.76
0.71
0.66
0.61
25
45
65
85

B

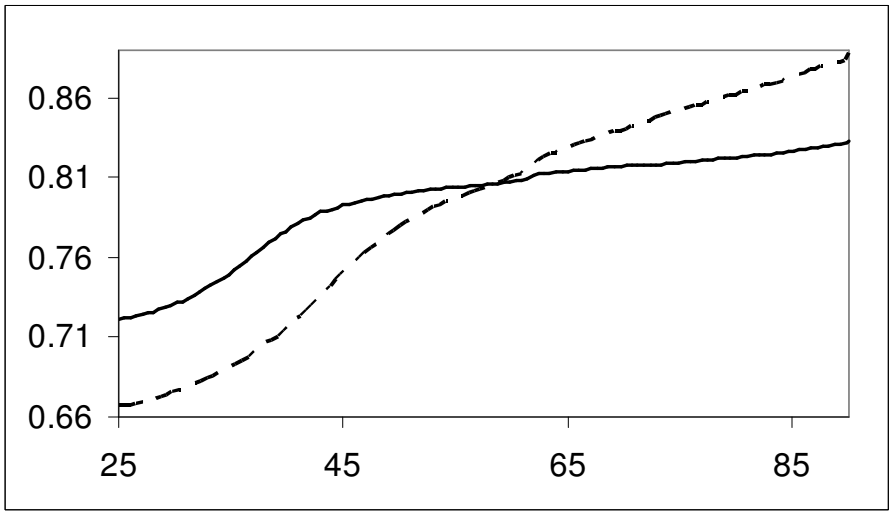
0.86
0.81
0.76
0.71
0.66
25
45
65
85

C

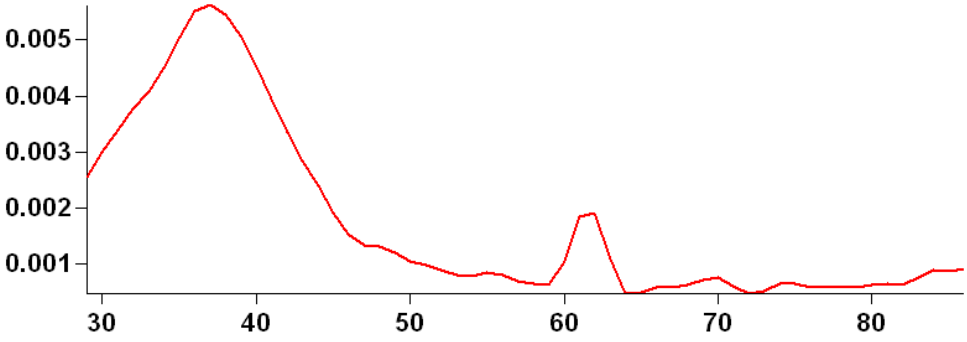
0.005
0.004
0.003
0.002
0.001
30
40
50
60
70
80

D

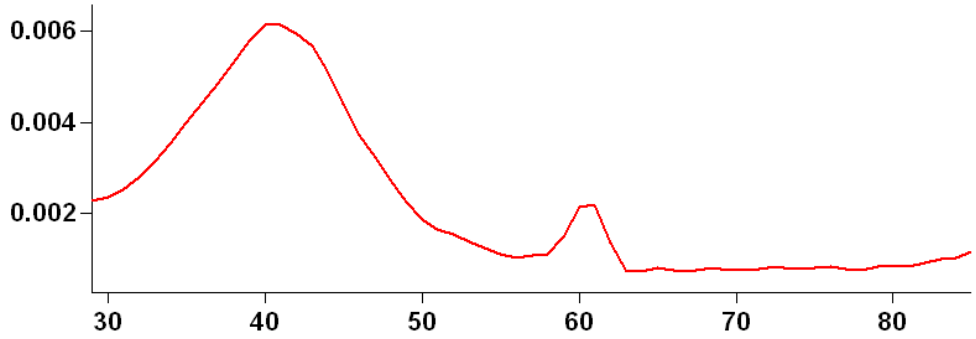
0.006
0.004
0.002
30
40
50
60
70
80

E

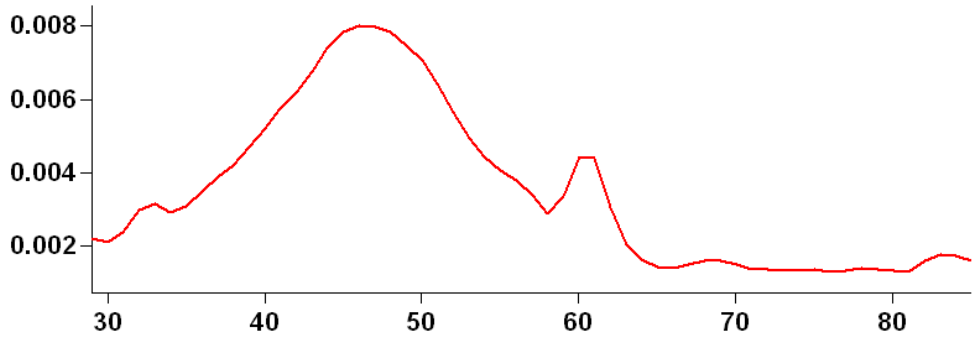
0.008
0.006
0.004
0.002
30
40
50
60
70
80

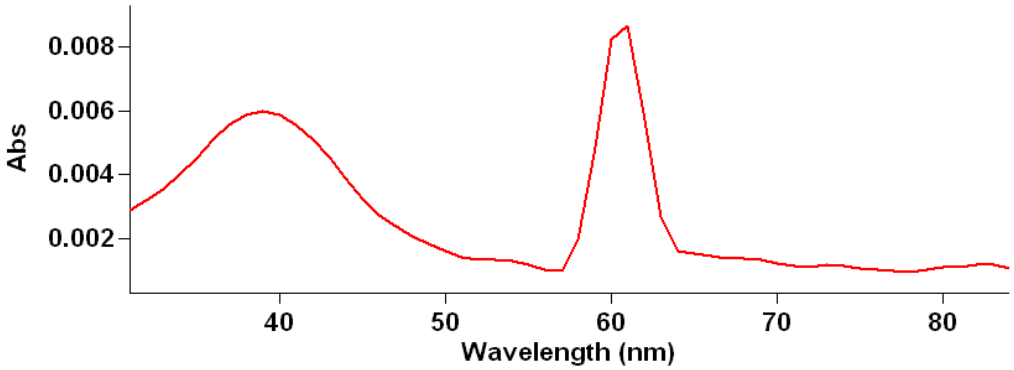
Abs
0.008
0.006
0.004
0.002
40
50
60
70
80
Wavelength (nm)

F

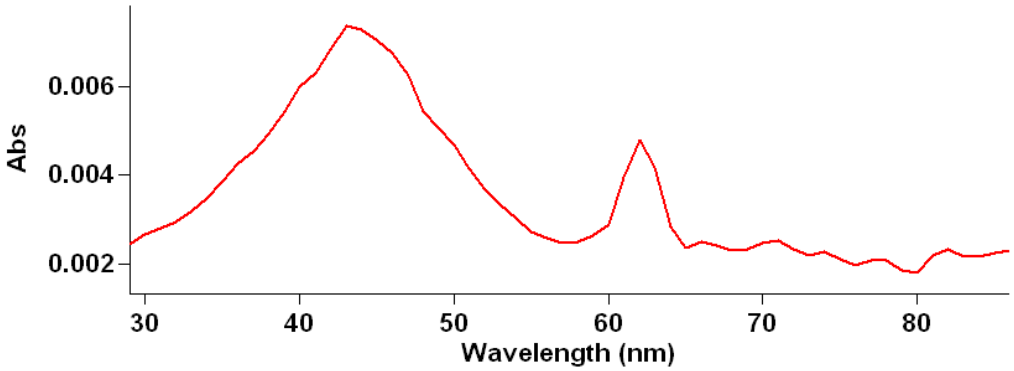

G

Fig. S1 UV-vis melting curves of ferritin H-chain IRE RNA in the absence (solid) and presence (dashed) of A) 20 µM DOX and B) 20 µM DAU and first derivative plots H-chain IRE RNA in the presence of C) no drug, D) 5 µM DOX, E) 20 µM DOX, F) 5 µM DAU, G) 20 µM DAU

A

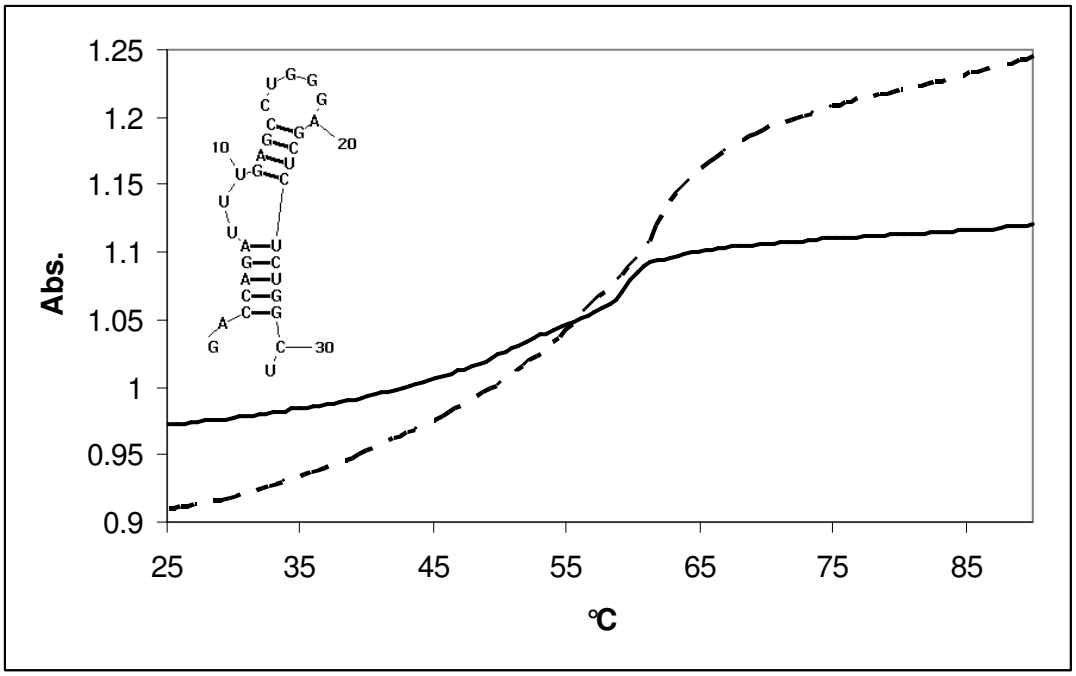

B

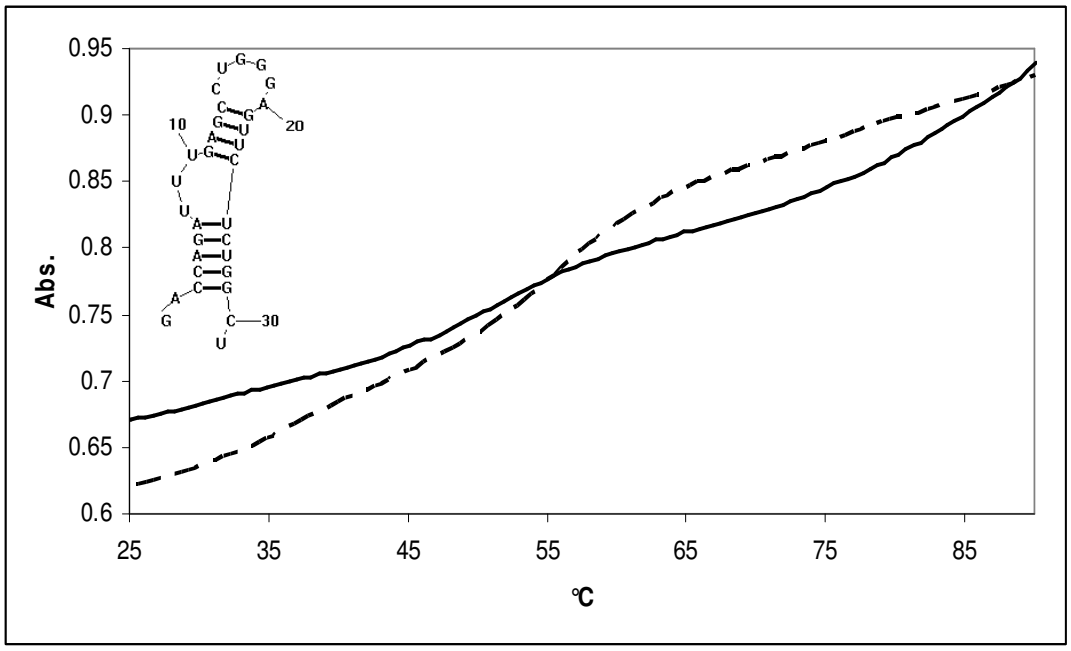

Fig. S2 Overlay of the melting profiles of (*A*) TAR mRNA and (*B*) TAR C22U mRNA in the absence (*solid*) and presence (*dashed*) of 20 μM DOX. The secondary structure of each construct is inlayed.

A

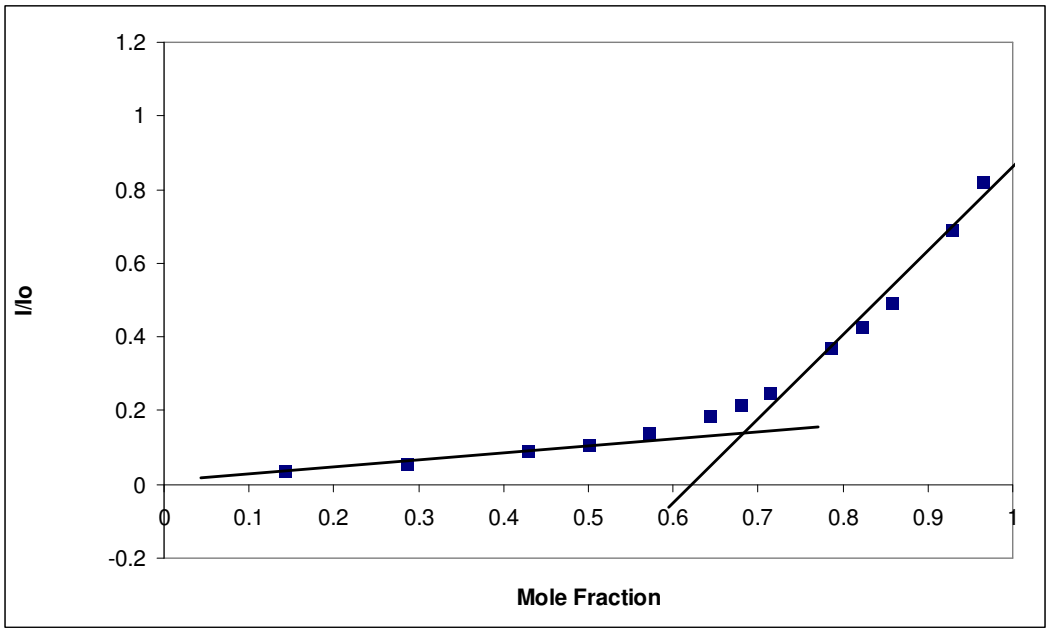

B

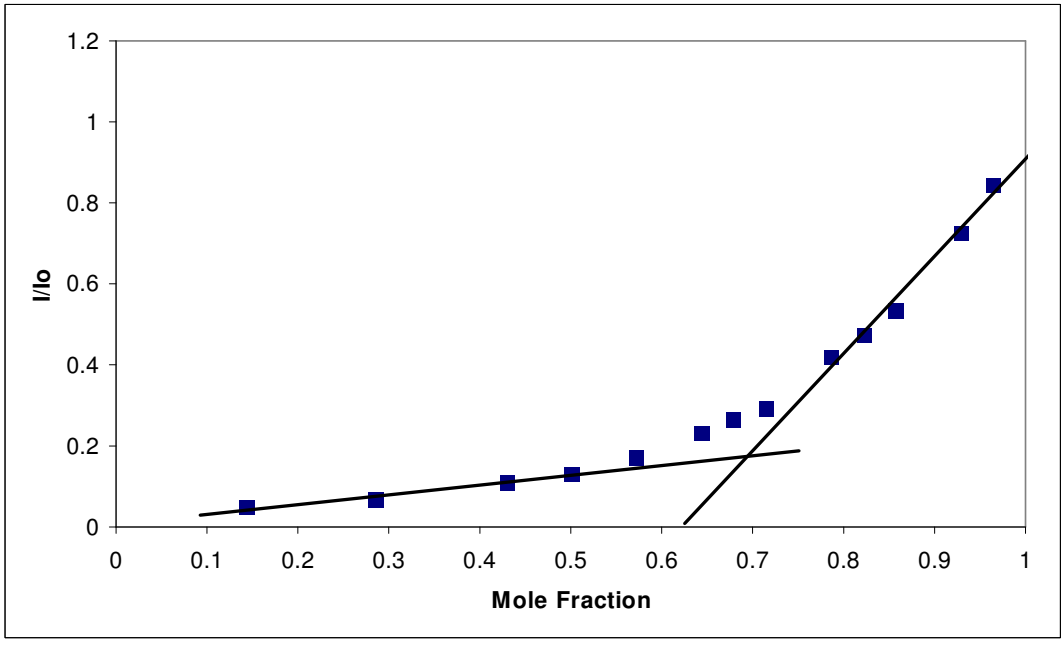

Fig S3 Job plots for: (*A*) U6C, U10C Ferritin H-chain IRE RNA double mutant, and (*B*) U10C Ferritin H-chain IRE RNA mutant

Fig. S4 Cleavage band validation autoradiograph. Lane: (1) Ladder of 16-poly -U and 23-poly-U RNA constructs. (2) Ferritin H-chain IRE RNA only. (3) Ferritin H-chain IRE RNA and 20 μM DOX after T1 digestion. The 16-poly-U and 23-poly-U bands are adjacent to the cleavage bands denoted G16 and G23, respectfully, supporting the cleavage band denotation presented in Fig. 5.

Table S1 Average T_M values for all construct and drug combinations.

	H-chain	L-chain	G23I-IRE	U10C-IRE	U6C-IRE	C8A-IRE	U6C-U10C-IRE
RNA only	38.0	33.5	32.2	48.8	42.5	37.1	55.0
5 µM DOX	40.5	36.2	36.9	52.5	45.1	41.0	56.0
20 µM DOX	47.9	43.6	42.5	55.6	49.0	45.0	60.5
5 µM DAU	38.5	37.0	36.0	50.5	44.0	40.0	55.5
20 µM DAU	43.7	40.0	39.5	53.5	46.5	43.0	56.5

A

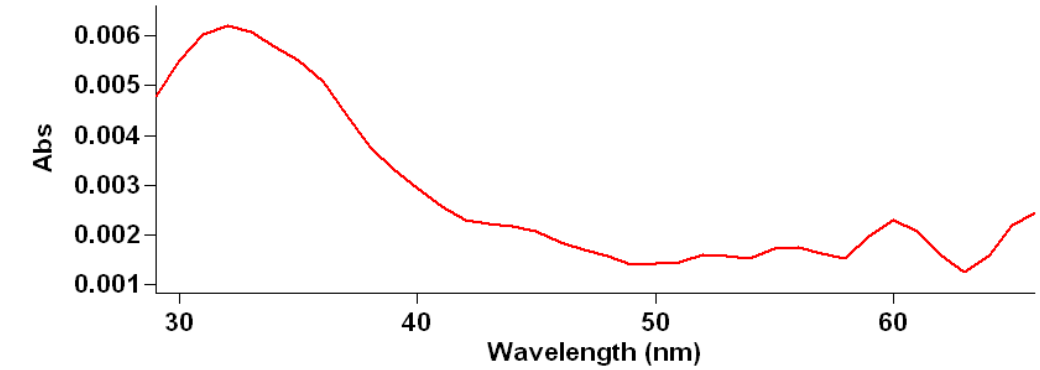

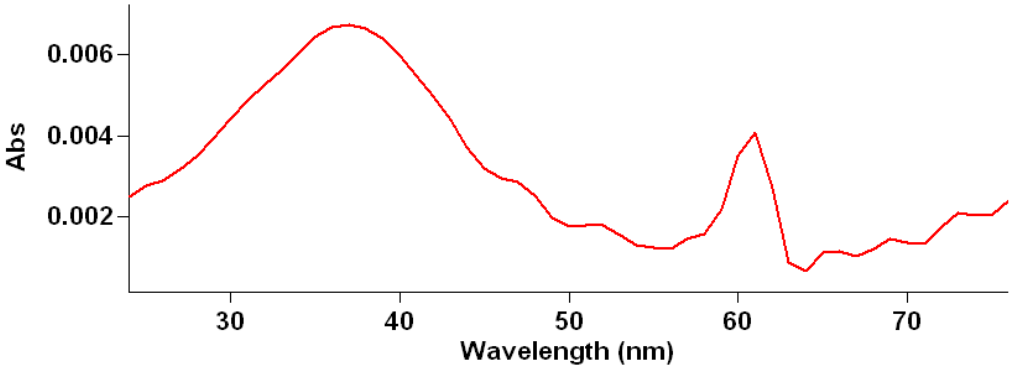

B

C

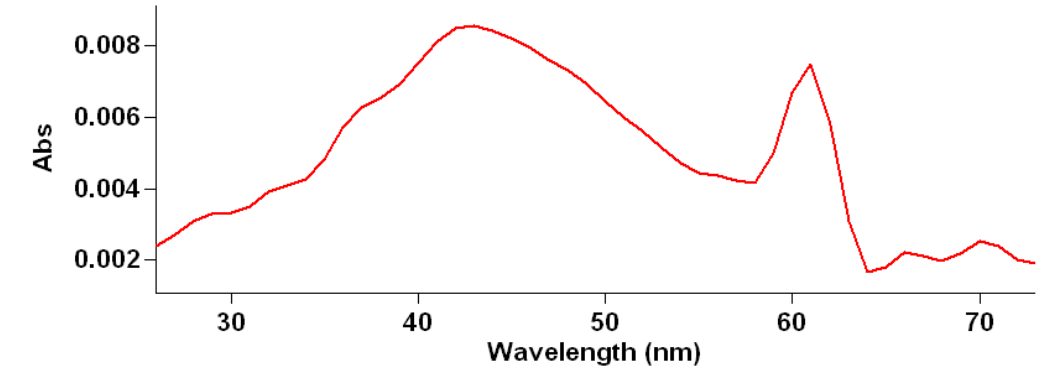

Figure S5 First derivative plots of UV melting profiles for construct G23I and A) No drug, B) 5 µM DOX and C) 20 µM DOX.

A

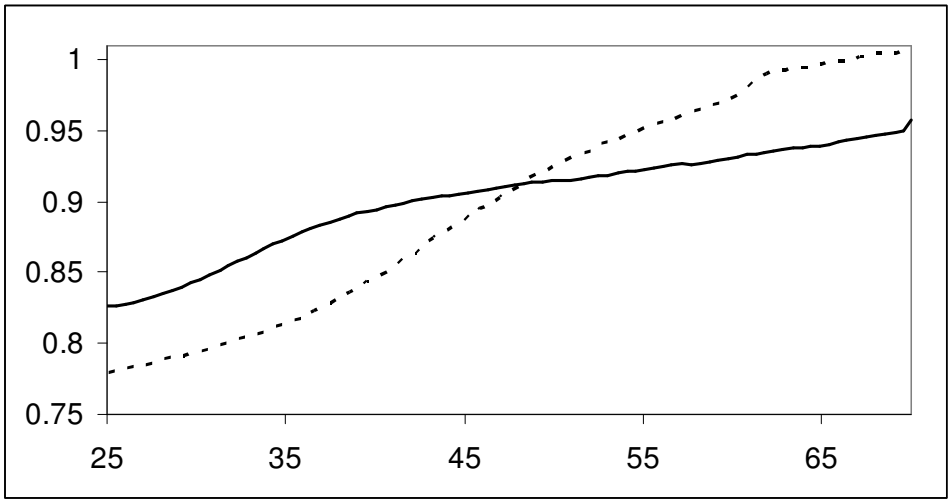

B

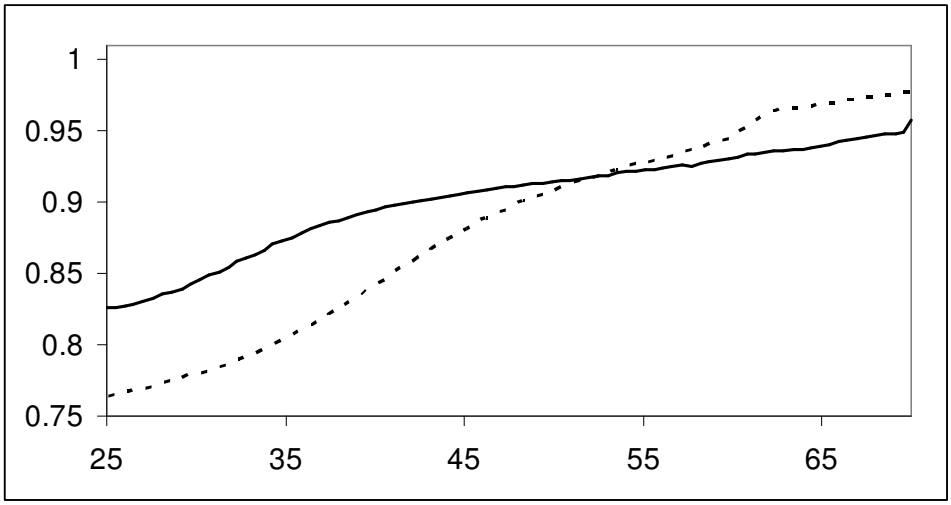

Overlay of the melting profiles of G23I mRNA (*A*) in the absence (*solid*) and presence (*dashed*) of 20 μM DOX, and (*B*) in the absence (*solid*) and presence (*dashed*) of 20 μM DAU.

Fluorescence Quenching Data and TableCurve Fits

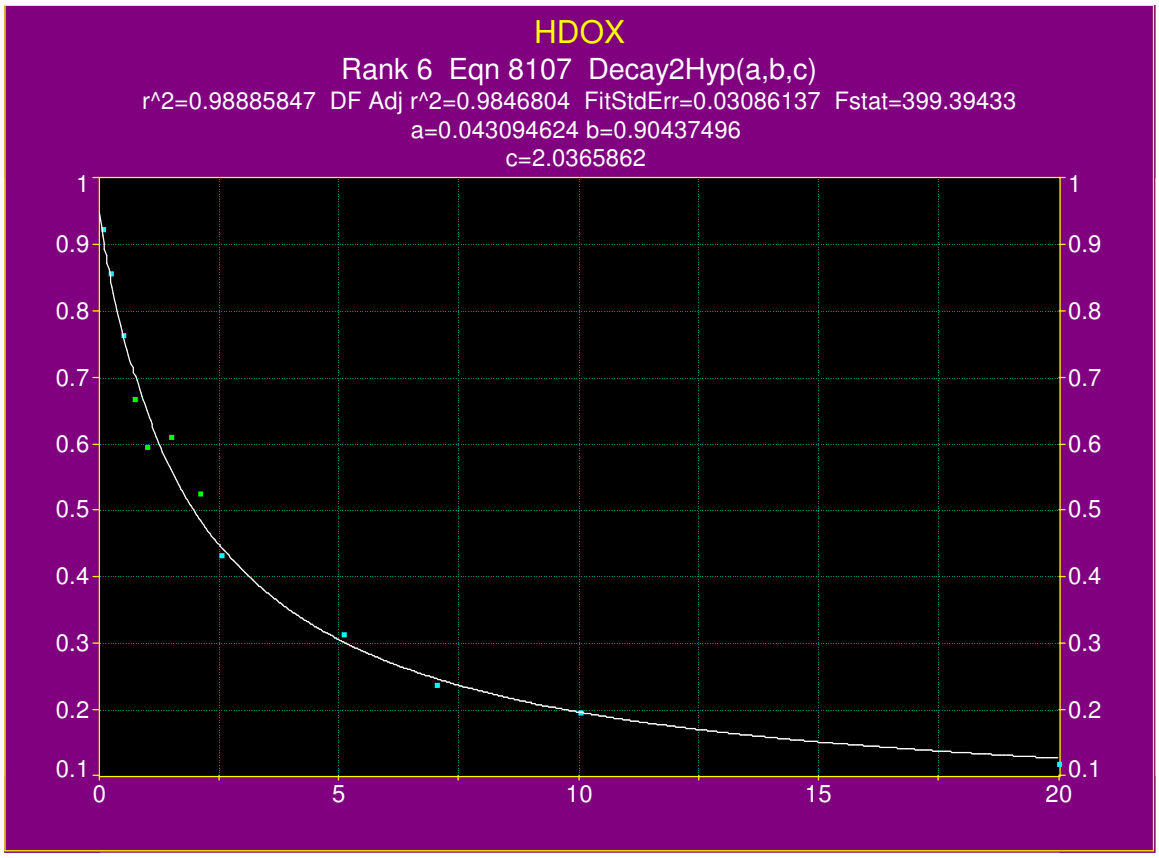

H-Chain IRE RNAFluorescence Quenching Profile

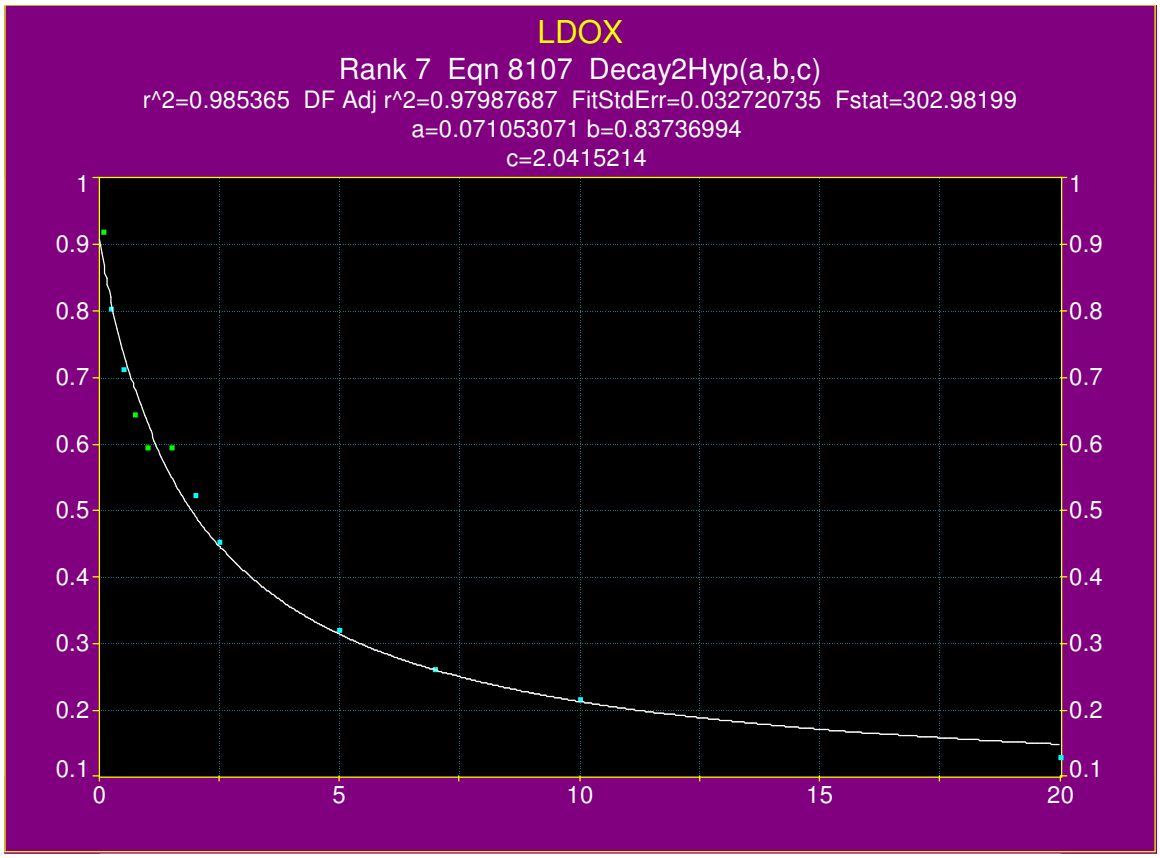

L-Chain IRE RNAFluorescence Quenching Profile

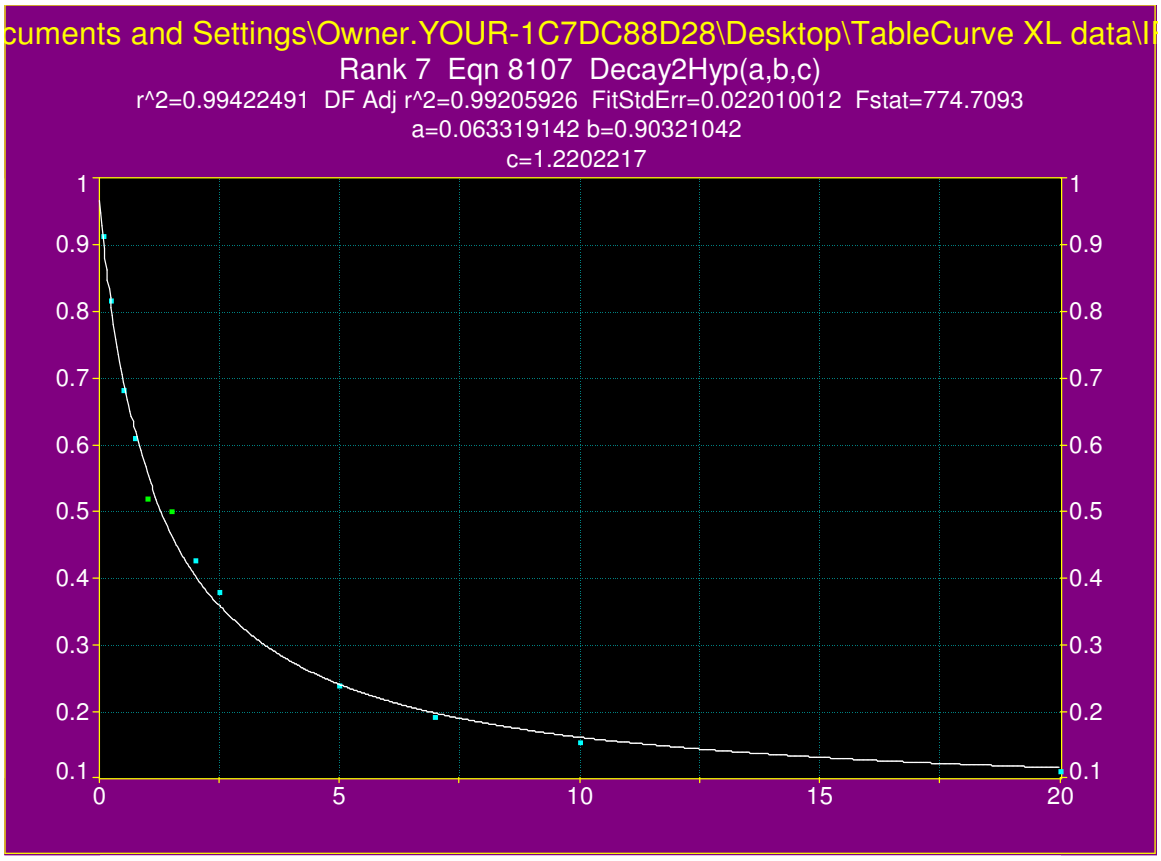

G23I IRE RNAFluorescence Quenching Profile

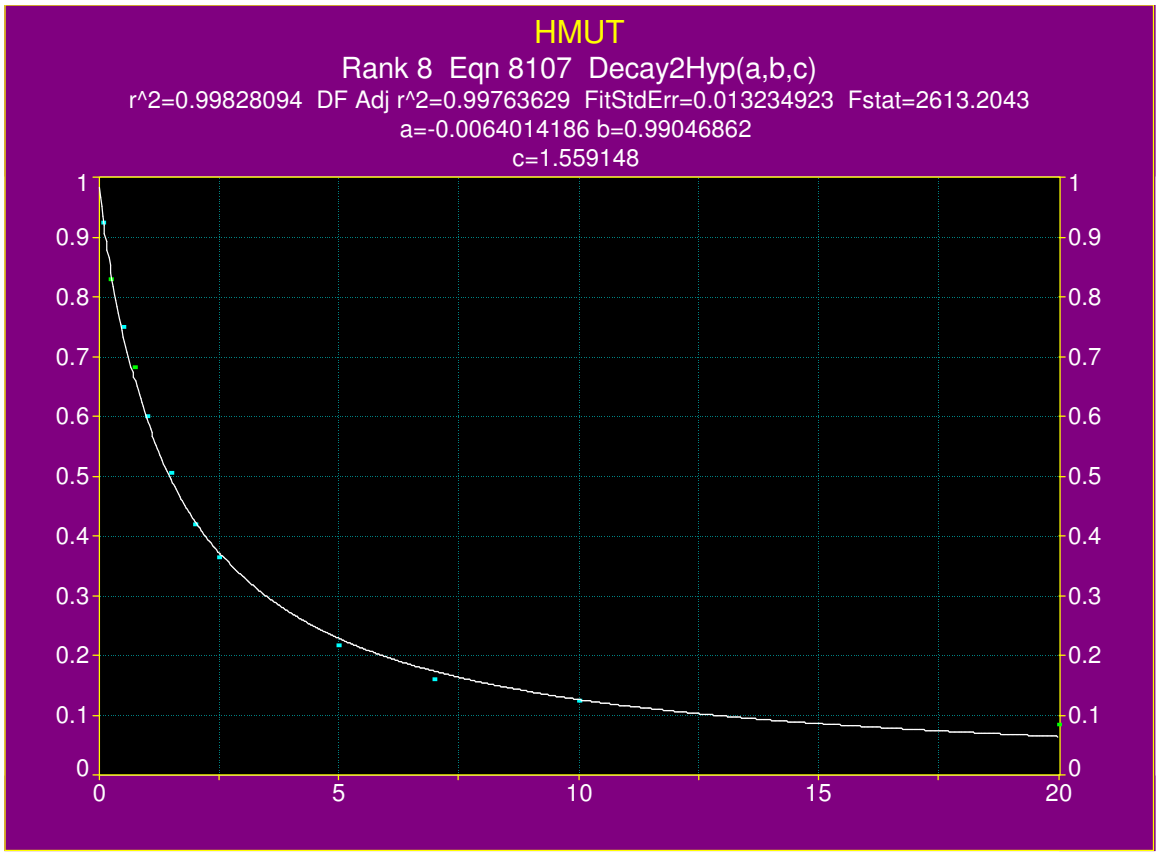

U10C IRE RNAFluorescence Quenching Profile

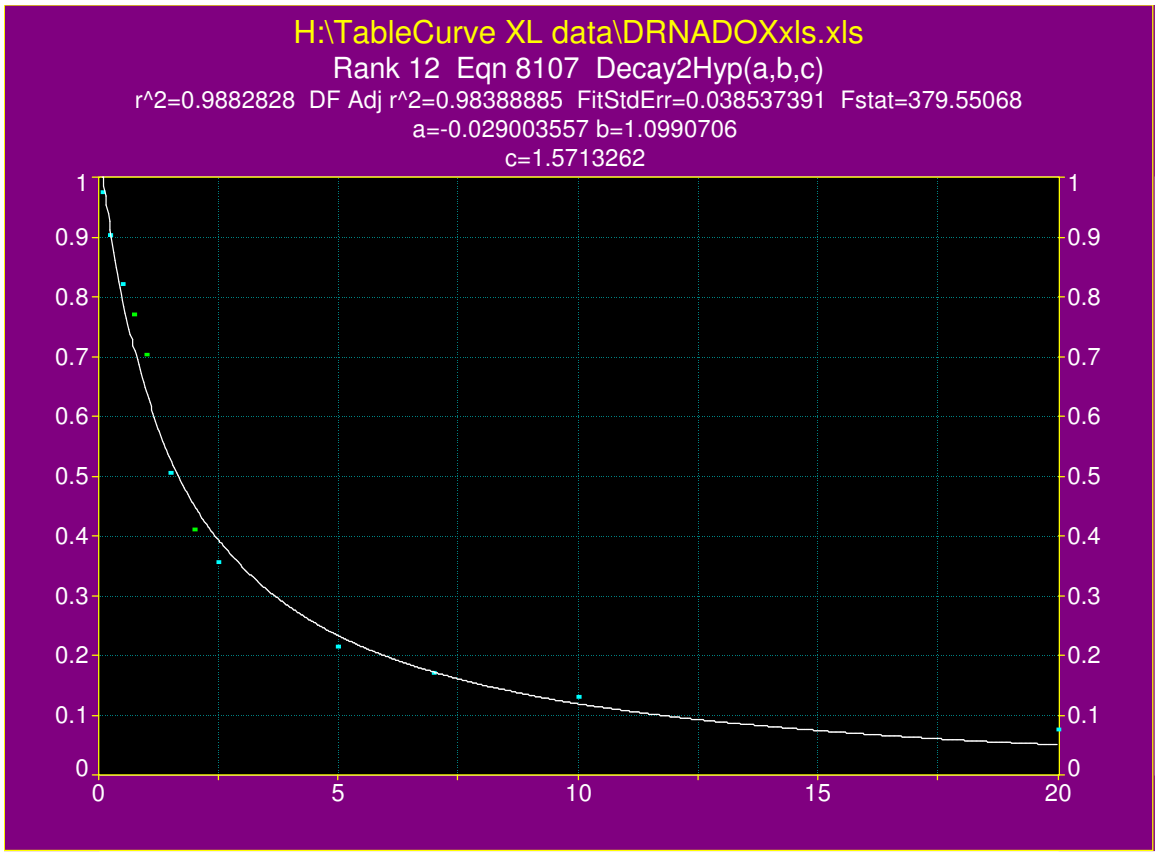

U6C, U10C IRE RNAFluorescence Quenching Profile

APPENDIX B

Chapter 5 Supporting Information

Cellular Localization of Dual-acting Inhibitors in A549 cells

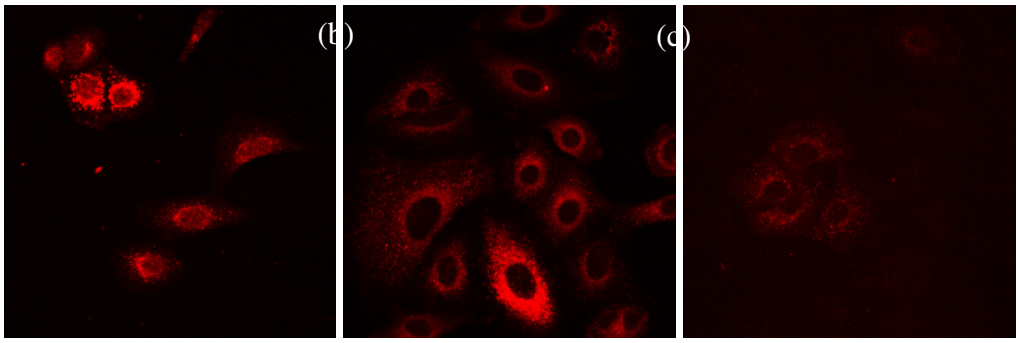

Figure B1. Cellular Localization of Dual-Acting Inhibitors. (A) **DAU**, (B) **7**, (C) **12b**. A549 cells were dosed at 1μM for 4 hours with indicated compounds and visualized by confocal microscopy.

VITA

JOSHUA CRAIG CANZONERI

Joshua Canzoneri was born in Fort Carson, Colorado in 1983 to Craig and Anita Canzoneri. His sister, Jessica, shares the same birthday but is four years younger. Joshua graduated from Columbus High School in Columbus, Georgia in 2001. After receiving a hard-earned appointment to the United States Military Academy in West Point, New York, Joshua instead chose to attend Georgia Southern University in Statesboro, Georgia, on a full academic scholarship as a Bell Honors Scholar, where he majored in chemistry and minored in biology. He then joined the lab of Dr. Adegboyega "Yomi" Oyelere in 2005 at the Georgia Institute of Technology in Atlanta, Georgia to pursue his doctoral degree in biochemistry. While at Georgia Tech, he was awarded a GAANN predoctoral fellowship from the Georgia Tech Center for Drug Design, Development, and Delivery in 2007. Following the defense of his PhD thesis, Joshua will marry his fiancée, Tiffany W. Livingston on November 4th, 2012. The two first met at Columbus High School in 2000. When not in the laboratory, Joshua thoroughly enjoys being an avid outdoorsmen, bowhunter, and powerlifter.